
Design, fabrication and characterisation of silicon carbide resonators

Enrico Mastropaolo



A thesis submitted for the degree of Doctor of Philosophy.

The University of Edinburgh.

December, 2010

Abstract

Micro-electro-mechanical systems (MEMS) are integrated mechanical and electrical elements realised with micro-fabrication technology and employed as sensors and actuators. The integration of reliable MEMS switches and resonators into transceiver devices is a challenging and attractive solution to increase the efficiency and reduce the power consumption. Silicon carbide (SiC) is an excellent candidate for developing robust and reliable high frequency MEMS for transceivers applications due to its unique mechanical properties.

This thesis presents the design, fabrication and characterisation of 3C-SiC micro-mechanical vertical resonators. New device architectures have been developed for the study of the electro-mechanical behaviour of the devices with the aim of optimising the actuation efficiency, increasing the resonant frequency and obtaining new device functions.

A process for the fabrication of single or poly-crystalline 3C-SiC cantilevers, bridges and rings has been developed with the option of integrating top electrodes made of aluminium (Al) or lead zirconium titanate (PZT). The crystal structure and quality of the SiC layers have been evaluated with X-ray diffraction and Raman spectroscopy. A Young's Modulus of ~ 440 GPa has been calculated for the single crystalline SiC from the mechanical resonant frequency of the fabricated single material cantilevers. The fabricated Al/SiC bridges and rings have been actuated and driven into resonance electro-thermally. It has been found that wide Al electrodes applied close to the beams' anchor can maximise the induced displacement and vibration amplitude thus improving the actuation efficiency. Resonant frequencies in the MHz range have been obtained with the ring architectures therefore achieving higher frequencies compared to beam architectures. In addition, electro-thermal mixing of two input frequencies has been demonstrated and performed with the fabricated Al/SiC structures. Furthermore, piezo-electric transduction has been used for actuating the PZT/SiC cantilevers and for sensing the devices' resonance electrically. The design of the PZT piezo-electric active layer has been shown to influence strongly the devices' resonant frequency and has been optimised to enhance the electrical output by decreasing the electrodes length thus decreasing the feedthrough capacitance.

The results obtained in this work can be used for the implementation of SiC MEMS mixer-filters with electro-thermal actuation and piezo-electric sensing for transceiver applications.

Declaration

I hereby declare that the research reported in this thesis is my own work, produced without the prohibited assistance of third parties and without making use of aids other than those specified; notions taken over directly or indirectly from other sources have been identified as such. The thesis itself has been written by me and the work presented has been conducted in the School of Engineering at the University of Edinburgh from 2006 to 2010 under the supervision of Prof. Rebecca Cheung. This work has not been submitted for any other degree or professional qualification.

EDINBURGH,

Signature

Date

21/01/2011

To my family

"Turn off the TV. Read your elementary science textbooks."

from "Dancing Naked in the Mind Field"

by Dr. Kary B. Mullis (Nobel Prize in Chemistry 1993)

Acknowledgements

I would like to thank my supervisor Prof. Rebecca Cheung for her help, guidance and continuous encouragement that she has given me during my PhD studies. Great thanks go to all the people that had introduced me to the wonderful world of micro fabrication technology. In particular, my gratitude to Alan Gundlach and Dr. Andy Bunting for having taught me the secrets of IC fabrication, to Dr. Bill Parkes and Dr. Camelia Dunare for all their help with the ICP and SEM tools. Another deep thank you to Alec Ruthven, Kevin Tierney, Hugh Frizell, Ewan Macdonald, Stewart Ramsay and Richard Blair, excellent engineers who taught me that everything can be fixed. Thanks must go to the *pt35* and *memsstar* team, Tony O'Hara, Graeme Pringle, Lorna Slater and Mike Brown, for the help and assistance with their excellent sacrificial vapour release tools. I am also grateful to Dr. John Hedley and Dr. Zhongxu Hu from Newcastle University for their help with the vibrometer measurements. I would also like to thank Damien, Graham, Isaac and Juanjo for being wonderful working colleagues, good friends and for their helpful humour at coffee and lunch breaks in moments of big depression for failed experiments.

I am deeply thankful to Annalisa for being there with her patience and moral support during these years in Edinburgh. I dedicate this thesis to my parents and family that have always motivated and supported me during my studies.

Contents

List of figures	xii
List of tables	xvi
1 Introduction	1
1.1 Micro-electro-mechanical systems	1
1.1.1 History of MEMS	2
1.1.2 MEMS market	3
1.1.3 Radio frequency MEMS	4
1.1.4 MEMS resonators	5
1.2 Silicon carbide	6
1.3 Thesis plan	7
2 Silicon carbide for MEMS applications	11
2.1 Introduction	11
2.2 SiC properties	12
2.3 SiC growth	14
2.4 SiC etching	15
2.5 SiC micromachining	17
2.5.1 Bulk micromachining	18
2.5.2 Surface micromachining	19
2.5.3 One-step etch and release	20
2.6 SiC MEMS	21
2.6.1 First devices: thermistors	22
2.6.2 Pressure sensors	22
2.6.3 Accelerometers	23
2.6.4 Resonators	24
2.7 Conclusions	25
3 MEMS actuators: basic structures and transduction techniques	28
3.1 Introduction	28
3.2 Basic structures	29
3.2.1 Single-clamped beams - cantilevers	31
3.2.2 Double-clamped beams - bridges	32
3.2.3 Circular membranes - disks	32
3.2.4 Considerations on the fundamental resonant frequency	32

3.3	Electro-thermal transduction	34
3.3.1	Brief introduction	34
3.3.2	Displacement	36
3.3.3	Vibration and resonance	38
3.4	Piezo-electric transduction	39
3.4.1	Brief introduction	39
3.4.2	Displacement and induced force	41
3.5	Electro-static transduction	43
3.5.1	Brief introduction	43
3.5.2	Displacement and induced force	44
3.5.3	Actuation: vibration and resonance	46
3.5.4	Electro-static mixing	46
3.6	Conclusions	47
4	Design and fabrication of SiC MEMS	50
4.1	Introduction	50
4.2	General observation on the design and fabrication	51
4.3	SiC beams	51
4.3.1	SiC growth	52
4.3.2	SiC etching and choice of masking material	52
4.3.3	SiC release	55
4.4	SiC beams with Al electrodes	56
4.5	SiC beams with piezo-electric active layers	57
4.5.1	Fabrication of piezo-electric active layers	58
4.5.2	Integration of piezo-electric active layers into SiC beams actuators	60
4.6	SiC rings with Al electrodes	61
4.6.1	Release characterisation	63
4.7	Conclusions	66
5	Characterisation of SiC	68
5.1	Introduction	68
5.2	Raman spectroscopy characterisation	69
5.2.1	Introduction to Raman spectroscopy	69
5.2.2	Raman spectroscopy measurements results	71
5.3	X-ray diffraction characterisation	72
5.3.1	Introduction to XRD	73
5.3.2	XRD measurements results	73
5.4	Resonance measurement system and mechanical actuation	74
5.5	Young's modulus calculation	76
5.6	Conclusions	79
6	Electro-thermal actuation of SiC double clamped beam resonators with u-shaped electrodes	82
6.1	Introduction	82
6.2	Resonator and u-shaped electrode design	83
6.3	Simulations	84

6.3.1	General observations on the induced deflection	85
6.3.2	Influence of electrode length L_e on the bridge deflection	88
6.3.3	Influence of electrode width W on the bridge deflection	92
6.3.4	Influence of electrode spacing S on the bridge deflection	95
6.4	Measurements: electro-thermal actuation and resonance detection	96
6.5	Measurements: vibration amplitude	98
6.5.1	Influence of the electrode width W on vibration amplitude	99
6.5.2	Influence of the electrode spacing S on vibration amplitude	101
6.6	Conclusions	102
7	Electro-thermal actuation of SiC double clamped beam resonators with slab electrodes	104
7.1	Introduction	104
7.2	Resonator and slab electrode design	105
7.3	Simulations: the slab electrode	106
7.3.1	General observations	107
7.3.2	Influence of the electrode length L_e on the bridge deflection	108
7.4	Measurements: the slab electrode	110
7.5	Simulations: comparison between slab and u-shaped electrodes	112
7.6	Measurements: comparison between slab and u-shaped electrodes	114
7.7	Conclusions	115
8	Study of the mechanical behaviour and electro-thermal actuation of SiC ring resonators	118
8.1	Introduction	118
8.2	Resonator and electrodes design	119
8.3	Simulations: mechanical behaviour	121
8.4	Simulations: electro-thermal behaviour	123
8.5	Measurements: mechanical actuation	124
8.6	Measurements: electro-thermal actuation	126
8.7	Conclusions	128
9	Electro-thermal mixing with bimaterial Al/SiC resonators	131
9.1	Introduction	131
9.2	Electro-thermal actuation theory	132
9.2.1	Actuation with one voltage	133
9.2.2	Actuation with two voltages	133
9.3	Measurements on cantilevers	134
9.3.1	Sum	136
9.3.2	Difference	137
9.3.3	Mixing resonant frequencies - mechanical and thermal considerations	138
9.3.4	Vibration amplitude	139
9.4	Measurements on rings	140
9.4.1	Actuation and mixing	141
9.4.2	Resonant frequency shift - mechanical and thermal considerations	142

9.5	Conclusions	144
10	Piezo-electric driven SiC single clamped beam resonators	146
10.1	Introduction	146
10.2	General considerations	147
10.2.1	Piezo-electric actuation and sensing	147
10.2.2	Design and fabrication	148
10.3	Simulations	150
10.3.1	Mechanical behaviour - finite element analysis for different electrode lengths L_e	150
10.3.2	Electrical behaviour - circuit analysis for different track lengths L_t	152
10.4	Measurements	155
10.4.1	Measurements setup	155
10.4.2	Measurements results	156
10.5	Conclusions	161
11	Conclusions and future work	164
11.1	Fabrication of SiC MEMS resonators	165
11.2	Characterisation of SiC	166
11.3	Optimisation of electro-thermal actuation - shape and dimensions of the electrode	167
11.3.1	U-shaped electrodes	167
11.3.2	Slab electrodes	168
11.4	Maximisation of resonant frequency - shape and dimensions of the structure	169
11.5	Electro-thermal mixing on Al/SiC structures	170
11.6	Piezo-electric driving of SiC cantilevers	170
11.7	Future work	171
11.7.1	Electro-thermal actuation reliability	172
11.7.2	piezo-electric active layers design	172
11.7.3	SiC electro-thermal filter-mixer with piezo-electric sensing	173
11.8	Final conclusions	174
A	Materials parameters used in the simulations	175
B	Fabrication process details	177
B.1	Tools used for the fabrication	177
B.2	PZT etching	178
C	Young's modulus calculation	179
C.1	Measured resonant frequencies	179
C.2	Average Young's modulus and standard deviation	180
C.3	Final value of the Young's modulus and error estimation	181
C.3.1	Poly-crystalline SiC	181
C.3.2	Single crystalline SiC	181
D	Published and accepted papers	182

References

184

List of figures

1.1	MEMS market in 2009 [1].	4
1.2	RF MEMS devices integration in a transceiver circuit (simplified from [17]).	5
2.1	Si-C bilayers and their orientations to form SiC polytypes: (a) position of C atoms in the Si-C bilayers; (b) stacking sequence for 3C-SiC; (c) stacking sequence for 6H-SiC.	13
2.2	Schematic view of bulk micromachining with back-side and front-side etching.	19
2.3	Schematic view of surface micromachining.	20
2.4	Schematic view of the one-step etch and release process for front-side bulk and surface micromachining.	21
3.1	Schematics of the three basic structures used in this thesis: (a) single-clamped beam (i.e. cantilever), (b) double-clamped beam (i.e. bridge), (c) circular membrane (i.e. disk).	30
3.2	Analytical resonant frequency as a function of the structure's dimension for cantilevers, bridges and disks ($E = 400$ GPa, $\rho = 3200$ kg/m ³ , $t = 2$ μ m).	33
3.3	Schematic of a single material bridge.	37
3.4	Schematic of a bimaterial bridge.	38
3.5	Schematic of a cantilever with a piezo-electric actuating electrode.	41
3.6	Schematic of a bridge with piezo-electric actuating and sensing electrodes.	42
3.7	Schematic of a bridge with bottom electrode.	44
4.1	Fabrication process flow of SiC beams.	53
4.2	Scanning electron micrograph of SiC beams.	56
4.3	Simplified fabrication process flow of Al/SiC beams.	57
4.4	Fabricated bimaterial SiC bridges 150 μ m long with Al electrodes on top.	57
4.5	Fabrication process flow of Pt/PZT/Pt electrodes.	58
4.6	Scanning electron micrograph of a Pt/PZT/Pt electrode.	60
4.7	Simplified fabrication process flow of Pt/PZT/Pt/SiC beams.	60
4.8	Scanning electron micrograph of a SiC beam with a piezo-electric layer on top.	61
4.9	Schematic of the fabricated Al/SiC ring resonators.	62

4.10	Optical micrograph of two of the fabricated bimaterial Al/SiC ring resonators.	63
4.11	Release length in the radial direction as a function of process time for holes with radius $h = 2, 6, 15 \mu\text{m}$ at chamber pressure of 1 and 2 Torr and flow rate = 100 sccm.	64
4.12	Area release rate as a function of etching time for holes with radius $h = 2, 6, 15 \mu\text{m}$ at chamber pressure of 1 and 2 Torr and flow rate = 100 sccm.	65
5.1	Schematic representation of Raman scattering emission.	70
5.2	Raman spectra of SiC grown by hot-wall LPCVD.	71
5.3	Schematic representation of the X-ray diffraction mechanism.	73
5.4	XRD of poly (a) and single (b) crystalline SiC layers grown on top of Si substrates.	74
5.5	Schematic of the measurement setup for mechanical actuation and resonance detection of MEMS structure.	75
5.6	Measured resonant peaks when actuating mechanically the fabricated SiC cantilevers.	77
5.7	Measured and simulated SiC cantilevers resonant frequencies as a function of beams' length.	79
6.1	Schematic of the designed Al/SiC bridge resonators: u-shaped electrode layout with actuation voltage V_{in} applied.	83
6.2	Simulations, u-shaped layout: illustration of the direction of the simulated deflections.	87
6.3	Simulations, u-shaped layout: maximum displacement for $L_b = 200 \mu\text{m}$ and $W_b = 76 \mu\text{m}$ as a function of the electrode length L_e (electrode width $W = 9 \mu\text{m}$, electrode spacing $S = 30 \mu\text{m}$).	89
6.4	Simulations, u-shaped layout: temperature data of $200 \mu\text{m}$ long bridges for different electrode lengths L_e	90
6.5	Simulations, u-shaped layout: snapshots for $200 \mu\text{m}$ long bridge as a function of the electrode length L_e ($W = 9 \mu\text{m}$ and $S = 30 \mu\text{m}$).	91
6.6	Simulations, u-shaped layout, width variations: displacement and temperature as a function of the electrode length L_e for electrode width $W = 6, 9, 12 \mu\text{m}$ (electrode spacing $S = 30 \mu\text{m}$).	93
6.7	Simulations, u-shaped layout, spacing variations: displacement and temperature as a function of the electrode length L_e for electrode spacing $S = 10, 30, 50 \mu\text{m}$ (electrode spacing $W = 7 \mu\text{m}$).	96
6.8	Measurement setup for the electro-thermal actuation of the fabricated Al/SiC bimaterial bridges.	97
6.9	Measurements, u-shaped layout: resonant peak of an electro-thermally actuated Al/SiC bridge resonator $200 \mu\text{m}$ long and $2 \mu\text{m}$ thick ($Q \approx 10000$).	98
6.10	Measurements, u-shaped layout: vibration amplitude for $200 \mu\text{m}$ long bridges as a function of the electrode length L_e for different electrode width W	100

6.11	Measurements, u-shaped layout: vibration amplitude for 200 μm long bridges as a function of the electrode length L_e for different electrode spacing S	102
7.1	Schematic of the designed Al/SiC bridge resonators: slab electrode layout with actuation voltage V_{in} applied.	106
7.2	Simulations, slab layout: absolute maximum displacement for 150 μm long bridges actuated with the slab electrode layout (inset: snapshot with slab electrode length $L_e = 75 \mu\text{m}$).	107
7.3	Simulations, slab layout: temperature data of 150 μm long bridges for different electrode lengths L_e	108
7.4	Measurements, slab layout: resonant peak of an Al/SiC bridge resonator 150 μm long actuated electro-thermally with a slab electrode.	110
7.5	Measurements, slab layout: vibration amplitude as a function of electrode length L_e for 150 μm long bridges actuated with the slab electrode layout.	111
7.6	Simulations, slab and u-shaped layouts: maximum displacement as a function of the electrode length L_e for 150 μm long bridges.	112
7.7	Simulations, slab and u-shaped layouts: temperature data of 150 μm long bridges for different electrode lengths L_e	113
7.8	Measurements, slab and u-shaped layouts: vibration amplitude as a function of the electrode length L_e for 150 μm long bridges.	115
8.1	Schematic of the designed SiC rings.	120
8.2	Schematic of the designed electrodes on SiC rings.	120
8.3	Simulations: snapshot of the first mode shape for a SiC ring with $R = 80 \mu\text{m}$ and $h = 6 \mu\text{m}$	121
8.4	Simulations: results for the resonant frequency of SiC ring resonators as a function of the ring radius R for different hole radius h (inset: resonant frequency as a function of the hole radius for different R).	122
8.5	Simulations: snapshots with temperature distribution for rings with $R = 100 \mu\text{m}$ and $h = 6 \mu\text{m}$	124
8.6	Ring resonators: measured and simulated resonant frequency as a function of the ring radius R for hole radius $h = 6$ and $15 \mu\text{m}$	125
8.7	Ring resonators: resonant peak of an Al/SiC bimaterial ring with radius $R = 125 \mu\text{m}$ and hole radius $h = 15 \mu\text{m}$ ($Q \approx 12000$).	127
8.8	Measurements: snapshots of bimaterial Al/SiC rings actuated electro-thermally with double electrode configuration at atmospheric pressure. .	128
9.1	Schematic of a cantilever with one voltage applied to the top electrode. .	132
9.2	Schematic of a cantilever with two voltages applied to the top electrode. .	134
9.3	Scanning electron micrograph of one of the Al/SiC cantilevers used for the measurements.	135
9.4	Measurements, actuation and mixing: resonant peaks for a 200 μm Al/SiC cantilever.	136

9.5	Measurements, actuation and mixing: resonant peaks for a 50 μm Al/SiC cantilever.	137
9.6	Measurements: mixing amplitude detected for a cantilever 50 μm long, $f_1 - f_2 \pm \Delta f$, $f_1 = 1200 \text{ kHz}$ $f_2 = 255 \text{ kHz}$	139
9.7	Optical micrograph of one of the Al/SiC rings used for the measurements.	141
9.8	Measurements: actuation and mixing with a ring with $R = 190 \mu\text{m}$ $h = 15 \mu\text{m}$	142
9.9	Measurements: mixing with a ring with $R = 190 \mu\text{m}$ $h = 15 \mu\text{m}$	143
10.1	Schematic of the designed piezo-electric SiC cantilevers.	149
10.2	Simulations: static displacement and resonant frequency as a function of electrode length L_e of a SiC cantilever with $L_b = 200 \mu\text{m}$ actuated piezo-electrically with a voltage of 0.5 V.	151
10.3	Simulations: harmonic displacement as a function of the shift from the resonant frequency for different electrode length L_e ($L_b = 200 \mu\text{m}$, actuation voltage = 0.5 V).	152
10.4	Butterworth - Van Dyke equivalent representation for electro-mechanical resonators.	153
10.5	Simulations of equivalent electrical circuit: impedance change at resonance for different values of C_p	155
10.6	Schematic of the testing system setup for the piezo-electric driving (actuation and sensing) of the fabricated cantilevers.	156
10.7	Measurements: electrode impedance (magnitude and phase) of a SiC cantilever 150 μm long actuated piezo-electrically.	157
10.8	Measurements results: impedance change as a function of frequency shift from resonance for a SiC cantilever 200 μm long actuated piezo-electrically with electrode length $L_e = 200$ and 100 μm	159
10.9	Scanning electron micrograph of the Pt/PZT/Pt electrode showing the three cuts performed with the FIB tool.	160
10.10	Measurements results: impedance change as a function of frequency shift from resonance for different values of C_p	161
11.1	Schematic of SiC bridge with top electrodes for electro-thermal actuation and piezo-electric sensing.	173

List of tables

2.1	Si and SiC material properties.	14
3.1	Piezo-electric material properties.	43
5.1	Measured resonant frequencies.	78
A.1	Material properties used in the finite element simulations.	175
A.2	Material properties used in the finite element simulations.	176
C.1	Measured resonant frequencies.	179
C.2	Young's modulus calculated from the measured resonant frequencies. . .	180

Acronyms and abbreviations

IC	Integrated circuits
RF	Radio frequency
Cantilevers	Single clamped beams
Bridges	Double clamped beams
Rings	Circular membranes with a central hole (i.e. annulus)
Si	Silicon
Poly-Si	poly-crystalline Si
SiC	Silicon carbide
SiO ₂	Silicon dioxide
SiN	Silicon nitride
Al	Aluminium
Au	Gold
Pt	Platinum
Ti	Titanium
PZT	Lead zirconium titanate
AlN	Aluminium nitride
ZnO	Zinc oxide
SF ₆	Sulfur hexafluoride
O ₂	Oxygen
XeF ₂	Xenon difluoride
CF ₄	Carbon tetrafluoride
H ₂	Hydrogen
SiCl ₄	Silicon tetrachloride
CVD	Chemical vapour deposition
APCVD	Atmospheric pressure chemical vapour deposition
LPCVD	Low pressure chemical vapour deposition
PECVD	Plasma enhanced chemical vapour deposition
RIE	Reactive ion etching
ICP - RIE	Inductively coupled plasma - reactive ion etching
TCE	Thermal expansion coefficient
XRD	X-ray diffraction
FIB	Focused Ion Beam
E	Tensile modulus or Young's modulus
ρ	Mass density
k	Spring constant
ϵ_0	Electrical permittivity of vacuum
TCE, γ	Thermal expansion coefficient
TCR	Temperature coefficient of resistance

L_b	Beam length
L_e	Electrode length
W	Electrode width
S	Electrode spacing
R	Ring radius
h	Ring's central hole radius
T_{av}	Simulated average temperature of the SiC beam when electro-thermal actuation is performed
T_{max}	Simulated maximum temperature of the SiC beam when electro-thermal actuation is performed
ΔT_z	Simulated vertical temperature difference in the SiC beam when electro-thermal actuation is performed
$\Delta T = T - T_0$	Simulated temperature difference between final and initial temperature in the SiC beam when electro-thermal actuation is performed

Chapter 1

Introduction

This chapter presents an introduction to micro electro-mechanical systems (MEMS) summarising the history and technology developments. Furthermore, the existing and emerging MEMS market and the related applications will be discussed together with some considerations on MEMS resonators as a new potential application. A brief review on silicon carbide (SiC) and its emergence as a semiconducting and mechanical material will be presented. The end of the chapter is dedicated to the thesis plan with the list of the next chapters and a short summary of their contents.

1.1 Micro-electro-mechanical systems

Micro electro-mechanical systems are integrated micro-scale mechanical and electrical elements, usually sensors and actuators, realised using micro-fabrication technology. Despite the term “MEMS” was first introduced by the end of the 1980s, electro-mechanical systems have been used long before for implementing “macro” devices including accelerometers, ceramic filters and reference oscillators. The ability of reducing the size of electro-mechanical systems has given the possibility of using batch processes developed extensively for integrated circuit (IC) fabrication. Consequently, the man-

ufacturing of one single device has been replaced by the simultaneous production of numerous devices on the same wafer thus reducing the fabrication time and costs.

Electro-mechanical accelerometers have been the first devices replaced by Si MEMS for employment in the automotive industry. Furthermore, since MEMS accelerometers were introduced in the market, new devices have been developed for a range of growing applications [1]. In particular, in the last two decades, MEMS devices including accelerometers, gyroscopes, micro-mirrors, switches, pressure and chemical sensors have been developed for various technological fields from biomedical applications to telecommunications, optics, automotive and entertainment industry.

1.1.1 History of MEMS

The development of micromachining technology is linked to the growth and progress of IC fabrication. In 1959, *Feynman*, during his famous lecture “Plenty of room at the bottom”, considered the advantages of technology miniaturisation and reflected about the possibilities and issues related to the making of “small but movable machines” [2].

The first MEMS devices have been developed in the 1960s when researchers started to turn attention to the manufacturing of mechanical systems using existing IC fabrication technology. In 1967, *Nathanson et al.* described the “resonant gate transistor” formed by a micro-fabricated single clamped beam (cantilever) driven electro-statically and used as a suspended gate over a transistor [3]. In 1968, *Wilfinger et al.* reported another device called the “resonistor”: a cantilever driven into vibration by electro-thermal transduction [4]. In the 1970s, the idea of commercialising microdevices such as accelerometers and pressure sensors started to be regarded with more interest. In 1974, National Semiconductor introduced into the market the first Si pressure sensors with piezo-resistive sensing. Few years later, in 1977, the first capacitive pressure sensor was demonstrated at Stanford. In the same years, attention was driven towards new devices such as the micro-mechanical light modulator reported by *Petersen* [5].

In the 1980s, the potentials of MEMS were established attracting a growing interest from the semiconductor industry. In those years, the role and the importance of Si for MEMS applications were recognised and highlighted by *Petersen* in his review “Silicon as mechanical material” [6]. The use of poly-crystalline silicon for fabricating micro-mechanical beams was reported in 1983 [7]. Few years later, in 1987, micro structures moving unrestrainedly in one or more degree of freedom were fabricated successfully thus opening new frontiers in the field of micromotors and other types of actuators [8] [9] [10].

In the 1990s, low-cost micro-mechanical pressure sensors and accelerometers became available commercially and introduced mainly in the automotive market. However, beside the employment as sensor devices, MEMS started to be used widely as actuating devices thus leading to the development of other applications such as inkjet printers, fuel-injection systems and digital microdisplays.

In the last decade, MEMS devices have started to be explored for the development of a variety of sensors and actuators. Devices such as gyroscopes, microphones, spectrometers and chemical sensors are part of the emerging MEMS sensing technologies. In addition, a lot of effort has been made to integrate micro switches and resonators in optical and radio frequency components. Large progresses are made every year in the area of biomedical MEMS-based systems such as lab-on-chip and drug delivery devices. Radio frequency (RF) MEMS are attracting an increasing interest for solving power consumption and miniaturisation issues in remote sensors and transceiver devices [11]. The most recent frontier in MEMS technology includes applications in the fields of alternative energy harvesting and quantum mechanics [12] [13].

1.1.2 MEMS market

In the 1990s, the development of low cost micro-mechanical devices such as pressure sensors and accelerometers has contributed to a boost in the growth of the MEMS

market. The automotive industry has been the first major consumer leading to a decrease of the price of the devices that opened MEMS to other industry fields. It has been estimated that in 2005 MEMS-based IC devices have created a market of \$ 8 billion with predictions growing to \$ 40 billion by 2015 [14].

Fig. 1.1 shows a schematic for the MEMS market distribution in 2009 [1]. In the last 5 years, MEMS technology has spread mainly among the fields of inkjet printers, pressure sensors, inertial sensors (accelerometers and gyroscopes), optical devices (digital microdisplays) and microphones. These few applications seem to produce profits over \$ 500 million per year. Profits from emerging applications employing RF and optical devices, spectrometers and biomedical systems are estimated in the order of \$ 100 million per year and are believed to grow in the next years [1] [14].

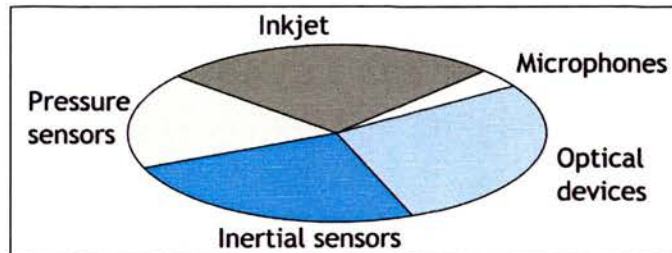


Figure 1.1: MEMS market in 2009 [1].

1.1.3 Radio frequency MEMS

In the last decade, the increasing demand in wireless communication systems has contributed to the boost of RF MEMS applications. Research in this field aims towards the reduction of the size and power consumption of the devices. Despite the progress in the IC technology, the chip scaling in the front-end of wireless devices is limited by the relatively large size of numerous off-chip passive components [15]. As a matter of fact, a large area of the printed board in wireless devices is taken generally by inductors, capacitors, switches, filters and resonators that are of key importance for performing the essential function of radio transceivers.

Due to the need of smaller and more efficient wireless devices, RF MEMS are considered as the possible “killer” application that could contribute to a further increase of the overall MEMS market. In 2007, RF MEMS have reached a market of \$ 250 million [16] with growing expectations to \$ 1 billion in 2015.

The final goal of RF MEMS researchers is to fully integrate all the passive devices into a single chip thus leading to consistent reduction of the printed board area of the transceiver. Fig. 1.2 shows a possible solution for the replacement of some of the passive components with RF MEMS devices in a GSM transceiver chipset [17].

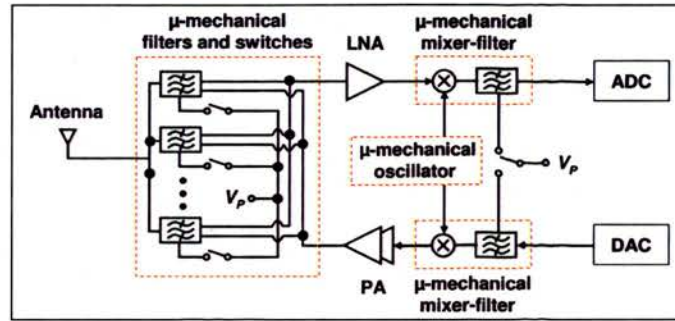


Figure 1.2: RF MEMS devices integration in a transceiver circuit (simplified from [17]).

1.1.4 MEMS resonators

MEMS-based oscillators occupy a niche of the market with profits \sim \$ 5.2 million in 2008 [18]. In the last two decades, MEMS resonators have been considered for replacing quartz crystals used as frequency reference for clock and timing IC devices. The excellent mechanical properties and low cost fabrication process of quartz crystals make these devices optimal for IC timing components [19]. However, drawbacks such as relatively large sizes, sensitivity to heat and shocks and higher failure rate than IC circuits appear to be major constraints for the miniaturisation of the devices used in automotive, wireless, entertainment and computer applications [19]. MEMS-based oscillators are expected to overcome the issues related to quartz crystals. As a matter of fact, thanks to the progress of IC technology and developments of new packaging

techniques, MEMS resonators have achieved levels of performance and temperature stability that make them really competitive with quartz crystals.

In the last years, SiTime Corp. has introduced into the market a Si resonator stacked on top of a CMOS driving chip. The entire package occupies an area of few square millimetres that is comparable with the dimensions of a quartz crystal without considering the driving circuitry [19].

The package proposed by SiTime does not integrate MEMS and CMOS devices on the same chip. As for the case of RF MEMS, one of final objectives is the complete single-chip integration of all the components forming the oscillator. The integration of the resonator, the reference oscillator circuit, the phase-locked loop and the temperature compensation circuit on the same substrate will allow smaller devices and package sizes thus facilitating high-volume assembly processes [20]. However, the single-chip integration is currently limited by issues related to the costs of packaging and encapsulation, temperature stability, phase noise and power consumption [20].

1.2 Silicon carbide

In this section, the main steps of the evolution of SiC as a semiconducting and mechanical material are summarised. A more detailed discussion on SiC properties together with a review on SiC growth and devices manufacturing will be given in Chapter 2.

A brief history of SiC is provided by *Brezeanu* in [21]. In the 1890s, SiC was synthesised for the first time by *Acheson* and in 1905, a SiC crystal was found by *Moissan* in a meteorite. Similar to Si, SiC has evolved as a semiconductor material first. In 1955, *Lely* developed a process to grow SiC crystals but the difficulties in obtaining high quality crystals limited the interest of the scientific community. In 1978, the first SiC wafer was produced by seeded sublimation growth and few years later SiC layers were grown epitaxially on Si substrates. At the end of 1980s, Cree Inc. started to produce

high-quality SiC epitaxial layers grown at low temperatures. In the same years, the first SiC prototypes of high frequency devices and light emitting devices were reported. Since the end of the 1980s, due to its electrical characteristics such as large bandgap, high saturation velocity and large breakdown voltage, SiC has shown to be an optimum material for electronics devices operating at high temperatures and frequencies and requiring relatively low power consumption [22] [23].

In the 1990s, the potentials of SiC as a mechanical material have started to be regarded with growing interest [24] [25] [26] [27]. As a matter of fact, SiC exhibits excellent mechanical strength, high elastic moduli, high thermal conductivity and stability and chemical inertness to most acids. In the last two decades, because of its outstanding electrical and mechanical properties, SiC has attracted a lot of attention and consequently stimulating the improvement of the growing and etching techniques. High quality SiC substrates and epilayers can now be produced together with a wide variety of SiC MEMS devices that have shown high robustness and reliability. Furthermore, it is believed that SiC could overwhelm Si in many MEMS applications such as resonators and transducers operating in high-temperature harsh environments [28] [29]. Details of SiC crystal structure, growth, etching and a brief review on SiC MEMS devices will be given in the next chapter.

1.3 Thesis plan

The work presented in this thesis has been motivated by the fact that SiC is an excellent candidate for the implementation of MEMS devices for RF applications. As mentioned above, RF MEMS are believed to be one of the solutions to lead to a new generation of wireless communication devices. The attention has been focused on SiC resonant devices that could be employed as reference oscillators. Furthermore, resonators could be used to perform filtering or mixing functions generally carried out by analogue circuits.

One of the first objectives has been to develop a repeatable and relatively simple fabrication process flow for manufacturing SiC MEMS devices. Then, once the devices could be fabricated, electro thermal transduction has been investigated as actuation mechanism focusing on the optimisation of the structure design for enhancing the actuation efficiency in terms of induced displacement and vibration amplitude. In addition, circular architectures have been compared to rectangular ones for inspecting the frequency range achievable and the ability of performing mixing functions with the fabricated resonators has been analysed. Moreover, piezo-electric driving of the SiC resonators has been explored in order to examine the possibility of sensing electrically the resonance of the structures.

Chapter 2: Silicon carbide for MEMS applications

The crystal structure and mechanical properties of SiC are introduced. A summary of the most common growing and etching techniques is presented followed by an overview on SiC MEMS devices reported in the literature of the last two decades.

Chapter 3: MEMS actuators: basic structures and transduction techniques

In this chapter basic structures such as flexural beam and disk flexural resonators are discussed and their fundamental natural frequency compared. In addition, electro-thermal, piezo-electric and electro-static transductions are introduced, examined and compared as mechanisms for driving flexural mode resonators. Some examples taken from the literature are also reported.

Chapter 4: Design and fabrication of SiC MEMS

The process flow developed for the manufacturing of SiC devices is described giving details on the etching and release of single material SiC beams. Additional steps are introduced for the implementation of metal (Al and PZT) electrodes on top of the devices. The process flow is then adapted and characterised for the fabrication of SiC rings.

Chapter 5: Characterisation of SiC

Two different SiC epilayers utilised for the devices fabrication are characterised. Raman spectroscopy and X-ray diffraction are introduced as materials characterisation techniques. The results obtained from the measurements are discussed. The elastic moduli of the epilayers is calculated from the resonant frequency of the fabricated cantilevers actuated with an external mechanical excitation.

Chapter 6: Electro-thermal actuation of SiC double clamped beam resonators with u-shaped electrodes

The results from the electro-thermal simulations and measurements of the fabricated Al/SiC double clamped beams (bridges) with u-shaped electrodes are discussed. The influence of the electrode dimensions on the thermo-mechanical behaviour of the devices is investigated in order to maximise the displacement and vibration amplitude at resonance of the structure.

Chapter 7: Electro-thermal actuation of SiC double clamped beam resonators with slab electrodes

A slab electrode configuration is analysed with the same methodology used in the previous chapter. The displacement and vibration amplitude induced electro-thermally are investigated as a function of the electrode dimensions. Furthermore, the results for the slab and u-shaped architectures are compared in order to determine the most efficient actuating electrode.

Chapter 8: Study of the mechanical behaviour and electro-thermal actuation of SiC ring resonators

In order to explore the possibility of achieving higher frequencies than beam structures, single material SiC and bimaterial Al/SiC rings are fabricated, simulated and tested. Therefore, particular attention is focused on the dependence between the structure's dimensions and the resonant frequency. The results obtained from the mechanical and electro-thermal actuation of the devices are presented. Different designs for the actuating electrodes designs are considered in order to assess the most efficient configuration

for performing electro-thermal actuation.

Chapter 9: Electro-thermal mixing with bimaterial Al/SiC resonators

Electro-thermal actuation is used to perform the mechanical mixing of two input frequencies. The theory of electro-thermal actuation is recalled to demonstrate the mixing principle. The measurements performed on bimaterial Al/SiC cantilevers and rings are shown.

Chapter 10: Piezo-electric driven SiC single clamped beam resonators

In this chapter, piezo-electric transduction is investigated as an electro-mechanical actuation and sensing technique. The SiC cantilevers fabricated with PZT electrodes on top are simulated and tested. The influence of the electrodes dimensions on the electro-mechanical coupling are investigated with the aim of maximising the electrical output.

Chapter 11: Conclusions and future work

An overall summary and review of the main results presented in the previous chapters is given. Some suggestions for future work and investigations are discussed together with the possible use of the major findings of this work for RF MEMS applications.

Chapter 2

Silicon carbide for MEMS applications

2.1 Introduction

As mentioned in Chapter 1, in the last two decades, silicon carbide (SiC) thin films have started to be employed for a wide range of electro-mechanical applications. In particular, due to its unique mechanical properties, SiC is an excellent candidate for the implementation of robust and reliable MEMS sensors and high frequency devices with high Q-factors. The emergence and advancement of SiC technology has been observed in parallel with and most likely promoted by the developments of Si MEMS applications.

The aim of this chapter is to describe the technology framework for the fabrication of SiC MEMS devices introducing the SiC structure, properties and manufacturing techniques.

In the first half of the chapter, the crystal structure and mechanical properties of SiC are introduced briefly. Then, a summary of growth, etching and micromachining techniques available for SiC thin films and substrates is presented. The discussion is addressed to

introduce the use of SiC layers particularly for the fabrication of mechanical structures.

The second half is dedicated to a general overview on SiC MEMS devices focusing on the main research works reported in the literature in the last two decades.

2.2 SiC properties

This section describes briefly the classification, structure and properties of different types of SiC crystals.

A polymorph material is a material that can exist in different structural forms. SiC exhibits a polymorphism called polytypism where the structural difference is observed in only one dimension. A detailed discussion of SiC polytypes is given by *Bechstedt* and *Willander* in [30] and [31], respectively.

The basic atomic structure of SiC is represented by a silicon (Si) atom and three carbon (C) atoms bonded tetrahedrally together. All the SiC polytypes have an identical planar arrangement of the Si and C atoms. The planes of Si and C atoms are referred as Si-C bilayers and can be viewed as a planar sheet of Si atoms linked to a planar sheet of C atoms. The C atoms of the Si C bilayers are arranged in a hexagonal pattern and every bilayer can be associated to a precise arrangement and orientation of its C atoms.

Fig. 2.1 shows a schematic representation of the position of the C atoms in the Si-C bilayers. In order to maintain the tetrahedral bondings, the Si-C bilayers can assume only three possible orientations that can be associated to the positions of the C atoms and denoted with the letters A, B and C (Fig. 2.1(a)). The differences in the stacking periodicity along one direction (i.e. one-dimensional variations) of the Si-C bilayers with different orientations A, B or C determine the SiC polytype and consequently its crystalline structure (Fig. 2.1(b)).

Despite the fact that more than 200 SiC polytypes exist, only three different crystalline structures have been observed: cubic, rhombohedral and hexagonal. The nomenclature

for SiC uses a letter for defining the crystalline structure and a number to define the stacking periodicity. For example, with this convention, 3C-SiC refers to a cubic (C) crystal with a stacking periodicity of 3 (ABC) (Fig. 2.1(b)) or 6H-SiC refers to a hexagonal (H) crystal with a periodicity of 6 (ABCACB) (Fig. 2.1(c)).

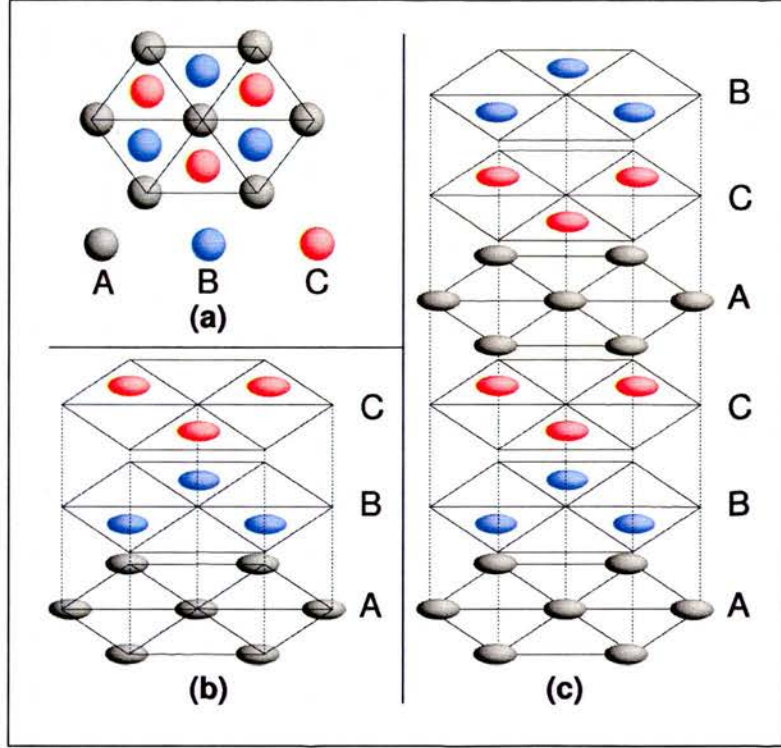


Figure 2.1: Si-C bilayers and their orientations to form SiC polytypes: (a) position of C atoms in the Si-C bilayers; (b) stacking sequence for 3C-SiC; (c) stacking sequence for 6H-SiC.

The differences in the Si-C bilayers stacking sequence lead to different electrical properties (such as bandgap or carriers mobility). On the contrary, all SiC polytypes show similar mechanical properties. As a matter of fact, all polytypes exhibit unique hardness and wear resistance characteristics that make SiC particularly suitable for harsh environment and high reliability applications. Furthermore, SiC is resistant to most of the acids and does not melt but decomposes at about 2730 °C. In addition, the Young's modulus of single crystalline SiC is in general relatively high (> 400 GPa) and much higher compared to the Si one (~ 190 GPa). Table 2.1 summarises and compares some

of the main properties of Si, 3C-SiC and 6H-SiC [27] [32].

Property	Si	3C-SiC	6H-SiC
Young's modulus [GPa]	190	420	440
Mass density [kg/m ³]	2330	3210	3210
Thermal conductivity [W/m °C]	170	360	490
Thermal exp. coeff. (TCE) [10 ⁻⁶ /°C]	2.6	3.28	3.25
Phase change temp. [°C]	1415	2730	2730

Table 2.1: Si and SiC material properties.

2.3 SiC growth

An overview on the techniques developed for the growth of SiC is presented. A detailed summary and discussion on SiC growth methods is given by *Mehregany* in [27] and by *Cheung* in [29].

Single crystalline SiC layers are grown epitaxially by atmospheric pressure chemical vapour deposition (APCVD) or by low pressure chemical vapour deposition (LPCVD) at relatively high temperatures usually ranging between 1300 °C and 1700 °C. The most common gases used are hydrogen (H₂) as a carrier gas and silane (SiH₄) and propane (C₃H₈) as precursor gases.

If aiming to high-temperature and high-power microelectronics applications where high quality single crystalline films are needed, the hexagonal polytype 6H-SiC is preferred [31]. High quality crystal 6H-SiC layers can be grown homoepitaxially by APCVD. The doping process is performed commonly *in – situ* during the SiC growth. Doping by diffusion after growth is arduous due to diffusion limitations and chemical inertness characteristic of SiC. Ion implantation can be used when a good controllability of the doping process is demanded nevertheless requiring very high temperatures in order to activate the implanted dopants.

3C-SiC is often preferred to 6H-SiC because of the possibility of growing it either

heteroepitaxially by APCVD [25] or by LPCVD [33] [34] on Si substrates thus making it more suitable for micromachining processes. The heteroepitaxial growth of 3C-SiC on Si substrates is practicable due to the similarities between the two cubic structures. The difference between the two materials' lattice constants ($\sim 20\%$) is solved with the carbonisation process. In fact, when performing heteroepitaxial growth, the Si substrate is heated up to $\sim 1300^\circ\text{C}$ and first exposed to a C precursor gas. Under these conditions, hydrocarbon reactants dissociate from the precursor gas and bond to the exposed Si surface thus converting into a thin layer of SiC. The reaction between the C-based gas and Si atoms is limited to the surface of the substrate due to the large SiC intrinsic diffusion barrier. After the initial carbonisation of the surface, the Si-based precursor gas is added and the process continues by homoepitaxial growth on top of the thin SiC layer [27].

Heteroepitaxial growth allows producing layers of single crystalline 3C-SiC on single crystalline Si substrates. In addition, poly-crystalline orientations can be obtained by APCVD or LPCVD on Si substrates or on various other layers, such as poly-Si, silicon oxide (SiO_2) or silicon nitride (Si_3N_4) previously deposited on Si substrates [35] [36]. The developments and improvements in the growth using Si substrates have allowed producing 3C-SiC layers on a larger scale and with more reasonable costs compared to the 6H-SiC substrates. Furthermore, the ability of growing SiC on a different range of materials provides a flexible system for the manufacturing of MEMS devices [29] [37].

2.4 SiC etching

The growth of SiC on different materials and in particular on Si substrates permits the use of conventional micromachining processes developed already for Si MEMS devices [28]. This section illustrates the techniques reported in literature for fabricating SiC MEMS.

The unique properties characteristic of SiC such as hardness and inertness to acids

that make it an attractive material for harsh environment applications, at the same time make the etching process relatively difficult. In fact, SiC is not etched by the acid or base solutions used at room temperatures for typical micro-fabrication processing. Therefore, wet etching of SiC requires the use of Molten Salts at temperatures typically higher than 300 °C [29].

Photoelectrochemical (PEC) etching is used mostly as a wet technique thus avoiding high temperatures and high corrosive solutions. Photo-enhanced etching can be performed on large areas and different solutions for selective and anisotropic etching have been developed. However, as a wet technique, PEC etching is not feasible for patterning small features or when smooth surfaces morphologies are required [29].

For these reasons, dry etching techniques are preferred when patterning SiC microstructures. In particular, reactive ion sources (RIE) have been shown to be convenient to etch SiC by using gases that contain chlorine (Cl) or fluorine (F) [38] [39]. One of the first and main reviews discussing the etching mechanism and properties of SiC in fluorinated plasmas has been published by *Yih et al.* in 1997 [40].

It is important to understand that, due to the large bonding energy between the Si and C atoms, the plasma source needs to produce high energy and high density ions in order to achieve reasonably fast etching rates. As a consequence, inductively coupled plasma - reactive ion etching (ICP-RIE) has become one of the most common etching mode for SiC. Generally, in ICP-RIE tools, the plasma density and the bias voltage can be controlled separately from the chamber pressure making the system quite versatile and permitting to achieve a high degree of anisotropy using low bias voltages [39] [41]. The effectiveness of Cl-based and F-based plasma has been compared in different papers [32] showing that chlorinated plasmas induce less surface damages but achieve much lower etching rates compared to fluorinated plasmas [38] [39]. Deep SiC etching has been demonstrated with an ICP-RIE system using a SF₆ plasma attaining etching depths of $\sim 100 \mu\text{m}$ [42].

In many micromachining processing, the etching rate play a key role due to the relatively large thickness of the layers that have to be patterned. Therefore, the fast etching rate achievable using F-based plasmas has stimulated many research efforts towards the optimisation of this process.

The addition of other gases to the process can increase the etching rate, reduce the surface damages and prevent micromasking. When fluorinated plasmas are used, the generated volatile etch products such as SiF_x and CF_x are removed easily from the chamber, consequently not limiting the etching speed. However, it has been shown that the addition of a small amount of oxygen O_2 (20%) to SF_6 gases increases the etching rate probably because of the liberation of more F atoms and the formation of more volatile products such as CO_x and COF_2 [43]. The addition of O_2 has the beneficial effect of enhancing the formation of volatile products hence preventing possible micromasking effects due to the redeposition of residues containing C [32]. However, if a relatively large amount of O_2 is introduced, the etching rate has been observed to decrease probably because of the overall reduction of F gas available thus limiting the removal of the Si atoms [43] [44].

It is important to point out that because of the high power density employed and the use of O_2 in the gas mixture, the commonly used photoresists do not last long enough for etching SiC layers thicker than a few microns. In this case, more resistant masking materials such as nickel (Ni), indium tin oxide (ITO) or silicon dioxide (SiO_2) are required [38] [45].

2.5 SiC micromachining

The growing and etching techniques presented in the previous sections can be employed for the micromachining of SiC. Similar to Si MEMS, bulk and surface micromachining processes can be used for the fabrication of SiC structures [28]. The choice of the micromachining technique is usually related to the growth process used and consequently

to the type of substrates and sacrificial materials to be removed in order to obtain suspended and movable structures. This section discusses the use of the state-of-art micromachining techniques for the fabrication of SiC MEMS.

2.5.1 Bulk micromachining

In general, bulk micromachining is performed when the SiC epilayer is grown directly on top of the Si substrate that is consequently employed as a sacrificial material. With bulk micromachining, the sacrificial material can be removed from the bottom or from the top side of the wafer (i.e. back-side and front-side etching).

Fig. 2.2 shows a schematic diagram of the conventional bulk micromachining technique with back-side and front-side removal of the sacrificial material.

In the case of back-side etching (Fig. 2.2(a)), the Si substrate can be removed isotropically with wet solutions. In many cases the large undercuts arising from the use of wet solutions are avoided by wet crystallographic etching (KOH or TMAH) so that the bulk Si substrate can be removed anisotropically.

Front-side etching is performed by etching the Si substrates through via-holes patterned on the SiC epilayers as shown in Fig. 2.2(b). As in the back-side etching, usually anisotropic etching is preferred to obviate issues related to large undercuts.

The advantages of using SiC as a structural layer in bulk micromachining is that an etch-stop layer is not required because of the good selectivity between SiC and Si. In addition, the SiC is not attacked during the removal of the sacrificial layer due to the inertness towards the acids used.

Despite the feasibility of wet solutions to remove the sacrificial layer, some disadvantages, such as stiction between the structural and the sacrificial material or the need of critical point drying processes, could make the release process tedious and impractical. For these reasons, in some cases dry release approaches are preferred to wet solutions.

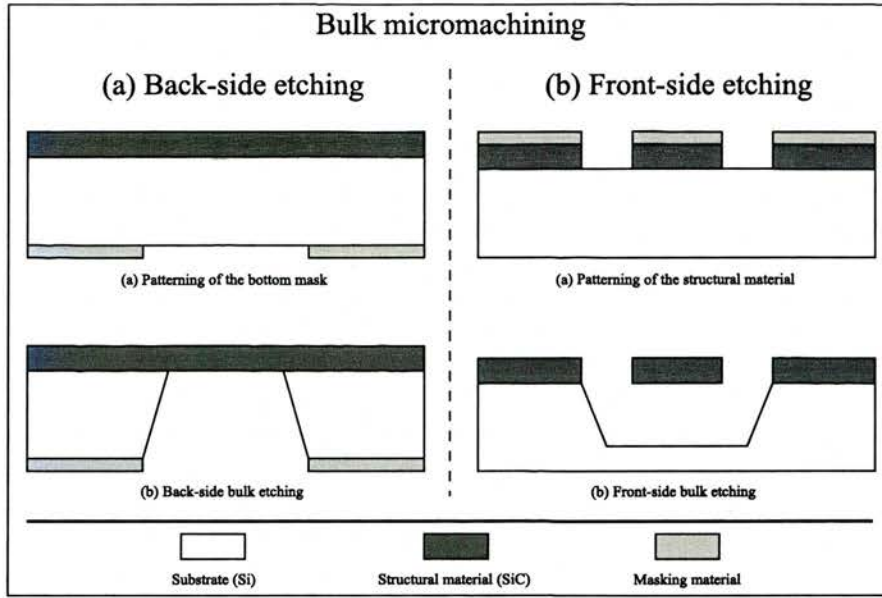


Figure 2.2: Schematic view of bulk micromachining with back-side and front-side etching.

For instance, xenon difluoride (XeF_2) in its vapour phase can be used as a releasing gas in front-side bulk micromachining. Recently, relatively high etching rates have been achieved with XeF_2 vapour making it particularly suitable for the removal of thick and large areas of Si sacrificial layers [46]. It is worth noting that dry vapour release techniques are isotropic thus requiring the control of the release rate in order to avoid large unwanted undercuts of the structures.

2.5.2 Surface micromachining

Surface micromachining is used when SiC layers are grown on top of substrates formed by layers of different materials (i.e. multi-layer substrates). Fig. 2.3 shows a schematic view of a typical surface micromachining process for SiC structures. In this case, the layer positioned directly below the SiC film is used as a sacrificial material. Polycrystalline SiC layer can be grown on top of poly-Si, SiO_2 or Si_3N_4 layers that are consequently used as sacrificial materials [47] [48].

Once the SiC film has been patterned and etched, the sacrificial layer can be removed

with wet or dry etching techniques. Similar to bulk micromachining, in order to avoid stiction and drying issues related to wet release processes, dry vapour release techniques can be used such as XeF_2 vapour [46] for poly-Si sacrificial layers or HF vapour [49] [50] for SiO_2 .

Surface micromachining is versatile for the fabrication of MEMS structures made of poly-crystalline SiC on various sacrificial materials while bulk micromachining is preferred when single crystalline SiC is grown on single crystalline bulk Si substrates.

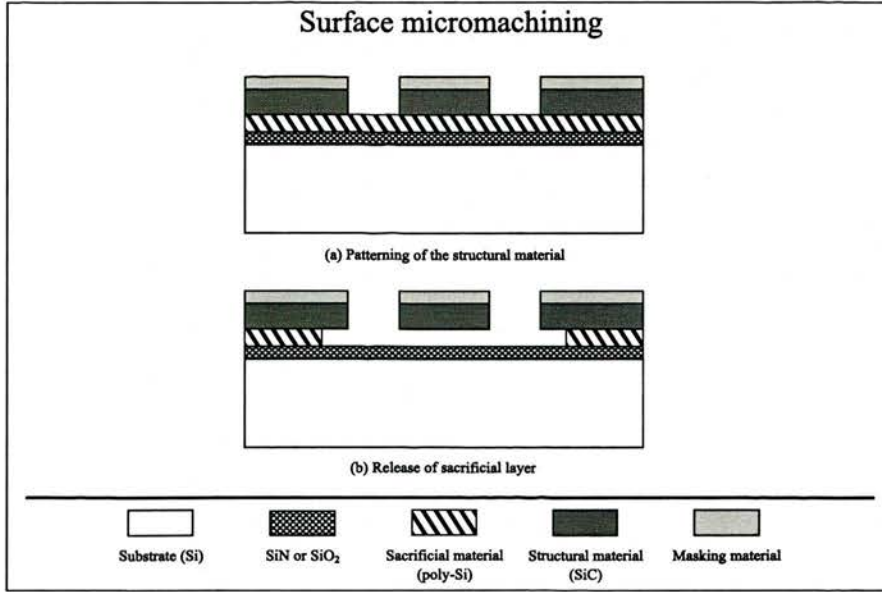


Figure 2.3: Schematic view of surface micromachining.

2.5.3 One-step etch and release

The fact that SiC can be grown on Si substrates or on poly-Si layers allows the possibility of dry etching both materials in the same fluorinated plasma [28].

A process that combines together the etch and the release of SiC films grown on Si substrates or on poly-Si layers has been developed by *Cheung et al* in 2003. In this process, the SiC is masked with a thick layer of PECVD SiO_2 and etched with an ICP-RIE with a SF_6/O_2 gas mixture. Once the SiC is etched, the Si exposed underneath

is attacked by the same fluorinated plasma allowing the etching and release of the SiC structures during the same fabrication step [43] [51].

Fig. 2.4 shows a schematic of the simplified process flow for the one-step etch and release process developed for SiC. As depicted in Fig. 2.4, this fabrication process can be utilised for front-side bulk micromachining of SiC films grown on Si substrates (Fig. 2.4(a)) [51] and for surface micromachining of SiC films grown on poly-Si layers (Fig. 2.4(b)) [52] [53] [54].

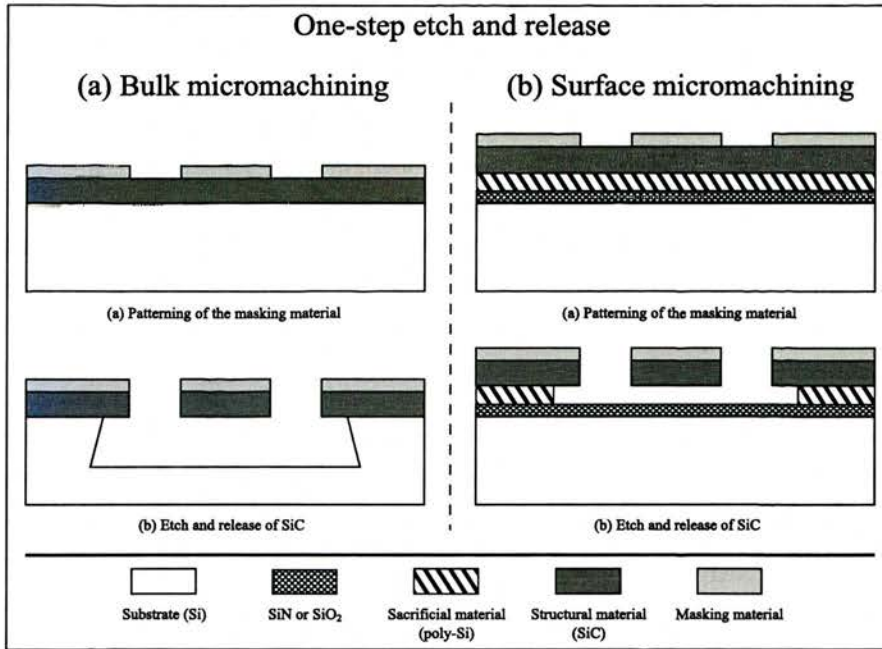


Figure 2.4: Schematic view of the one-step etch and release process for front-side bulk and surface micromachining.

2.6 SiC MEMS

As highlighted in the previous sections, bulk and surface micromachining techniques have been used widely in the past and are still being used for manufacturing MEMS. Si, SiO₂, SiN, Al and many other materials can be used as structural layers by adapting the micromachining techniques described above to the different processes. A similar

approach could be used with SiC due to the ability of growing single and poly-crystalline SiC on Si substrates and on poly-Si, respectively.

In order to highlight the developments and challenges concerning SiC MEMS, this section presents an overview on some of the SiC devices fabricated in the last two decades.

2.6.1 First devices: thermistors

SiC MEMS devices have started to be fabricated for sensor applications at the beginning of the 1990s. Temperature sensors have been manufactured initially with poly-crystalline SiC due to the ability of growing it on different substrates. One of the first MEMS devices has been a resistive temperature sensor (thermistor) that has been fabricated on an Al substrate in 1990 [55]. Later in 1996, the fabrication of poly-crystalline SiC thermistors on Si substrates has been reported [56]. These devices have shown a relatively good thermal stability when tested in a temperature range between 0 °C and 300 °C. Moreover, in comparison with the widely used metal thermistors, the temperature coefficient of resistance (TCR) has been shown to decrease slower as a function of the temperature.

2.6.2 Pressure sensors

In the late 1990s, the increasing need of pressure sensors applications for harsh environments has encouraged the implementation of more advanced devices with SiC suspended structures. The good thermal stability distinctive of SiC has made possible the employment of MEMS pressure sensing at high temperatures without the need of a cooling system.

6H-SiC layers have been used to demonstrate successfully the stable operation of pressure sensors at temperatures up to 500 °C [57]. N-type and p-type SiC epilayers have been used for the implementation of the piezo-resistors and of the membrane, respec-

tively. PEC has been used to perform bulk micromachining of the membrane and to define the piezo-resistors.

Later, 3C-SiC epilayers have been preferred for the development of SiC pressure sensors due to the low cost and flexible growth process. *Ziermann, von Berg, Eickhoff et al.* have given an important contribution to the developments of SiC pressure sensors using 3C-SiC on SOI (silicon-on-insulator) substrates [58]. The devices realised with SiC piezo-resistors positioned on top of Si diaphragms have been fabricated using a relatively simple manufacturing process employing RIE with a mixture of SF₆ and O₂. The devices have shown a linear output voltage as the temperature increased from 25 to 400 °C and a TCR of 0.16%/°C.

Pressure sensors with a similar structure have been developed by *Meheregany et al.*. In their process, 3C-SiC has been grown on top of Si substrates. The diaphragm has been implemented with the SiC by removing the bottom Si with bulk micromachining and the piezo-resistive elements have been implemented using poly-Si. The devices have been shown to have a TCR of ~0.14%/°C at 300 °C and a good thermal stability at 400 °C [27].

2.6.3 Accelerometers

An increasing interest in the design and fabrication of SiC accelerometers has been observed from 2001 aiming to harsh environment applications. For instance, in 2003, a bulk micromachined 6H-SiC piezo-resistive accelerometer has been reported by *Atwell, Okojie et al.* [59]. Different diaphragm configurations have been fabricated with p-type 6H-SiC substrates and etched with DRIE. The piezo-resistors made of n-type 6H-SiC grown epitaxially on the substrate have been placed on top of the diaphragm. The devices have been tested with different accelerations up to 40,000 g showing a signal output and sensitivity comparable to a commercially available system.

PECVD deposited SiC has been used by *Pakula et al.* to fabricate a CMOS compatible

vertical accelerometer [60] with Al electrodes. Due to the relatively low processing temperatures, the MEMS device could be fabricated on top of the CMOS readout circuit. The accelerometer has been designed with a SiC/Al/SiC membrane suspended on four SiC/Al springs. The output voltage has been shown to vary linearly when the acceleration was increased from 0.5 to 14 g [61].

2.6.4 Resonators

In parallel to the advancements in the fabrication of SiC pressure sensors and accelerometers, the use of SiC for implementing MEMS resonators has attracted great attention in order to develop devices more reliable than the Si ones. SiC MEMS resonators could find application as building blocks for different type of sensors and overcome issues related to operation temperature and reliability that limit the Si-based devices. The potentials of MEMS resonators for RF applications have been highlighted in Chapter 1.

In 1996-97, *Mehregany, Zorman et al.* reported the first prototype of SiC lateral resonator with electrostatic actuation [47]. The devices have been fabricated with poly-crystalline SiC thin films grown on top of poly-Si sacrificial layers. The SiC layer has been etched by RIE and the poly-Si released with KOH followed by a supercritical drying step used to avoid stiction problems. The performance of the SiC lateral resonators has been tested at temperatures up to 900°C showing a lower change in the average resonant frequency compared to the same devices fabricated with poly-Si [27].

In later works, these electro-statically actuated SiC lateral resonators have been improved and the performance of the devices tested at different temperatures [62] and different bias voltages [63]. The resonant frequency variations as a function of bias voltage have been shown to be lower than the ones obtained with similar poly-Si devices. Moreover, the increase in temperature has been shown to induce a non-linear increase of the resonant frequency due the interplay between variations in Young's modulus and induced thermal stress.

In a recent publication, the implementation of an oscillator based on a SiC resonator connected to a sustaining electronic circuit has been presented [48]. The device has been actuated with a 10 V DC bias voltage at 1 mTorr and has been shown to generate a sinusoidal waveform with a frequency of ~ 30 kHz and a power of -17 dBm.

An increasing interest in the field of micro-mechanical resonators has been observed in the last decade due to the continuous growth of wireless and radio frequency (RF) applications [64]. It is thought that the use of SiC for implementing resonant structures can improve the performance and the reliability of the devices and opens new perspectives for the application in harsh environments [29] [65]. As a matter of fact, due to unique properties such as high Young's modulus and relatively low mass density, SiC outperforms Si in terms of achievable resonant frequency and Q-factor. Single clamped and double clamped vertical resonator beams have been reported exhibiting resonant frequencies up to 5 MHz [52] [53] [66]. In addition, very high and ultra high frequencies (VHF and UHF) can be achieved with SiC nano-mechanical resonators. Resonant frequencies up to 700 MHz have been reported for SiC nano-resonators fabricated with electron beam lithography and actuated with magnetomotive transduction [67]. However, despite the very high working frequency, SiC NEMS suffer of unreliable signal outputs similar to Si NEMS.

2.7 Conclusions

SiC technology has developed widely in the last two decades. Since the beginning of the 1990s, when the first devices have been fabricated, great progress has been made in the growth and manufacturing processes. SiC is a very attractive material for harsh environments applications and high reliability devices due to its unique electrical and mechanical properties.

The crystal structure of SiC is determined by the stacking order of planar sheets (bilayers) composed by Si and C atoms. The differences in the stacking periodicity determine

the SiC crystal structure (polytype). There are many possible variations in the stacking periodicity but only cubic (C), rhombohedral (R) and hexagonal (H) crystal structures have been observed. 6H-SiC (hexagonal with periodicity of six) and 3C-SiC (cubic with periodicity of three) are the most largely used due to their excellent electrical and mechanical properties.

SiC can be grown by APCVD or LPCVD with silane (SiH_4) and propane (C_3H_8) precursors gases. 6H-SiC is homoepitaxially grown and mostly used for high-temperature and high-power microelectronics applications. For MEMS applications, 3C-SiC is preferred because the growth can be performed on various materials such as Si, SiO_2 or Si_3N_4 thus making it feasible for a wide range of processing techniques.

Due to the hardness, acid inertness and large atom bonding energy typical of SiC, reactive ion etching (RIE) techniques are used more often because of the high power and ion density that can be produced. In particular, inductively coupled plasma - reactive ion etching (ICP-RIE) systems utilising a fluorine-based gas (SF_6) have been shown to be quite efficient for achieving high etching rates and good degrees of anisotropy. However, masking materials such as SiO_2 or nickel (Ni) need to be employed because the standard photoresists are not suitable for the high power density used.

The micromachining techniques developed for Si MEMS can be adapted and employed for the manufacturing of SiC structures. The growth of SiC on different materials and the use of bulk and surface micromachining combined with dry release techniques have allowed the development of efficient process flows. In addition, the fact that SiC can be grown on Si sacrificial layers have endorsed the ability of etching the SiC and releasing the Si underneath in the same fluorine-based plasma. This *one - step etch and release* technique has been used as a part of the fabrication process flow for the SiC devices presented in this thesis (see Chapter 4).

The research on SiC MEMS has increased continuously since the 1990s. Initially, devices mainly for harsh environments applications have been studied and implemented.

Thermistors, pressure sensors and accelerometers fabricated using SiC have shown better performances than the corresponding Si devices. In addition, with the developments of the new generations of radio-frequency applications, SiC has started to attract more interest in order to implement high frequency resonators. The possibility of manufacturing SiC mechanical resonators with high Q-factors and good reliability has opened new perspectives for the on-chip integration of RF components.

On the grounds presented in this chapter, this thesis aims to add a contribution in the research of SiC MEMS addressing the development of resonating structures for RF applications.

Chapter 3

MEMS actuators: basic structures and transduction techniques

3.1 Introduction

In the previous chapter, the mechanical properties of SiC have been introduced focusing on MEMS applications and presenting some of the SiC MEMS devices reported in literature. As discussed, the compatibility of SiC with the state-of-art technology has allowed the possibility of utilising the well established Si fabrication techniques for manufacturing SiC MEMS.

This chapter aims to provide the framework for the design of MEMS vertical actuators, sensors and resonators summarising the background theory related to the structures' modal behaviour and transduction methods.

In the first part of the chapter, basic architectures such as beams and circular structures are presented discussing the fundamental mechanical formulas that describe their modal

behaviour. The introduction of these basic structures is necessary in order to provide the background for discussing the results obtained when analysing the fabricated SiC micro-mechanical devices.

The rest of the chapter is dedicated to the theory behind the most common transduction mechanisms employed as actuation and sensing techniques for MEMS devices. The electro-thermal, piezo-electric and electro-static mechanisms will be discussed together with a review on the relevant literature works. Particular attention will be focused on the electro-thermal and piezo-electric mechanisms as alternatives to the widely used electro-static excitation.

The fundamental analytical equations describing the mechanical response of a structure experiencing an electrical excitation will be introduced. The formulas presented for the electro-thermal and piezo-electric actuation will be used in the next chapters as a complementary tool to finite element simulations for explaining the results obtained.

In the concluding section, the different transduction techniques will be compared discussing their major advantages and drawbacks.

3.2 Basic structures

Electro-mechanical structures are characterised by the direction of the deflection and, when employed as resonators, by the fundamental resonant frequency. Flexural-mode resonators are mechanical structures that deflect in vertical (out-of-plane) direction [68]. In this section, the architecture schematics and the analytical formulas for the fundamental resonant frequency of flexural-mode beams and circular membranes are presented.

A mechanical resonator can be simplified as an undamped mass m attached to a spring. The natural resonant frequency f_0 can be calculated from the equation of motion and

written as:

$$f_0 = \frac{1}{2\pi} \sqrt{\frac{k}{m}}, \quad (3.1)$$

where the spring constant k is a function of the structure's geometry and material's tensile modulus (i.e. Young's modulus).

The fundamental resonant frequency of structures having various geometries can be calculated by solving the wave equations that characterise the motion of the structures. By applying the appropriate boundary conditions for flexural-mode resonators, the frequency results a function of the structure's dimensions and material characteristics such as mass density ρ and Young's modulus E .

Fig. 3.1 shows the schematic of the top and side views of the structures considered. For completeness, the wave equations for flexural mode beams and disks taken from [68] are reported below. However, the formulas of the resonant frequency will not be derived here but will be quoted from [68].

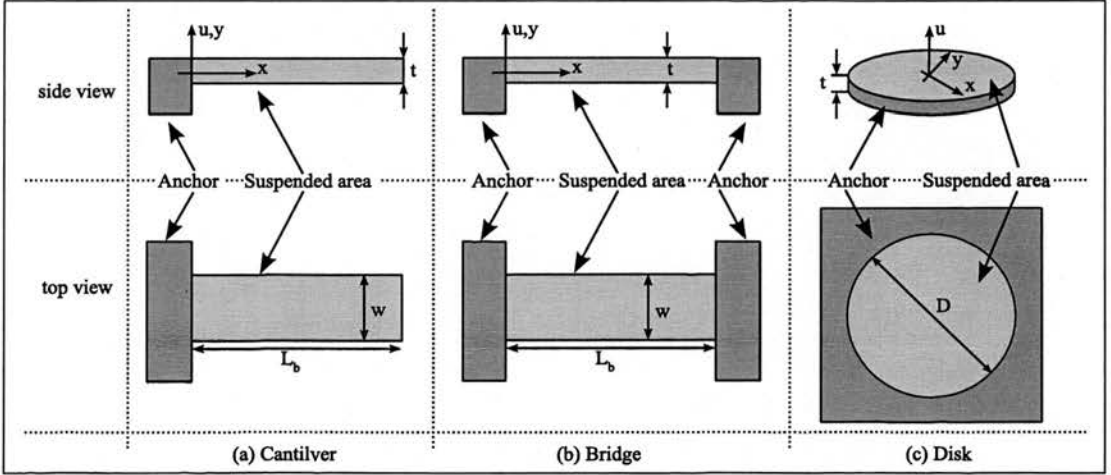


Figure 3.1: Schematics of the three basic structures used in this thesis: (a) single-clamped beam (i.e. cantilever), (b) double-clamped beam (i.e. bridge), (c) circular membrane (i.e. disk).

For a flexural mode beam (Fig. 3.1(a) and Fig. 3.1(b)) with thickness t and width w , if u is the vertical displacement and x is the coordinate along the beam, the wave

equation is of fourth order and is written as [68]:

$$\frac{\partial^4 u}{\partial x^4} = \frac{\rho A}{EI} \frac{\partial^2 u}{\partial t^2}, \quad (3.2)$$

where $A = wt$ is the cross-sectional area and $I = (wt^3)/12$ is the second moment of area.

For a flexural mode disk Fig. 3.1(c), if u is the vertical displacement and x and y are the coordinates on the surface of the disk, the wave equation is of fourth order and given in rectangular coordinates by [68]:

$$\frac{\partial^4 u}{\partial x^4} + \frac{\partial^4 u}{\partial y^4} + 2 \frac{\partial^4 u}{\partial x^2 \partial y^2} = \frac{1}{c^2} \frac{\partial^2 u}{\partial t^2}, \quad (3.3)$$

where c is the propagation velocity and its squared value can be written as a function of the disk's thickness t , Young's modulus E , mass density ρ and Poisson's ratio μ :

$$c^2 = \frac{Et^2}{12\rho(1-\mu)}. \quad (3.4)$$

3.2.1 Single-clamped beams - cantilevers

A single-clamped beam (i.e. cantilever) is defined as a flexural beam clamped on one side and free on the other side. Fig. 3.1(a) shows the schematic of a thin flexural-mode cantilever with the associated dimensions. The analytical formula for the fundamental resonant frequency f_C of a stress-free cantilever is given by:

$$f_C = 0.162 \sqrt{\frac{E}{\rho}} \frac{t}{L_b^2}, \quad (3.5)$$

where L_b is the beam length and t is the beam thickness.

3.2.2 Double-clamped beams - bridges

A double-clamped beam (i.e. bridge) is defined as a flexural beam clamped on both sides. Fig. 3.1(b) shows the schematic of a thin flexural-mode bridge with the associated dimensions. The analytical formula for the fundamental resonant frequency f_B of a stress-free bridge is given by:

$$f_B = 1.03 \sqrt{\frac{E}{\rho} \frac{t}{L_b^2}}, \quad (3.6)$$

where L_b is the beam length and t is the beam thickness.

3.2.3 Circular membranes - disks

A circular membrane (i.e. disk) is defined as a circle-shaped flexural membrane clamped all around its perimeter. Fig. 3.1(c) shows the schematic of a thin flexural-mode disk with the associated dimensions. In the case of disks, the calculation of the fundamental resonant frequency is much more complex compared to the beams cases [68]. However, for facilitating the comparison with Eq. 3.5 and Eq. 3.6, the final solution for the fundamental resonant frequency f_D of a stress-free disk has been simplified and can be written as:

$$f_D = 1.65 \sqrt{\frac{E}{\rho} \frac{t}{D^2}}, \quad (3.7)$$

where D is the disk diameter and t is the disk thickness.

3.2.4 Considerations on the fundamental resonant frequency

From Eq. 3.5, Eq. 3.6 and Eq. 3.7, it can be seen that the fundamental resonant frequency depends on the structure dimensions (t , L_b , D) and on the material properties (E , ρ). Therefore, the choice of the structure, dimensions and materials is very important for achieving different frequency ranges. For example, with regard to the material's choice, SiC has a relatively low mass density ρ and a high Young's modulus E . As a consequence, SiC devices are capable of achieving higher resonant frequencies

compared to Si ones. As for the structure's choice, for comparable dimensions, disks exhibit a fundamental resonant frequency ~ 10 higher than cantilevers and ~ 1.6 times higher than bridges. Fig. 3.2 shows the resonant frequency as a function of the structure dimensions for stress-free cantilevers, bridges and disks calculated with Eq. 3.5, Eq. 3.6 and Eq. 3.7. For this calculation, the material properties of 3C-SiC reported in Table 2.1 have been used (Young's modulus $E = 420$ GPa and mass density $\rho = 3210$ kg/m³). A thickness t of $2\text{ }\mu\text{m}$ has been chosen to match the one of the structures presented in the next chapters.

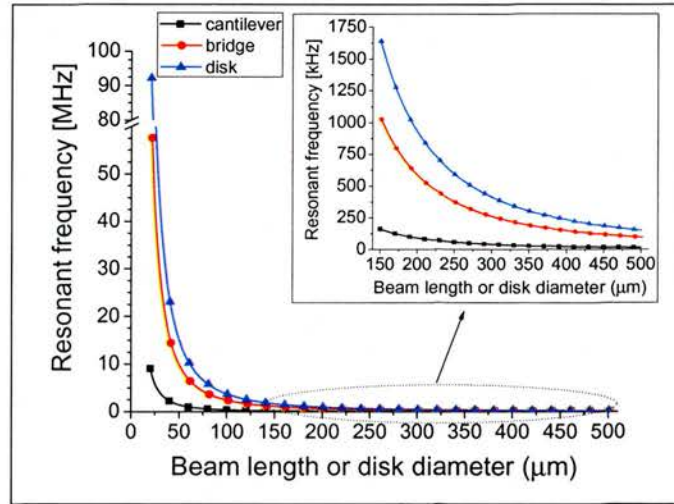


Figure 3.2: Analytical resonant frequency as a function of the structure's dimension for cantilevers, bridges and disks ($E = 400$ GPa, $\rho = 3200$ kg/m³, $t = 2\text{ }\mu\text{m}$).

It is worth pointing out that the analytical equations given in Eq. 3.5, Eq. 3.6 and Eq. 3.7 do not consider the effect of the intrinsic stress within the structures resulting from the used materials, their interaction and from the manufacturing processes (i.e. growth, etch and release) employed for the devices' fabrication. The overall effect of the stress is difficult to evaluate due to the contribution of different stress components such as the residual, thermal stress and the shear and anchor stress that comes from the interaction between the different materials forming the structure clamped to the substrate (i.e. electrodes, insulating layers and substrates).

In some cases, the influence of the stress on the resonant frequency can be predicted by introducing some approximations to simplify the mechanical model. In the particular case of bridges, if the beam is considered as a single material structure and the stress deriving from the strain induced by the substrate is neglected, the total intrinsic stress can be assumed to be equal to the residual stress σ_r . With these assumptions, the resonant frequency can be written as a function of the intrinsic stress as [69] [70]:

$$f_{B-\sigma_r} = f_B \left(\sqrt{1 + 0.295 \frac{\sigma_r L_b^2}{Et^2}} \right), \quad (3.8)$$

where f_B is the stress-free resonant frequency given in Eq. 3.6. From Eq. 3.8, it can be seen that for positive values of σ_r (tensile stress) the frequency increases, while for negative values (compressive stress) it decreases [70].

3.3 Electro-thermal transduction

This section describes the electro-thermo-mechanical (abbreviated as electro-thermal) transduction mechanism. First, a physical description of this excitation technique is given together with a brief review on the main literature works. Then, the formulas of the induced displacement for single material and bimaterial bridges are presented followed by a short discussion on the induction of vibrations and resonance to the structures.

3.3.1 Brief introduction

Electro-thermal excitation is a technique based on the electrically induced thermal expansion of a material. By applying a voltage across the material that is to be actuated, an electric current is dissipated thus generating Joule heat. Consequently, a temperature increase is experienced causing the material to expand. The degree of expansion depends on the thermal expansion coefficient (TCE) of the material.

The thermo-mechanical transduction effect can be amplified using multi-material structures. The most common multi-material devices are formed of two different materials (i.e. bimaterials). The two materials forming the structure are chosen to have different TCEs so that as the temperature increases, one material experiences a larger expansion than the other one thus resulting in an enhancement of the mechanical strain. One of the major advantages of bimaterial structures is that one of the materials can be used for the implementation of the heating electrode.

The theory of bimetallic structures has been discussed in detail by *Timoshenko* in 1925 [71] and one of the first MEMS devices reported in literature has been actuated electro-thermally by *Wilfinger et al.* in 1968 (see Chapter 1, Section 1.1.1) [4]. In their work, a p-type Si substrate has been used to fabricate a cantilever with top piezo-resistors implemented into an n-type epitaxial layer grown on top of the Si substrate. The top piezo-resistors have been used for actuating the cantilever and at the same time detecting its resonance. Further investigations and improvements have been carried out by *Othman* and *Brunnschweiler* in 1987 [72]. In their work, the bulk Si substrate has been used to fabricate the main structure while a top layer of poly-Si has been used to pattern the actuation electrode.

The choice of the materials for the design of electro-thermal transducers plays a key role in the devices' performance. Properties such as thermal and electrical conductivity, TCE and the Young's modulus are important for designing thermal transducers and are essential factors for meeting specifications such as displacement range or power consumption.

In the last two decades, different bimaterial structures have been studied and fabricated by combining various range of materials. Usually, the actuating electrode is fabricated with a metal layer deposited on top of the main structure to be actuated. A large number of beam-shape vertical actuators have been fabricated with Si, SiO₂ or SiN and using different metal such as aluminium (Al) or copper (Cu) as electrodes' materials [73]

[74]. Poly-Si circular membranes with a central hole (i.e. domes or rings) with top gold (Au) electrodes have been fabricated and electro-thermally actuated by *Reichenbach, Zalalutdinov et al.* showing resonant frequencies up to 17 MHz [75] [76] [77]. In 2006, the first SiC electro-thermal cantilever actuators fabricated with top platinum (Pt) and nichrome (NiCr) electrodes have been reported [53].

3.3.2 Displacement

The displacement of a structure subjected to a temperature change can be evaluated as a function of the structure's dimensions, the material's TCE, the induced temperature difference and the heated up area [71], [78]. In [74], the displacement of bimaterial cantilevers has been investigated as a function of the thickness of the two materials forming the structure. In the following paragraph, the formulas for the displacement of bridges subjected to a temperature change will be presented. These formulas have been taken from [78] and are obtained by making the general assumptions of simple beam theory:

- the beam length is much greater than width and thickness;
- the beam cross-section is constant along its axis;
- the plane sections of the beam remain plane;
- the deformation is small compared to the beam dimensions;
- the friction at the supports is neglected;
- the shear effects are negligible;
- the strain at the interface between two or more materials is the same;
- the beam edges are fixed.

3.3.2.1 Single material bridge

The displacement of a single material or bimaterial bridge can be predicted with a similar approach as the one used in [74] for bimaterial cantilevers. Fig. 3.3 shows the schematic of a single material bridge experiencing a uniform vertical temperature change ΔT_Z on an area whose length is $L_{\Delta T}$ [78].

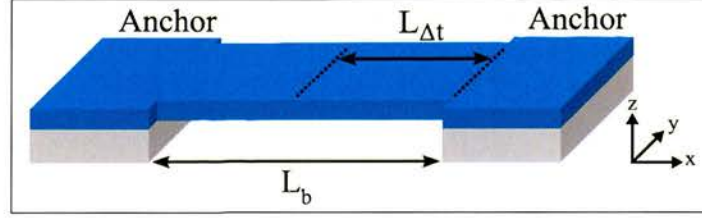


Figure 3.3: Schematic of a single material bridge.

In this case, the maximum deflection is given by:

$$z_{max} = \frac{1}{54} \frac{\gamma \Delta T_Z}{t} \frac{(2L_b - 3L_{\Delta T})^3 L_{\Delta T}}{(L_b - L_{\Delta T})^2}, \quad (3.9)$$

where L_b and t are the beam length and thickness, respectively, γ is the material's TCE and $\Delta T_Z = (T_B - T_T)$, with T_B and T_T bottom and top temperatures. In this case, the maximum deflection is directly proportional to the TCE of the beam material γ and to the vertical temperature difference ΔT_Z .

3.3.2.2 Bimaterial bridge

In the case of a bimaterial bridge, both materials' dimensions and thermo-mechanical properties have to be considered. Fig. 3.4 shows the schematic of a bimaterial bridge experiencing a uniform temperature change ΔT on an area whose length is $L_{\Delta T}$ [78].

Using subscript 1 and 2 for the top and bottom layers, respectively, and if top and bottom layers have the same width and length, the maximum deflection is given by:

$$z_{max} = \frac{1}{9} \frac{\Delta \gamma \Delta T (t_1 + t_2)}{K t_2^2} \frac{(2L_b - 3L_{\Delta T})^3 L_{\Delta T}}{(L_b - L_{\Delta T})^2}, \quad (3.10)$$

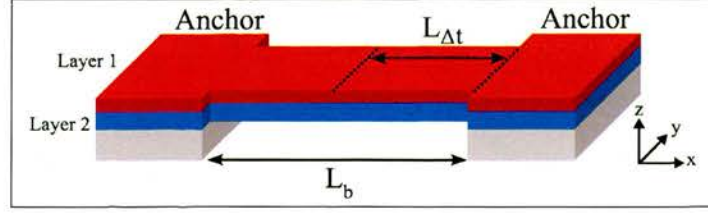


Figure 3.4: Schematic of a bimaterial bridge.

where L_b is the beam length, $\Delta\gamma = (\gamma_2 - \gamma_1)$ is the difference between the TCE of layer 1 and 2 and $\Delta T = (T - T_0)$, with T and T_0 being final and initial temperatures. K is a constant factor that is a function of the layer thickness t_i and Young's modulus E_i :

$$K = 4 + 6\frac{t_1}{t_2} + 4\left(\frac{t_1}{t_2}\right)^2 + \frac{E_1}{E_2}\left(\frac{t_1}{t_2}\right)^3 + \frac{E_2 t_2}{E_1 t_1}. \quad (3.11)$$

In the bimaterial case, the displacement is influenced mostly by the difference between the final and initial temperature ($T - T_0$) rather than by the vertical temperature difference ΔT_Z as in the single material case. However, in both cases, the deflection is related to a factor dependent on the length L_b of the beam and on the length of the heated up area along the beam $L_{\Delta T}$.

3.3.3 Vibration and resonance

As mentioned above, when performing electro-thermal actuation with a bimaterial structure (Fig.3.4), one of the two materials can be used as a heating resistor R where the actuating voltage is applied. In this case, the driving force is the result of the temperature gradient generated by the electrical power dissipated in R [53].

By applying an alternating voltage $\mathbf{V}_{in} = V_1 \sin \omega_1 t + V_{dc}$, the power P dissipated in heating resistor R equals to:

$$P = \frac{V_{in}^2}{R} = \frac{(V_1 \sin \omega_1 t + V_{dc})^2}{R}. \quad (3.12)$$

Expanding Eq. 3.12 and neglecting the DC terms, the AC component of the power results:

$$P_{ac} = \frac{2V_{dc}V_1}{R} \sin \omega_1 t - \frac{V_1^2}{2R} \cos 2\omega_1 t. \quad (3.13)$$

From Eq. 3.13, when applying an input voltage V_{in} formed by an AC signal $V_{ac} = V_1 \sin \omega_1 t$ with a frequency $f_{ac} = \omega_1/2\pi$ superimposed to a DC bias V_{dc} , the device will be driven into resonance if f_{ac} matches the natural frequency f_0 . If only V_{ac} is applied, resonance will be achieved using $f_{ac} = \frac{1}{2} f_0$. In both cases, resonance is due to the temperature oscillations experienced by the structure at a frequency equal to f_{ac} [4] [53] .

3.4 Piezo-electric transduction

Piezo-electric transduction can be used for inducing or detecting a mechanical strain. This section introduces the phenomena of piezo-electricity and highlights its use as a transduction technique for flexural-mode cantilevers and bridges.

3.4.1 Brief introduction

Piezo-electricity is an effect observed in some ceramic materials when a mechanical strain induces an electrical polarization (direct piezo-electric effect) [79]. The reciprocal effect (inverse piezo-electric effect) is obtained when an electric field is forced within a material thus inducing a mechanical deformation. This direct dependence between the mechanical strain and the electric field can be exploited for inducing (actuating) and/or detecting (sensing) a mechanical deformation of a structure.

Actuation can be performed and a deflection can be induced when a voltage difference is applied across a suspended structure made of a piezo-electric material. When an

alternating voltage is applied, oscillations of the electric field are generated and experienced as variations of the mechanical strain. Under these conditions, the structure vibrates and mechanical resonance can be achieved if the frequency of the input voltage matches the structure's natural frequency.

The deflection of a suspended piezo-electric structure can be sensed by detecting the voltage difference consequence of the electric field induced by the mechanical strain. In particular, if the structure is vibrating, an oscillating voltage with a frequency equal to the frequency of the mechanical oscillations can be detected across the piezo-electric material.

During the 1990s, the integration of piezo-electric thin films into MEMS devices has attracted increasing attention in the actuators area opening new possibilities for the miniaturisation of sensor devices. Piezo-electric structures have been fabricated successfully by using lead zirconium titanate (PZT), zinc oxide (ZnO) or aluminium nitride (AlN). Bimaterial devices are more common because of the possibility of reducing the size of the piezo-electric part and consequently exploiting the mechanical properties of other materials used for implementing the main structure. Bimaterial piezo-electric devices can be designed with a similar approach as electro-thermal actuators. The piezo-electric active layer is usually placed on top of the main structure. In this case, the actuating voltage is applied to the piezo-electric layer thus generating a mechanical strain that is transferred to the main structure. This mechanism has been described in detail by *DeVoe* and *Pisano* in [80].

The increasing attention focused on piezo-electric transduction has led to substantial improvements of the related fabrication techniques [32]. As discussed above, this transduction method can be used for both actuation and sensing due to the reciprocity of the piezo-electric effect [80] [81]. PZT, ZnO and AlN electrodes have been used for driving vertically different type of structures made of Si and SiO₂ [80] [81] [82] [83]. Single material piezo-electric AlN structures have been used for implementing contour-mode

resonators with rectangular [84] [85] and circular architectures that have been shown to reach resonant frequencies in the ultra high frequency (UHF) range [86] [87]. In 2004, the first devices made of a piezo-electric material on SiC structures have been reported. These devices have been fabricated by integrating AlN electrodes on top of SiC cantilevers and membranes for chemical and fluid sensing [88].

3.4.2 Displacement and induced force

As discussed above, the strain and consequently the deflection of a piezo-electric structure is proportional to the applied voltage.

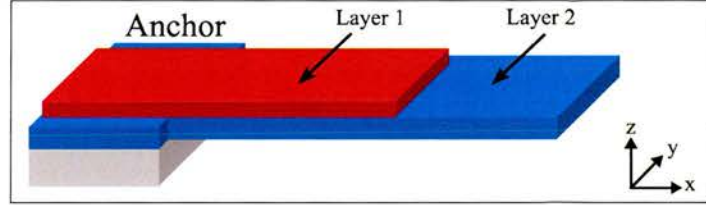


Figure 3.5: Schematic of a cantilever with a piezo-electric actuating electrode.

Fig. 3.5 shows the case of a cantilever formed by a top piezo-electric layer (subscript 1) and a bottom structural layer (subscript 2). If a voltage V_{in} is applied across the actuating electrode, the deflection in the vertical direction can be written as a function of the position along the beam x [89]:

$$z(x) = 3 \frac{d_{31} V_{in} x^2}{K_{pe} t_1^2} \quad (3.14)$$

where d_{31} is the transverse piezo-electric coefficient and K_{pe} is a constant, function of the layers thickness t_i and Young's modulus E_i :

$$K_{pe} = 4t_1 + 6t_2(t_1)^2 + 4(t_1 t_2)^2 + \frac{E_1}{E_2} (t_1^2 t_2^3) + \frac{E_2}{E_1} \frac{t_1^2}{t_2} \quad (3.15)$$

From Eq. 3.14, the induced displacement is directly proportional to the applied voltage V_{in} and to the piezo-electric coefficient d_{31} .

Due to the reciprocity of the piezo-electric effect, structures with both actuation and sensing can be implemented. Bridge structures are particularly suitable for implementing a system with an actuating and a sensing electrode.

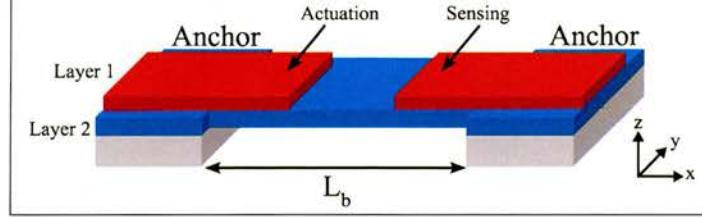


Figure 3.6: Schematic of a bridge with piezo-electric actuating and sensing electrodes.

Fig. 3.6 shows an example of a bridge with two top piezo-electric layers. The behaviour of the device can be investigated by analysing the electro-mechanical coupling between an input voltage V_{in} applied to the actuating layer and the output current I_{out} flowing through the sensing layer [80]. If the thickness of the piezo-electric film is small compared to the one of the bridge and the deflection is small compared to the dimensions of the structure, the induced force F_{pe} equals:

$$F_{pe} = \eta_1 V_{in} \quad (3.16)$$

and the output current:

$$I_{out} = \eta_2 Z \quad (3.17)$$

where η_1 and η_2 are the electro-mechanical coupling parameters and Z is the vertical displacement. The electro-mechanical coupling parameters are given in [80]:

$$\eta_1, \eta_2 \propto \frac{d_{31} E_1 t_2}{L_b}; \quad (3.18)$$

where E_1 is the Young's modulus of the top piezo-electric films and t_2 is the thickness of the bridge. Eq. 3.18 and Eq. 3.14 highlight the importance of the piezo-electric coefficient for inducing large deflections and for obtaining a large electro-mechanical coupling between input and output and therefore facilitating the electrical sensing.

Lead zirconium titanate (PZT), zinc oxide (ZnO) and aluminium nitride (AlN) are commonly used for MEMS applications because of their good piezo-electric properties. Table 3.1 summarises some of the mechanical, electrical and piezo-electric properties of these materials [32] [80].

Material	PZT	ZnO	AlN
Transverse piezo-electric coeff. d_{31} [m/V]	$-171 \cdot 10^{-12}$	$-5.1 \cdot 10^{-12}$	$-2.1 \cdot 10^{-12}$
Mass density ρ [kg/m ³]	7600	2330	3230
Young's modulus E [GPa]	63	160	278
Electrical resistivity [Ω m]	$2 \cdot 10^9$	$25 \cdot 10^9$	$> 10^{10}$

Table 3.1: Piezo-electric material properties.

3.5 Electro-static transduction

Electro-static or capacitive excitation is an electro-mechanical transduction technique that is widely used for MEMS actuators and sensors. This section introduces the basic working principle of electro-static transduction and gives an overview on the major literature works of the last two decades. As in the previous sections, the discussion will be focused on vertical flexural-mode structures.

3.5.1 Brief introduction

Electro-static transduction is based on the electro-static force that can be generated between a suspended structure made of a conductive material and a relatively close electrode. Fig. 3.7 shows the schematic of a bridge positioned on top of an electrode.

The system composed of electrode and main structure can be considered as the two parallel plates of a capacitor. As in a standard capacitor, an electro-static force can be generated by applying a voltage across the two plates. Under these conditions, the suspended structure experiences an attractive force towards the electrode.

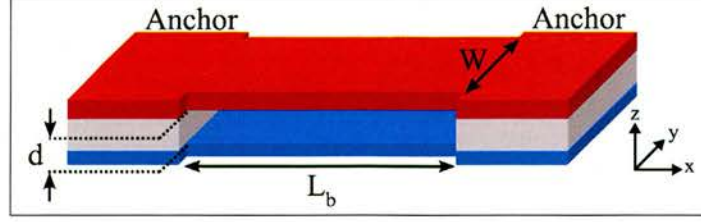


Figure 3.7: Schematic of a bridge with bottom electrode.

The reciprocal effect is also valid when the suspended structure moves towards the electrode. In this case, the distance between the two capacitor plates varies thus generating a change in the capacitance. Electro-static transduction can be employed as an actuation and sensing method for a wide range of MEMS applications.

Two of the first examples of devices employing electro-static actuation are the resonant gate transistor reported in 1967 by *Nathanson et al.* (see also Chapter 1, Section 1.1.1) and a micro-mechanical light modulator reported in 1977 by *Petersen* [5]. In the 1980s, electro-static transduction has started to attract an increasing attention because of its relative simplicity [90]. A major contribution to the developments of electro-statically actuated MEMS devices has been given by *Nguyen, Howe et al.*. In their early works, frequencies up to ~ 35 MHz have been reached with beams actuated vertically and laterally [91] [92]. More recent works have presented circular structures (wine-glass disks) actuated in the radial mode reaching ultra high frequencies (UHF) up to ~ 1.5 GHz [93].

3.5.2 Displacement and induced force

The configuration shown in Fig. 3.7, depicting a beam to be actuated in the vertical direction and suspended on an electrode, is a common and simple example used for describing the electro-static transduction mechanism. If the bridge and the electrode have the same dimensions, the capacitance C between the structure and the underlying electrode is given by:

$$C = \frac{\epsilon_0 A}{d}, \quad (3.19)$$

where ϵ_0 is the electrical permittivity in vacuum, A is the area of the capacitor ($A = W \cdot L_b$) and d is the initial distance between beam and electrode (see Fig. 3.7).

The magnitude of the electro-static force F_{es} generated by an input voltage V_{in} applied across the capacitor equals to:

$$F_{es} = \frac{1}{2} \frac{\epsilon_0 A}{z^2} V_{in}^2. \quad (3.20)$$

The magnitude of the force is proportional to the input voltage V_{in} and inversely proportional to the distance z between the two capacitor plates. The distance d between beam and electrode plays a key role in electro-statically actuated systems. In order to obtain reasonable attractive forces and induced displacements using relatively low input voltages, typical gap distances $< 1 \mu\text{m}$ have to be implemented.

When applying the input voltage, the generated electro-static force F_{es} pulls the beam towards the electrode. From Eq. 3.20, as the beam moves towards the electrode, F_{es} increases quadratically with the distance z . The electro-static force is counteracted by an opposite restoring spring force that acts to bring the beam to the initial position. At equilibrium, the electro-static force and the spring force cancel out. However, the electro-static force increases quadratically with the displacement z of the beam while the spring force increases linearly. Therefore, after a certain threshold, the electro-static force overwhelms the restoring one thus resulting in the stiction of the beam to the bottom electrode (i.e. pull-in effect). The threshold displacement and the associated threshold voltage (i.e. pull-in voltage) equal, respectively, to:

$$z_{pull-in} = \frac{2}{3}d \quad (3.21)$$

and

$$V_{pull-in} = \sqrt{\frac{8}{27} \frac{k d^3}{\epsilon_0 A}}, \quad (3.22)$$

where k is the spring constant of the structure.

3.5.3 Actuation: vibration and resonance

From Eq. 3.20, the induced force F_{es} is proportional to the square of the input voltage V_{in} . Similar to the case of the electro-thermal actuation, the displacement is proportional to the induced force and therefore to V_{in}^2 . Vibrations can be induced to the structure if an alternating voltage is applied between the beam and the electrode. For the case of an input voltage formed by an AC signal superimposed to a DC bias, $V_{in} = V_1 \sin \omega_1 t + V_{dc}$, the force F_{es} results:

$$F_{es} \propto V_{in}^2 = (V_{dc} + V_1 \sin \omega_1 t)^2 = V_{dc} V_1 \sin \omega_1 t - \frac{1}{2} V_1^2 \cos 2\omega_1 t + V_{dc}^2. \quad (3.23)$$

If an AC voltage is superimposed to a DC bias, the device is driven into resonance through the first term in Eq. 3.23 when the input frequency $f_{ac} = \omega_1/2\pi$ matches the natural frequency f_0 of the structure. If only an AC voltage is applied, resonance is achieved with the contribution of the second term in Eq. 3.23 when f_{ac} equals $\frac{1}{2} f_0$.

3.5.4 Electro-static mixing

An interesting application for electro-static resonators has been developed by *Nguyen et al.* for RF devices. The quadratic dependence between the force and the voltage has been exploited to implement a frequency mixing function [92]. The mixing function is performed by applying two alternating voltages $V_{RF} = V_{RF} \sin \omega_{RF} t$ and $V_{LO} = V_{LO} \sin \omega_{LO} t + V_{dc}$ to a bridge resonator and to a bottom actuating electrode, respectively (configuration similar to Fig. 3.7). Under these conditions, the driving force results:

$$F_{mix} \propto -\cos(\omega_{RF} - \omega_{LO})t. \quad (3.24)$$

In this way, the device is driven into resonance if the difference between the two frequencies of V_{RF} and V_{LO} matches the natural resonant frequency f_0 of the bridge. The device acts as a mixer-filter providing a mixing function for frequencies with their

difference equal to f_0 and a filtering function for frequencies not matching the beam resonance. The same principle has been employed for implementing a CMOS-MEMS resonant mixer-filter using lateral resonators and contour-mode wine-glass disk resonators [94] [95] [96].

3.6 Conclusions

The most common architectures described in the literature for vertical actuators, sensors and resonators have been discussed. The analytical formulas for the fundamental resonant frequency of single-clamped beams (cantilevers), double-clamped beams (bridges) and circular membranes (disks) have been presented. The influence of the materials' elastic moduli, mass density and structures' dimensions on the resonant frequency shows the importance of the materials choice and structures design.

In order to provide a theoretical framework for the work undertaken in this thesis, the basic working principles of electro-thermal, piezo-electric and electro-static transductions have been analysed and summarised.

Among the transduction techniques described in this chapter, electro-static actuation is used widely for a variety of MEMS devices. The direct dependence between electro-static force and actuating voltage allows a precise control of the mechanical deflection. Another major advantage is that capacitive driving can be used for performing both actuation and sensing functions. In addition, because of the absence of electric current flow between the main actuated structure and the actuating electrode, no power is dissipated leading to a very low power consumption in the entire device. However, major drawbacks limit the performance of electro-statically actuated MEMS devices. The manufacturing process can be relatively complicated due to the critical fabrication of small gaps (generally < 100 nm) essential to have a considerable driving force and a low motional resistance. Furthermore, complicated designs are required in order to solve problems related to pull-in instabilities, high actuation voltages and impedance

mismatch between the device and the 50 Ω input/output network.

Electro-thermal excitation is a technique that could be optimised using bimaterial structures. From a fabrication point of view, the process can be simpler compared to the one used for electro-statically actuated devices because critical size gaps are not required. The actuating resistor used for inducing the mechanical deflection can be conveniently designed for accommodating the requirements of the 50 Ω input/output network. In general, electro-thermal actuators exhibit large deflections induced with low actuation voltages (ranging between 1 - 6 V) so that the power consumption can be maintained at relatively low values [97].

The main constraint of electro-thermally actuated devices is the operating frequency that is limited by the heating and cooling times dependent on the structures' geometry and materials' thermal conductivity [1] [98] [99]. In addition, the electro-thermal effect cannot be used as a sensing technique hence requiring other transduction methods when the electrical detection of the mechanical displacement is demanded.

Piezo-electric transduction has started to attract interest since the improvements in the integration of piezo-electric thin films into MEMS. This transduction method can be used for both actuation and sensing due to the reciprocity of the piezo-electric effect. The actuation is carried out with pure AC voltages without the need of any DC polarisation and the motional resistance at high frequency can be kept relatively low [85] [100]. In addition, the fabrication process of piezo-electric driven actuators and sensors do not require critical size gaps.

It is important to point out that the function of frequency mixing using mechanical resonators is advantageous when aiming to RF applications. The mixing function can be carried out with MEMS devices by exploiting the non-linearity between actuation voltage and induced force. Electro-static transduction has been used for performing frequency mixing. Nevertheless, electro-thermal transduction shows the same quadratic proportionality between actuating voltage and force thus allowing in principle

the electro-mechanical mixing of two input frequencies. One of the aims of this thesis is to demonstrate the ability of performing electro-thermal mixing in order to consider the employment of electro-thermal actuators for wireless and RF applications. Furthermore, piezo-electric transduction will be investigated as a sensing technique that could permit the implementation of an electro-thermally actuated micro-mechanical mixer with piezo-electric sensing.

Chapter 4

Design and fabrication of SiC MEMS

4.1 Introduction

In this chapter, the design and fabrication of SiC MEMS structures are presented.

In the first part of the chapter, the fabrication process flow developed for manufacturing single material SiC single and double clamped beams (i.e. cantilevers and bridges) is described.

The second part of the chapter is dedicated to the integration of metal electrodes onto SiC structures in order to provide an electrical connection to the devices for performing electro-mechanical transduction. The fabrication method developed for single material SiC MEMS has been extended for the integration of metal patterns on top of the SiC. Bimaterial devices formed of Al electrodes placed on top of SiC beams have been fabricated. In addition, a process for the manufacturing of piezo-electric active layers has been developed and integrated into the SiC beams process flow.

In the last part of the chapter, attention is focused on the fabrication of circular SiC

membranes with a circular hole patterned in the centre (i.e. rings). The process flow developed for the manufacturing of beams has been adapted and characterised for the fabrication of single material SiC and bimaterial SiC rings with Al electrodes.

4.2 General observation on the design and fabrication

The patterning of the structures has been performed using standard UV photolithographic processes and UV mask aligners. Initial test designs have been made on 4-inch masks with the patterns confined within 1 cm^2 fields. Square chips having same dimensions as the mask pitch have been diced, mounted on carrier wafers and patterned photolithographically. However, this technique could be employed only when aligning one or two layers due to the limitation in the alignment precision of the tool used ($\sim \pm 3\text{ }\mu\text{m}$). Once the design has been finalised and the critical structural dimensions have been investigated, 5-inch masks have been designed and 4-inch wafers have been used. In this way, designs needing more than two layers to be aligned have been patterned using a tool with an alignment precision of $\sim \pm 0.5\text{ }\mu\text{m}$. The tools used for the fabrication have been listed in Appendix B.

4.3 SiC beams

In this section, the process flow developed for the fabrication of the SiC micro-mechanical beams studied in this thesis is described.

As discussed in Chapter 2, Section 2.3, 3C-SiC layers can be grown on top of Si bulk substrates or on multi-layer substrates formed by a top layer of poly-Si, SiO_2 or Si_3N_4 , previously grown on Si substrates. Bulk substrates are particularly suitable for manufacturing suspended SiC MEMS devices using front-side bulk micromachining techniques while multi-layer substrates can be used for surface micromachining (see Chapter 2, Section 2.5). The release of SiC structures can be performed with various wet

and dry etching techniques that are well characterised in literature.

The manufacturing of SiC structures has been performed using Si as a sacrificial material and the fabrication process has been developed for:

- i. single and poly-crystalline 3C-SiC layers grown on bulk Si substrates,
- ii. poly-crystalline 3C-SiC layers grown on multi-layer poly-Si/SiO₂/Si substrates.

Fig. 4.1 shows a schematic of the process flow used for the fabrication of the SiC structures. The left and the right sides depict the fabrication with bulk Si (i.) and with multi-layer substrates (ii.), respectively. The process has been divided in three main parts that are discussed in detail in the next sections:

1. Growth (Fig. 4.1(a)),
2. Mask, etch and release(Fig. 4.1(b)(c)(d)),
3. Final release and mask removal (Fig. 4.1(e)(f)).

4.3.1 SiC growth

The SiC layers have been grown with a thickness of $\sim 2 \mu\text{m}$ on top of the two different type of substrates: bulk Si substrate (i. in Fig. 4.1(a) left side) and multi-layer substrate (ii. (Fig. 4.1(a) right side)).

Linköping University (Sweden) and *novaSiC* have provided single and poly-crystalline SiC films grown on the bulk Si substrates. *Case Western Reserve University* (Ohio, U.S.A.) has provided poly-crystalline SiC layers grown on the multi-layer substrates made of a $4 \mu\text{m}$ thick LPCVD poly-Si layer deposited on thermally oxidised bulk Si.

4.3.2 SiC etching and choice of masking material

As discussed in Chapter 2, Section 2.4, SiC films can be patterned using dry or photo-assisted wet etching techniques. However, a dry etching process is more suitable for MEMS applications due to the need of relatively vertical side walls. In addition, induc-

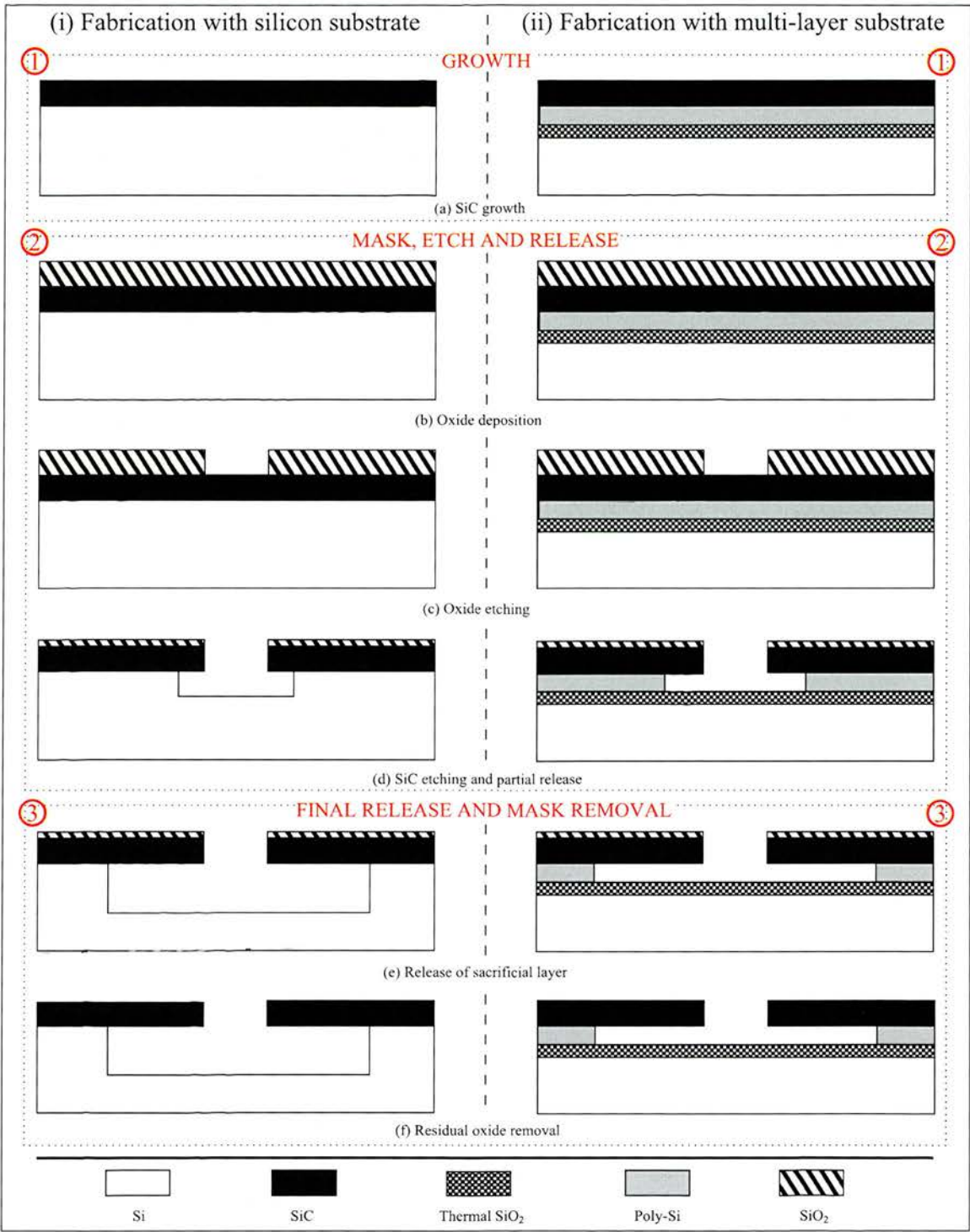


Figure 4.1: Fabrication process flow of SiC beams.

tively coupled plasma - reactive ion etching (ICP-RIE) is preferable for SiC because of the much faster etch rate compared to reactive ion etching (RIE).

A dry etching ICP-RIE technique with a gas mixture of SF_6 and O_2 , similar to the one presented in Chapter 2, Section 2.4 and described in detail in [45], has been used. However, the process has been modified slightly for adapting to the tool used. The flow-rate of SF_6 and O_2 has been set at 55 and 10 sccm, respectively, and the chamber pressure fixed at 7 mT. The platen power and the coil power have been fixed at 50 and 900 W, respectively. Due to the relatively high power and low pressure used, a standard photoresist is not durable enough to be employed as a mask. Therefore, plasma-enhanced-chemical-vapour-deposited (PECVD) SiO_2 has been chosen as masking material because of its feasibility in the deposition and etching on a wide range of substrates.

Some initial experiments have been performed on SiO_2 and SiC in order to have a general characterisation of the etching selectivity between the two materials. With the process conditions considered, the etching rate of SiO_2 and SiC has been shown to be ~ 180 and 210 nm/min, respectively, resulting in a selectivity of $\sim 1:1.2$. Considering that $2\text{ }\mu\text{m}$ of SiC has to be etched, the thickness of the PECVD SiO_2 has been chosen to be between 2.5 and $3\text{ }\mu\text{m}$ (Fig. 4.1(b)).

After the SiO_2 deposition, the beam shapes have been photolithographically patterned on the thick oxide mask. Then, the exposed material has been removed with a CF_4/H_2 RIE plasma hence creating rectangular windows into the SiC (Fig. 4.1(c)). At this point, the SiC has been etched with the ICP-RIE tool (Fig. 4.1(d)).

In addition to the SiC etching, the advantage of this process is that the exposed Si is removed by the SF_6 gas present in the plasma. A sideways release rate of about $2\text{ }\mu\text{m}/\text{min}$ has been obtained thus giving a selectivity of $\sim 12:1$ to the SiO_2 mask [51]. Under these conditions, a $3\text{ }\mu\text{m}$ thick oxide layer lasts enough time to etch $2\text{ }\mu\text{m}$ of SiC and to remove $12\text{ }\mu\text{m}$ of Si sacrificial layer.

4.3.3 SiC release

As discussed, the Si sacrificial layer can be released with the same gas mixture used for the SiC etching. However, due to the limited etching selectivity between the oxide mask and the SiC, when the fabrication process requires undercut lengths $> 12\text{ }\mu\text{m}$, the release has to be completed with a further process step. In the described process flow, the sacrificial layer has not been patterned to introduce an etch-stop. Therefore, in order to avoid a large undercut at the anchors of the beams, a process that can control the release rate has been developed. In this case, a dry technique is preferred rather than a wet one. Moreover, issues related to the stiction between the sacrificial and structural layers are avoided if dry release approaches are employed.

A release process using XeF_2 in its vapour state has been developed because of its advantages over ICP-RIE with SF_6/O_2 gases [46]. During this step, no plasma is used so that the SiC is not attacked. This chemical dry etch technique allows a time-controlled release of the structures (Fig. 4.1(e)). Typical release rates in the range between 3 and 10 $\mu\text{m}/\text{min}$ have been obtained depending on the aperture size of the exposed sacrificial layer and on the etching conditions (i.e. chamber pressure and gas flow rate) [46].

Once the release has been completed, the residues of masking oxide left on the SiC surface have been removed in a CF_4/H_2 plasma (Fig. 4.1(f)).

Fig. 4.2 shows two scanning electron micrograph of SiC bridges fabricated on a bulk Si substrate (Fig. 4.2(a)) and cantilevers fabricated on a multi-layer substrate (Fig. 4.2(b)).

It is worth pointing out that in the process flow developed for the fabrication of the SiC beams, the dimensions of the structures are defined during the design process. However, the lack of the patterning of the sacrificial layer introduces the need of controlling the release rate in order to minimise the undercut at the anchors. In fact, a large over-release causes unwanted changes to the designed dimensions and in the case of beams, the final structure could become longer than the designed one. These

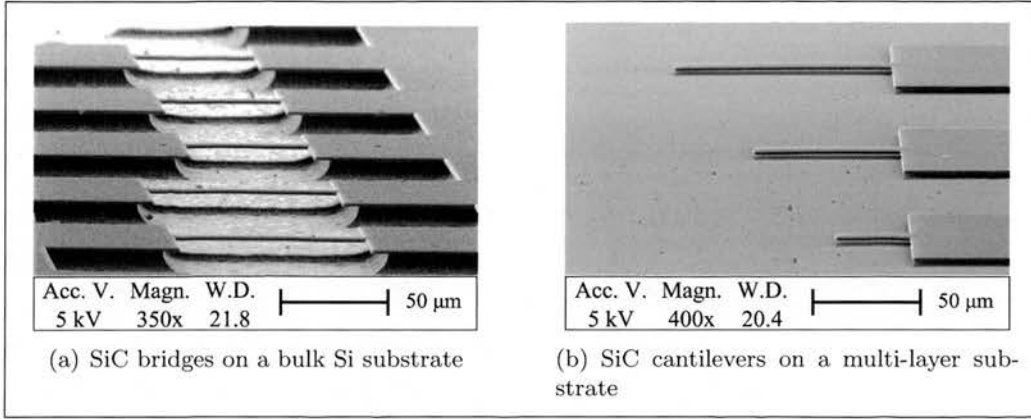


Figure 4.2: Scanning electron micrograph of SiC beams.

dimensional variations lead to discrepancies between the actual resonant frequency and the simulated one thus hindering the comparison between the simulated model and the fabricated structure. The XeF_2 dry release has shown to be particularly suitable for controlling the release rate by operating on chamber pressure and gas flow rate.

4.4 SiC beams with Al electrodes

In the previous section, the fabrication of SiC suspended structures has been described. The integration of Al electrodes can be implemented by adding the necessary steps straight after the SiC growth.

Fig. 4.3 shows the schematic of the process flow for the fabrication of the Al/SiC beams. After the SiC growth on the substrate, a thin passivation layer of SiO_2 (~ 100 nm) has been grown thermally in order to insulate electrically the SiC from the Al. Then, a 500 nm thick layer of Al has been sputtered on top of the oxide (Fig. 4.3(a)). The electrodes have been patterned photolithographically and etched with an RIE technique in a SiCl_4/Ar plasma (Fig. 4.3(b)). During this step, the exposed Al and the thin oxide are removed together. At this point, the fabrication steps described in Section 4.3 have been performed. The masking oxide has been deposited and patterned, the SiC has been etched and released (Fig. 4.3(c)). A schematic of the top view of the final structure

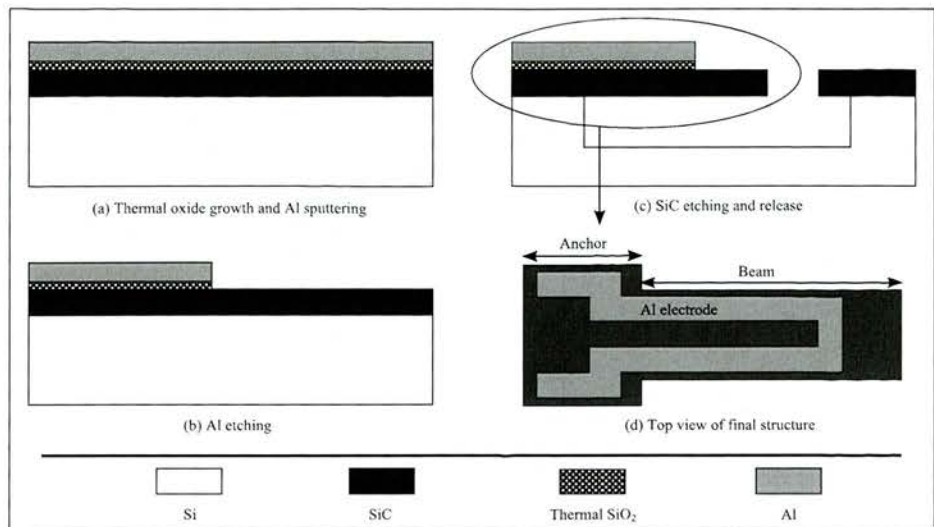


Figure 4.3: Simplified fabrication process flow of Al/SiC beams.

is shown in Fig. 4.3(d). Fig. 4.4 shows two of the fabricated SiC beams with top Al electrodes. It is worth noting that the overall structure Al/SiC can be considered as a bimaterial beam.

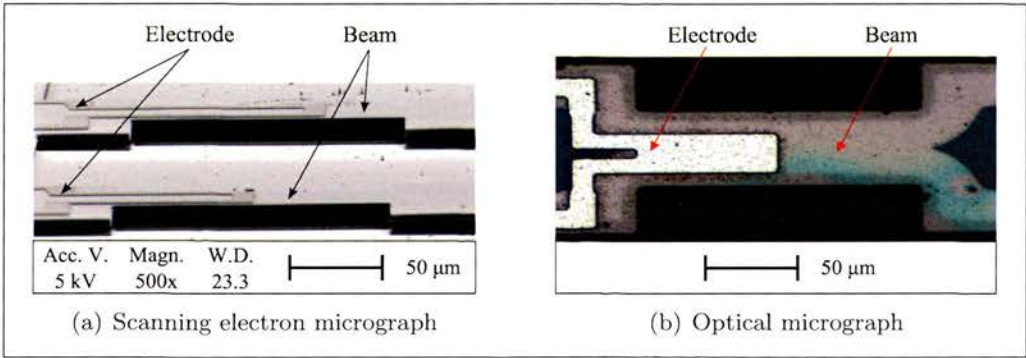


Figure 4.4: Fabricated bimaterial SiC bridges 150 μm long with Al electrodes on top.

4.5 SiC beams with piezo-electric active layers

In this section, the fabrication process of SiC beams with piezo-electric active layers placed on top is presented. The process flow can be divided in two parts; the first one for the patterning of the electrode and the second one for the patterning of the beam. The implementation of a piezo-electric layer requires a more elaborate process

compared to a resistive Al electrode. The formation of the beam is the same as the one presented for single material SiC beams in Section 4.3.

4.5.1 Fabrication of piezo-electric active layers

In order to improve the transduction efficiency, PZT has been chosen because of its high piezo-electric coefficient (see Chapter 3, Section 3.4). When performing piezo-electric actuation, a voltage across the piezo-electric material has to be applied thus bottom and top contacts to the PZT have to be implemented. Ohmic contacts to the PZT can be obtained by using conductive layers of Pt.

Fig. 4.5 shows the schematic process flow for the fabrication of the piezo-electric active layers.

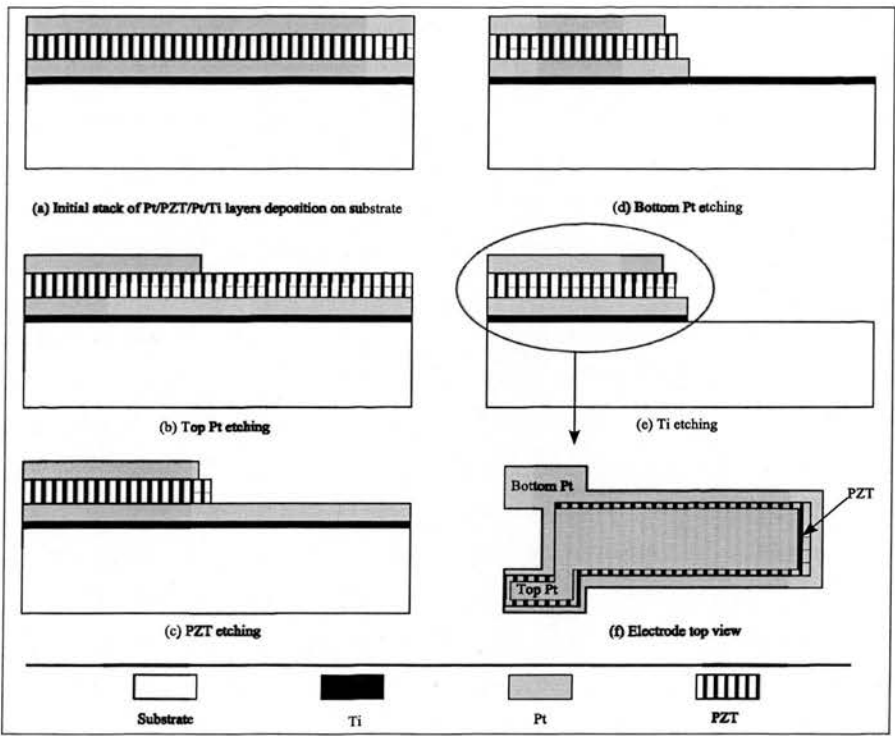


Figure 4.5: Fabrication process flow of Pt/PZT/Pt electrodes.

The initial stack of materials made of Ti/Pt/PZT/Pt with thickness of 10, 100, 500 and 100 nm, respectively, has been provided by *Inostek inc.* (Fig. 4.5(a)). The PZT is deposited with a sol-gel process using a 10 wt % lead (Pb) excess 52/48 PZT solution [101]. The very thin layer of Ti has been used as adhesion layer between the bottom Pt and the substrate while the two Pt layers as bottom and top contacts to the PZT. The electrode stack has been deposited on a Si substrate. The top Pt has been patterned photolithographically for defining the top metal contact to the PZT. The Pt has been etched with an Ar ion beam tool using an acceleration and a beam voltage of 250 and 500 V, respectively, resulting in an etching rate of ~ 7 nm/min (Fig. 4.5(b)).

After the etching of the top Pt, the PZT layer has been patterned photolithographically and wet etched (Fig. 4.5(c)) in a solution made of

$$BHF : HCl : NH_4Cl : H_2O = 1 : 2 : 4 : 40. \quad (4.1)$$

The buffered HF (BHF) has been made by diluting NH_4F into HF with a 10 : 1 ratio. Under these conditions, the PZT is etched at ~ 13 nm/s while the Pt layers are not attacked. However, during the wet etching step, redeposition of PZT residuals on the bottom layer of Pt occurs so that a further rinsing in $HNO_3 : H_2O = 2 : 1$ for 15 seconds is needed to remove the unwanted particles on the surface [102]. The details of the acid concentrations used for the wet etching of PZT are given in Appendix B.

Once the PZT has been etched, the bottom metal contact has been defined by photolithography and etched with the same process as the one for the top Pt contact (Fig. 4.5(d)). Finally, the bottom Ti is etched with a $SiCl_4/Ar$ RIE plasma for 1 minute (Fig. 4.5(e)). In this last part of the process, photolithography has not been required because the photoresist used for masking the bottom Pt has been used for masking the Ti layer. A schematic of the top view of the final electrode structure is shown in Fig. 4.5(f). Fig. 4.6 shows a scanning electron micrograph of one of the fabricated piezo-electric layers.

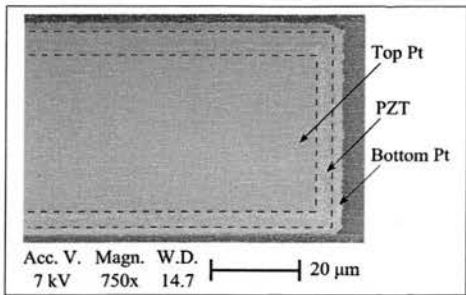


Figure 4.6: Scanning electron micrograph of a Pt/PZT/Pt electrode.

4.5.2 Integration of piezo-electric active layers into SiC beams actuators

For the fabrication of the SiC beams with piezo-electric layers on top, 4-inch Si wafers have been used as main substrate. Similar to the Al/SiC process presented in Section 4.4, the integration of the electrodes on the SiC beams can be performed by adding the deposition and patterning of the Pt/PZT/Pt/Ti stack just after the SiC growth.

Fig. 4.7 shows the process flow for the fabrication of SiC beams with piezo-electric active layers.

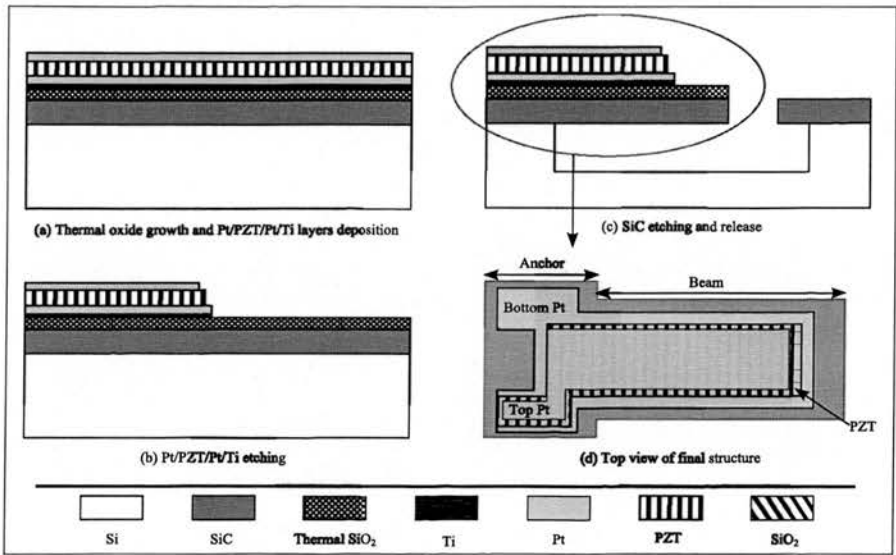


Figure 4.7: Simplified fabrication process flow of Pt/PZT/Pt/SiC beams.

A $2\text{ }\mu\text{m}$ thick SiC epilayer has been grown on top of the Si and then thermal SiO_2 has been grown as a passivation layer on top of the SiC. Afterwards, Ti, Pt, PZT and Pt have been deposited by *Inostek inc.* (Fig. 4.7(a)). Then, the piezo-electric stack electrode has been patterned as described in the previous section (Fig. 4.7(b)). Afterwards, the SiC beam has been etched and released as described in Section 4.3 (Fig. 4.7(c)). A schematic of the top view of the final structure is shown in Fig. 4.7(d). Fig. 4.8 shows two scanning electron micrographs (top and side view) of one of the fabricated SiC beams with a piezo-electric active layer placed on top.

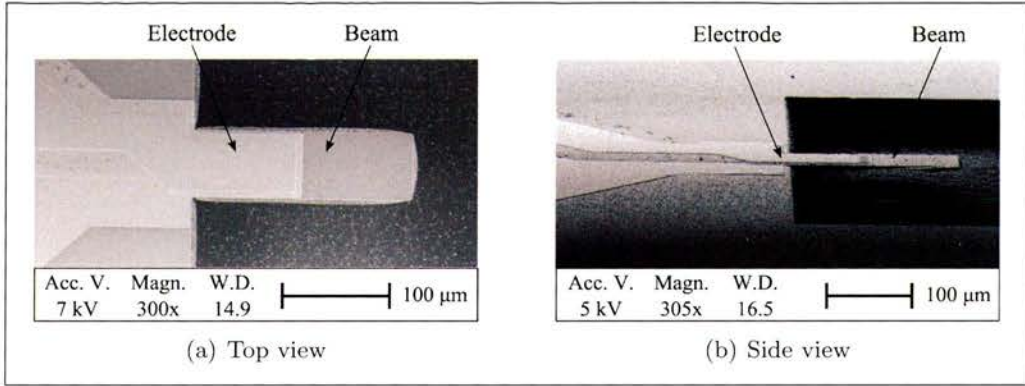


Figure 4.8: Scanning electron micrograph of a SiC beam with a piezo-electric layer on top.

4.6 SiC rings with Al electrodes

Circular membranes with a circular hole patterned in the centre (i.e. rings) have been fabricated using the same process flow described for the beam structures in Section 4.3. Al electrodes can be included in the devices as discussed for bimaterial Al/SiC beams in Section 4.4.

Although the process flow for the SiC rings is the same as for the SiC beams, the final dimension of the suspended part of the ring structure is defined during the release process. As a matter of fact, only the radius of the circular hole is defined during the design while the radius of the overall structure is defined during the release process.

In the case of beams, the length and width are fixed during the design process and only the undercut at the anchor is controlled during the release step. For both types of structures, the thickness of the final device is defined during the SiC growth process.

For the fabrication of the rings, a $\sim 2 \mu\text{m}$ thick single crystalline SiC layer grown on bulk Si substrates has been used. After growing the passivation layer of SiO_2 , a 500 nm thick layer of Al has been deposited and the electrodes etched. Then, holes with different radius have been patterned photolithographically on the PECVD masking oxide and the exposed material removed with RIE plasma. The holes in the SiC have been etched with the ICP-RIE process and the Si has been released with XeF_2 dry etching (see Section 4.3). The circular shape of the patterned central hole is transferred to the sacrificial layer during the release process and a ring structure is obtained. Consequently, the final radius of the ring is defined during the time dependent release step and is determined by the released area under the SiC layer. The transparency of the SiC layer used has allowed measuring the final radius of the rings using an optical microscope. The release rate of the rings strictly depends on the etching conditions and on the dimensions of the central hole.

Fig. 4.9 shows the schematic of the Al/SiC ring resonators. Structures with a hole radius h of 2, 6, 15 μm and ring radius R in the range between 15 and 200 μm have been fabricated.

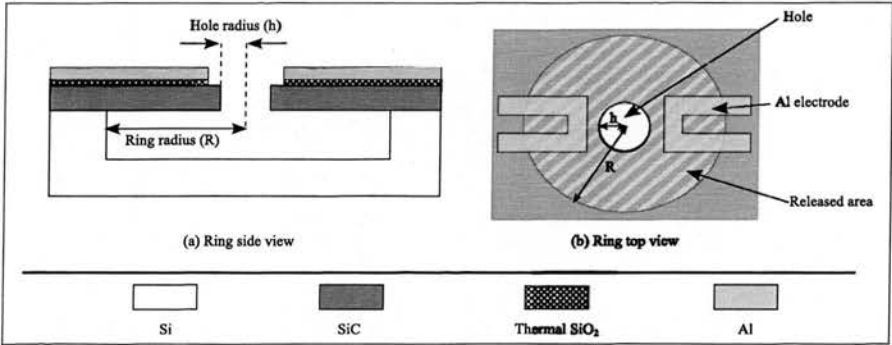


Figure 4.9: Schematic of the fabricated Al/SiC ring resonators.

Fig. 4.10 shows two of the fabricated rings having double and inter-digitated (IDT)

electrode configurations.

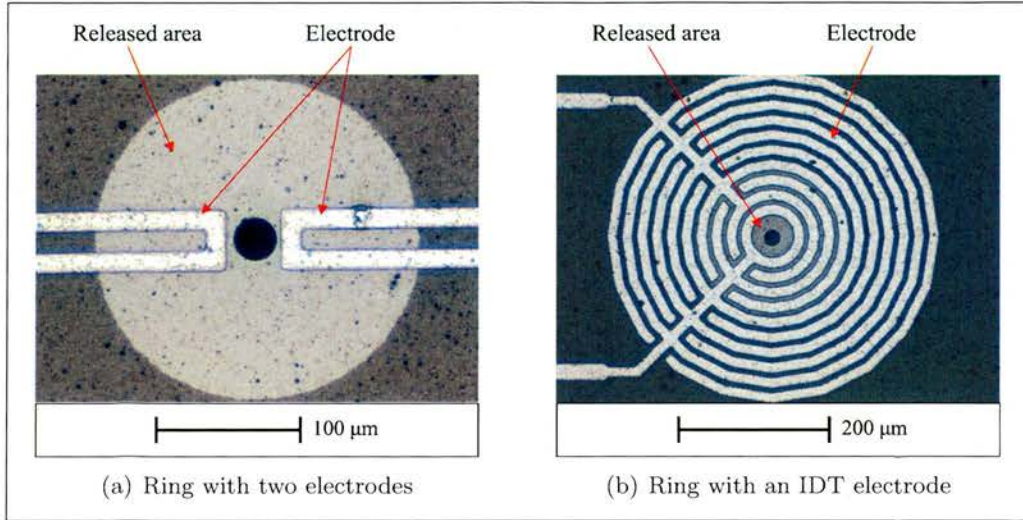


Figure 4.10: Optical micrograph of two of the fabricated bimaterial Al/SiC ring resonators.

4.6.1 Release characterisation

It is important to notice that in the fabrication of the SiC rings, the XeF_2 dry release is a crucial step because the final dimensions of the structures are defined during the removal of the sacrificial layer. In order to help the repeatability of the process, the release rate has been characterised in the radial direction as a function of time and for different etching conditions and aperture sizes (i.e. hole radius). In addition, in order to investigate the etching mechanism, the area release rate has been calculated from the radial release. As mentioned before, the transparency of the SiC used has allowed measuring the radius of the released area using an optical microscope.

4.6.1.1 Radial release length

Fig. 4.11 shows the release length in the radial direction as a function of the etching time t for $h = 2, 6, 15 \mu\text{m}$ and measured from the edge of the hole. Chamber pressures of 1 and 2 Torr with a XeF_2 flow rate of 100 sccm have been used.

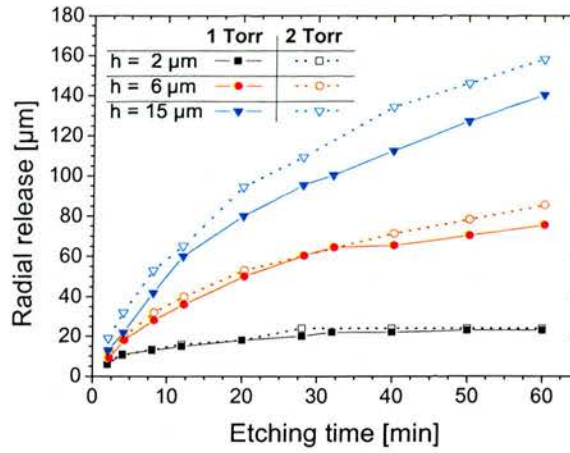


Figure 4.11: Release length in the radial direction as a function of process time for holes with radius $h = 2, 6, 15 \mu\text{m}$ at chamber pressure of 1 and 2 Torr and flow rate = 100 sccm.

The release length increases when the hole radius is increased showing that the aperture size influences the amount of material that can be removed. As the hole's size increases, the access of the gas species into the aperture and the removal of the etching products are enhanced. Therefore, after the same amount of etching time, wider structures are obtained for larger holes.

For $h = 2 \mu\text{m}$, as the etching time increases, the radial release length increases until $t \approx 30 \text{ min}$ to saturate at a value of $20 \mu\text{m}$. In the case of $h = 6$ and $15 \mu\text{m}$, the radial release length has not been observed to saturate and to increase to maximum values of ~ 160 and $80 \mu\text{m}$ for $t = 60 \text{ min}$, respectively. As the release time increases, the saturation of the radial release length occurs probably because more material is exposed so that more gas species are needed for the etching. In the particular case of $h = 2 \mu\text{m}$, the access of the gas species is limited due to the relatively small size of the hole. Therefore, after a certain amount of time, the concentration of exposed material becomes higher than the gas species available for etching and therefore no more material can be removed.

The increase in the chamber pressure from 1 to 2 Torr does not affect the release length for hole radius of $2 \mu\text{m}$. However, when the pressure is increased, a relatively small

increase and a larger one is observed for hole radius of 6 and 15 μm , respectively. This behaviour is probably due to the fact that by increasing the pressure, the mean free path of the gas species decreases thus leading to a higher amount of species able to access the aperture. As a consequence, the probability of chemical reactions with the Si is enhanced and the radial release increases. However, it is believed that the mean free path of the species is not reduced enough to enhance the access through the aperture with $h = 2 \mu\text{m}$ so that the increase in the release length is not observed for this aperture size.

4.6.1.2 Area release rate

A further investigation on the release mechanism of circular membranes has been carried out by calculating the area release rate from the measured release in the radial direction. Fig. 4.12 shows the area release rate as a function of the etching time at chamber pressures of 1 and 2 Torr and for different hole radii.

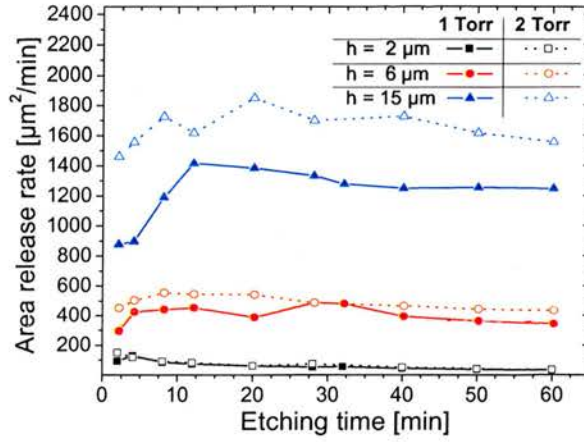


Figure 4.12: Area release rate as a function of etching time for holes with radius $h = 2, 6, 15 \mu\text{m}$ at chamber pressure of 1 and 2 Torr and flow rate = 100 sccm.

A higher area release rate is evident when the hole size h is increased. The larger area release rate observed at 2 Torr for $h = 15 \mu\text{m}$ suggests the dominance of the aperture effects in the etching mechanism. In addition, the area release rate is found to increase

initially and then to decrease after some time. This effect is probably due to the fact that at the beginning, the amount of gas species able to enter the aperture is higher than the actual amount needed to remove Si. As the Si is etched and removed, a larger amount of it is exposed and consequently a larger area is released resulting in an increase in the area release rate. As time goes on, the concentration of exposed Si becomes higher than the concentration of gas species available for etching, hence the area release rate starts to decrease due to the depletion of the gas species.

The characterisation of the release length in the radial direction and the area release rate for different hole's sizes has allowed the repeatability of the SiC rings fabrication. The XeF_2 dry etching technique has been found to be particularly suitable for this process permitting to control the release rate so that the final dimensions of the structures have been defined with a relatively good precision.

4.7 Conclusions

In this chapter, the process flow developed for the manufacturing of surface micromachined SiC MEMS devices has been described. SiC layers grown on bulk Si substrates and on multi-layer poly-Si/SiO₂/Si substrates have been used. The SiC has been patterned using an ICP-RIE process with a gas mixture composed of SF₆ and O₂. The removal of the Si sacrificial layer has been performed partially during the SiC etching and then finalised with a XeF_2 dry vapour release technique.

Initially, the process has been characterised for the formation of single material SiC single and double clamped beam devices (i.e. cantilevers and bridges). Then, metal electrodes have been integrated in order to allow the possibility of performing electro-mechanical transduction for the actuation of the devices. Al electrodes and PZT layers have been successfully integrated onto the SiC beams.

The sacrificial layer has not been patterned thus making the process flow relatively

simple. When the release step is performed, the lack of patterned sacrificial layers could lead to large undercuts at the anchors resulting in variations on the designed dimensions of the structures. However, the dry release technique used has been shown to be particularly suitable for controlling the etching rate so that the issues related to the absence of an etch-stop have been avoided. The over-release at the anchors has been limited by calculating the time needed for the release of the structures.

The same surface micromachining technique used for the fabrication of SiC beams has been utilised for manufacturing circular membranes with a hole patterned in the middle (i.e. rings). The hole has been used to create an access to the sacrificial layer so that it could be removed by the releasing gas. The circular shape of the hole has been transferred to the sacrificial layer and a final ring-shaped structure has been obtained.

Despite the similarities between the fabrication process of beams and rings, the width and length of the beams are defined during the design process, while in the case of rings, the final radius is defined during the release process. In order to ensure the control of the rings dimensions and reproducibility of the process, the release mechanism of the rings has been analysed by investigating the release length in the radial direction and the area release rate as a function of the central hole's size and chamber pressure. The release mechanism has been shown to be dominated by aperture effects. In addition, as the released area becomes larger, the area release rate decreases due to the depletion of the gas species. The dependence of the release process on the hole's size and on the etching conditions has allowed the control of the release rate and consequently the definition of the final ring dimensions with a relatively good precision.

The fabricated devices will be analysed and tested in the next chapters. In particular, the structures' mechanical and electro-mechanical behaviours will be investigated.

Chapter 5

Characterisation of SiC

5.1 Introduction

In general, structural layers with good crystal quality are required for fabricating robust and reliable MEMS devices. In addition, materials with a high Young's modulus are preferred when aiming to high frequency applications.

In the previous chapter, the process flow developed for the fabrication of SiC MEMS structures has been presented. SiC layers grown on Si bulk substrates or on poly-Si/SiO₂/Si multi-layer substrates have been used for fabricating beams and rings. As discussed in Chapter 2, the crystal orientation and the quality of the SiC layers depend on the growth conditions and on the crystal orientation of the Si layers used underneath.

For the fabrication, some of the SiC layers have been provided by the Department of Physics, Chemistry and Biology of *Linköping University* (Sweden). The two SiC layers examined have been grown on bulk Si substrates by hot-wall LPCVD at 400 mbar - 1280 °C and at 300 mbar - 1350 °C, respectively, using silane SiH₄ and propane C₃H₈ as precursor gases [36]. In this chapter, the characterisation of the polytype, crystal orientation, quality and Young's modulus of the SiC layers is presented.

In the first part, Raman spectroscopy has been utilised for investigating the quality

and the polytype of the SiC films while X-ray diffraction (XRD) has been used for characterising the crystal orientation. The basic principles behind the two techniques will be introduced and the measurements performed on the SiC layers will be discussed.

In the second part, a measurement setup for actuating mechanically MEMS structures and inspecting the resonant frequency is described. The structures fabricated with the process flow presented in Chapter 4 have been excited mechanically in order to explore the possibility of utilising them as MEMS resonators. The measurements performed on single material SiC cantilevers are presented. In addition, the Young's modulus of the SiC layers has been calculated from the resonant frequency of cantilevers having different lengths.

5.2 Raman spectroscopy characterisation

Raman spectroscopy is used as a non-destructive technique to investigate the structure of materials. A detailed description of the theory behind Raman spectroscopy is given by *Banwell* [103]. In this section, the mechanism of Raman scattering is discussed briefly. Then, the results obtained from the measurements performed on the SiC layers grown in *Linköping University* are presented.

5.2.1 Introduction to Raman spectroscopy

Raman spectroscopy is based on the interaction mechanism between an electro-magnetic (EM) wave and a molecule.

When an EM wave of frequency ν_0 interacts with a material, the electron cloud of the molecules oscillate at the same frequency ν_0 of the incident wave creating a periodic charge separation in the molecules. This effect is experienced as an electric dipole moment induced within the molecules. The oscillating dipole emits radiations at ν_0 that are referred as elastic or Rayleigh scattering. In addition, the molecule experiences

internal vibrational and rotational oscillations that superimpose to the effect of the oscillating dipole. In the case of a vibrational oscillation of frequency ν_{vib} , the emitted radiation has frequency components equal to ν_0 and $\nu_0 \pm \nu_{vib}$. The radiations emitted due to the internal motion of the molecule are referred as inelastic or Raman scattering and are observable as a shift of the incident frequency ν_0 towards lower or higher values (i.e. Raman shift). The Raman emission can be considered as a fingerprint of the excited molecule and gives information about the vibrational state of the molecule which relates to the nature of the internal bonds and to the type of molecular structure. Raman spectroscopy can be explained with the following interpretation. The incident wave can be represented as a stream of photons and the molecular vibration modes can be represented as vibrational quantum states. If the Planck's constant is defined as h , the energy E_0 of each photon is equal to $h\nu_0$ and the energy difference ΔE_{vib} between two vibrational states is equal to $h\nu_{vib}$.

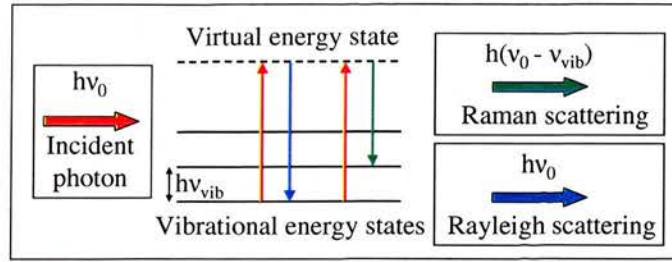


Figure 5.1: Schematic representation of Raman scattering emission.

Fig. 5.1 shows a schematic representation of the interaction mechanism between a photon and a molecule. The incident photon induces an oscillating dipole moment that is experienced by the molecule as a virtual energy state (red arrow in Fig. 5.1). In the case of an elastic collision between the photon and the molecule, the energy of the scattered photon remains unchanged, the molecule returns to its initial vibrational state (blue arrow in Fig. 5.1) and Rayleigh scattering is observed. However, in case of an inelastic collision, energy is exchanged between the photon and the molecule that consequently enters in a vibrational state different from the initial one (green arrow in

Fig. 5.1). The resulting loss of energy is observed as a Raman radiation.

When performing Raman scattering in crystals, the incident EM wave excites the lattice vibrational modes referred to as longitudinal (LO) and transverse (TO) optical phonon modes depending on whether they are excited in a direction parallel or perpendicular to the incident EM wave, respectively. The lattice vibrational modes are related closely to the crystal arrangement for every crystal [104]. In the case of SiC, the longitudinal scattering is “allowed” while the transverse one is “forbidden” [105]. The polytype and the quality of a crystal lattice can be investigated by observing the intensity and the relative position of the TO and LO peaks in the Raman spectra. In addition, Raman spectroscopy can be used to determine the residual stress in thin films by observing the shift of the LO and TO peaks.

5.2.2 Raman spectroscopy measurements results

Fig. 5.2 shows the Raman spectra obtained for the SiC layers grown on bulk Si substrates. Fig. 5.2(a) and Fig. 5.2(b) show the results obtained with SiC films grown at 400 mbar and 1280 °C and at 300 mbar and 1350 °C, respectively.

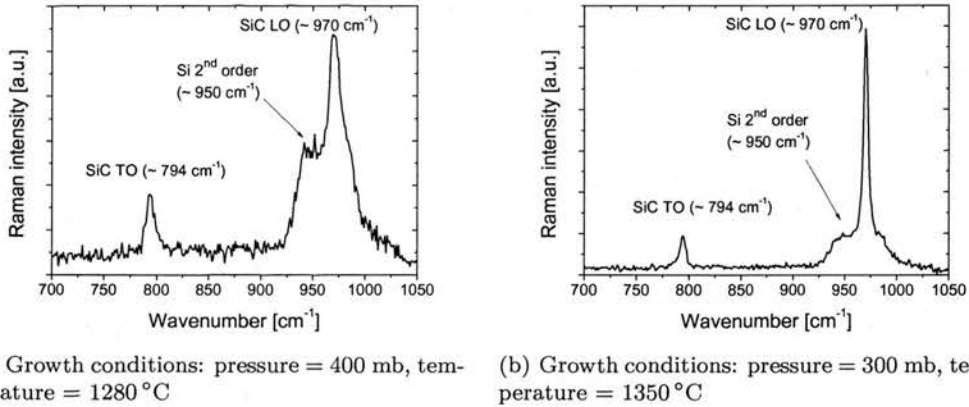


Figure 5.2: Raman spectra of SiC grown by hot-wall LPCVD.

For both films, the Raman peaks corresponding to the TO and LO phonon modes have

been detected at 794 and 970 cm^{-1} , respectively, indicating a 3C-SiC polytype [106]. In addition, a peak has been detected at 950 cm^{-1} corresponding to the second order mode of the Si substrate. The LO and TO peaks in the two spectra occur at the same position but with different intensities.

The ratio between the LO and TO phonon modes gives an indication of the quality of the SiC film [107], [105]. The higher LO/TO ratio indicates the presence of fewer defects in the SiC film. The SiC layer grown at lower pressure and higher temperature (Fig. 5.2(b)) has been shown to have an intensity ratio LO/TO of 6.3 that is higher compared to the ratio of 3 obtained for the layer grown at higher pressure and lower temperature (Fig. 5.2(a)). Therefore, the SiC film grown at lower pressure and higher temperature exhibits a higher crystal quality.

5.3 X-ray diffraction characterisation

As discussed in Chapter 2, single crystalline SiC layers can be grown by epitaxy and poly-crystalline SiC layers can be obtained if the film is grown on top of poly-Si. However, when single crystalline Si is used as a substrate, SiC films with single or poly-crystalline orientations can be obtained varying the growing conditions.

In order to investigate the possibility of obtaining different crystal orientations, different pressure and temperature conditions have been used for growing the SiC films provided by *Linköping University*. The crystallographic structure of the SiC films grown by hot-wall LPCVD has been characterised by X-ray diffraction (XRD). In this section, a brief explanation of the XRD mechanism has been given followed by the discussion of the results obtained.

5.3.1 Introduction to XRD

The XRD technique is based on the principle that X-rays interact with the electrons of the examined material. Some of the incident photons are diffracted because of the collisions with the electrons. Information about the atomic structure of the material can be obtained by detecting the X-rays scattered elastically. In crystals, the atoms are distributed periodically so that the incident waves are diffracted with certain angles depending on the atoms distribution.

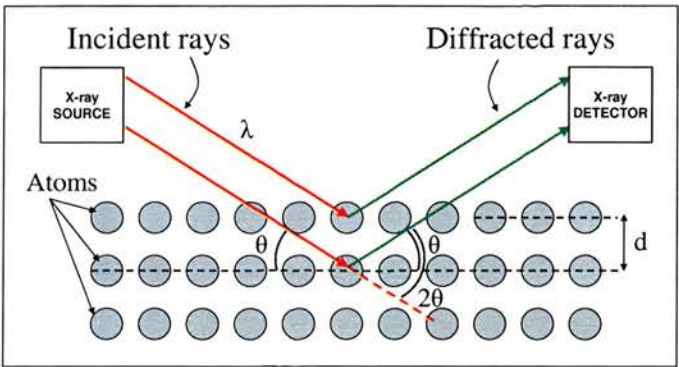


Figure 5.3: Schematic representation of the X-ray diffraction mechanism.

Fig. 5.3 shows a simple schematic representation of the interaction mechanism between the incident rays and electrons. The relationship between the wavelength λ of the incident rays, the diffraction angle θ and the lattice distance d is given by the Bragg's law $\lambda = 2d \cdot \sin\theta$. Usually, the intensity of the diffracted rays is plotted as a function of the diffraction angle. High intensity peaks are obtained for particular angles that can be associated to the lattice distance by solving the Bragg's equation. Therefore, the position of the high intensity peaks is used for deducing the crystal orientation of a specific material.

5.3.2 XRD measurements results

The results obtained from the XRD measurements performed on the SiC layers are presented.

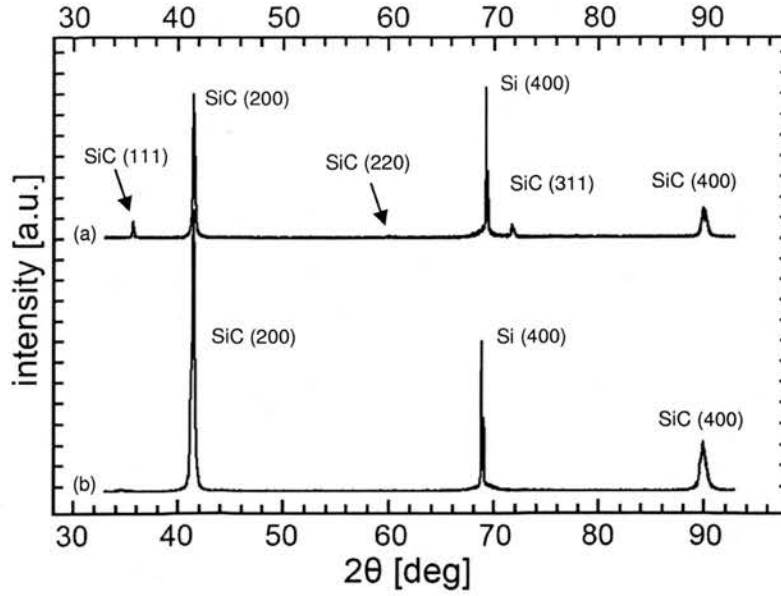


Figure 5.4: XRD of poly (a) and single (b) crystalline SiC layers grown on top of Si substrates.

Fig. 5.4 shows the XRD peaks obtained for SiC layers grown at 400 mbar and 1280 °C (Fig. 5.4(a)) and at 300 mbar and 1350 °C (Fig. 5.4(b)). In both cases, the peak relative to the single crystalline Si substrate is observed at about $2\theta \approx 69$ degrees. Fig. 5.4(a) shows dominant peaks associated with the (100) orientation together with other peaks for orientations such as (111), (220) and (311) indicating a poly-crystalline structure for the layer grown at 400 mbar and 1280 °C. Fig. 5.4(b) shows only two peaks associated with the SiC (100) orientation indicating a single crystalline structure for the layer grown at 300 mbar and 1350 °C.

5.4 Resonance measurement system and mechanical actuation

The SiC structures fabricated with the process flow described in Chapter 4 have been actuated mechanically in order to confirm the resonating ability of the devices. The

resonant frequency has been detected and measured optically with the use of a laser vibrometer.

Fig. 5.5 shows a schematic of the measurement setup utilised for the investigation of the resonant frequency. The chip with the structures to be tested has been mounted on a piezo-electric disc (piezo-disc). The disc has been placed into a vacuum chamber and mounted on movable stage (x and y stages) fitted under the objective of a Polytec OFV 3000 laser vibrometer. The actuating voltage has been applied with an Agilent signal generator that has been connected to the piezo-disc through an inlet of the vacuum chamber. When applying an alternating voltage to the piezo-disc, the induced vertical vibrations are transferred to the structures. In order to inspect the dynamical behaviour of the actuated devices, the vibrometer output signal has been connected to a computer and analysed with a LabView interface. With the setup described, the resonant frequency has been measured with an error of ± 10 Hz.

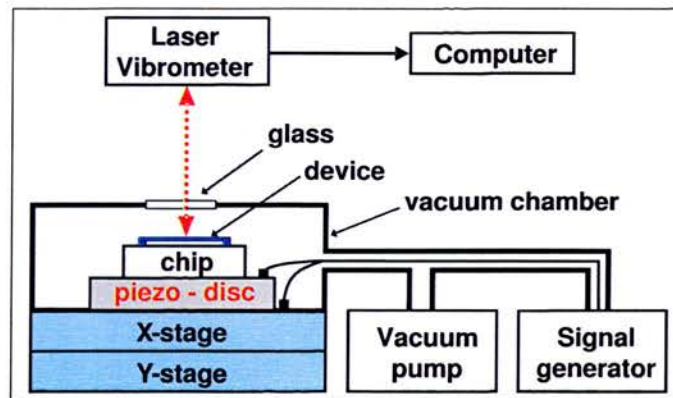


Figure 5.5: Schematic of the measurement setup for mechanical actuation and resonance detection of MEMS structure.

First, the structures' resonant frequency has been detected and investigated by mechanical actuation to verify the correct working state of the devices. Afterwards, other types of experiments such as electro-thermal and piezo-electric actuation and vibration amplitude detection (discussed in the next chapters) have been performed.

The measurement system has shown to be very feasible for investigating the devices'

resonance. In some cases, the low reflectivity of the SiC used has limited the vibrometer output signal and small vibration amplitudes have been difficult to detect. When actuating mechanically, the issues related to the SiC low reflectivity have been solved by coating the devices with a very thin layer of gold (evaporated with a thickness < 10 nm) thus enhancing the reflection of the laser beam and consequently maximising the output signal. When actuating electrically, the gold coating has not been employed in order to avoid the short-circuit of the actuating electrodes. However, in this case, the resonant frequency could be detected but the values obtained for the vibration amplitude have been probably lower than the actual ones.

5.5 Young's modulus calculation

This section presents the technique used for calculating the Young's modulus of the 3C-SiC layers provided by *Linköping University*. The calculation relies on the dependence of the Young's modulus on the fundamental mechanical frequency of a suspended structure.

Single clamped beams (i.e. cantilevers) have been fabricated as described in Chapter 4 using single and poly-crystalline SiC layers with thickness t of 2.3 and 1.4 μm , respectively. The Young's modulus has been calculated from the resonant frequencies measured for the fabricated beams. Three cantilevers for each length of 200, 150, 100 and 50 μm have been actuated mechanically and the natural resonant frequency inspected. During the fabrication process, the undercut at the anchor has been controlled and minimised in order to reduce the influence of root compliance on the calculation of the Young's modulus.

Resonant frequencies in a range 110 kHz - 1.5 MHz and 50 - 750 kHz have been obtained for the single and poly-crystalline devices, respectively. Fig. 5.6 shows two resonant peaks detected at 74.1 kHz ($Q \approx 1000$) and at 112.68 kHz ($Q \approx 6600$) for 200 μm long cantilevers fabricated with the poly-crystalline (Fig. 5.6(a)) and single crystalline

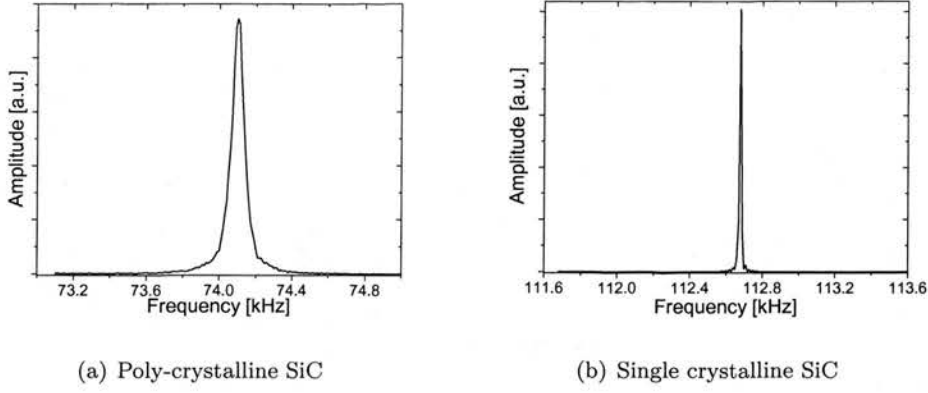


Figure 5.6: Measured resonant peaks when actuating mechanically the fabricated SiC cantilevers.

(Fig. 5.6(b)) SiC layers. Table 5.1 shows the resonant frequencies obtained for each cantilever's length and for the two different crystal orientation.

The Young's modulus E for both SiC layers has been calculated from the analytical formula of the cantilever's resonant frequency f_C (Eq. 3.5 in Chapter 3, Section 3.2.1):

$$f_C = 0.162 \sqrt{\frac{E}{\rho}} \frac{t}{L^2}, \quad (5.1)$$

where t and L are the thickness and the length of the cantilever, respectively, and ρ is the mass density of SiC. As discussed above, the undercut at the anchors of the fabricated cantilevers has been minimised so that the influence of root compliance on Eq. 5.1 could be neglected.

Average Young's modulus values of 446 ± 3 GPa and 246 ± 11 GPa have been calculated for the single crystalline layer ($t = 2.3 \mu\text{m}$) and for the poly-crystalline layer ($t = 1.4 \mu\text{m}$), respectively. For this calculation, the average value of E and its standard deviation have been calculated for each beam length. Then, an average of the values of E obtained for each length has been calculated excluding the values presenting a relatively high standard deviation. The final error has been estimated from the previously calculated standard deviation values. More details about the Young's modulus calculation are

(a) Poly-crystalline SiC

Length	Resonant frequency		
	device 1	device 2	device 3
[μm]	[kHz]	[kHz]	[kHz]
200	n.a.	57.5	74.7
150	118.9	119.2	96.5
100	215.5	208.6	214.5
50	730.0	745.0	727.0

(b) Single crystalline SiC

Length	Resonant frequency		
	device 1	device 2	device 3
[μm]	[kHz]	[kHz]	[kHz]
200	113.4	113.5	113.0
150	196.1	196.6	196.3
100	423.5	424.6	424.1
50	1483.0	1480.0	1250.0

Table 5.1: Measured resonant frequencies.

given in Appendix C.

The Young’s modulus obtained for the poly-crystalline SiC is very low compared to the values available in literature for stoichiometric 3C-SiC. A large standard deviation has been calculated for the average Young’s modulus obtained from the poly-crystalline SiC cantilevers with lengths of 200 and 150 μm . Therefore, when calculating the final Young’s modulus value, only the data obtained with cantilevers’ length of 100 and 50 μm have been used. In this case, the root compliance due to the anchor’s undercut has a larger influence on Eq. 5.1 thus reducing the value of the calculated Young’s modulus.

Fig. 5.7 shows the measured resonant frequency plotted for different cantilever’s lengths fabricated from the poly-crystalline (Fig. 5.7(a)) and single crystalline (Fig. 5.7(b)) layers. For comparison, the analytical curve, calculated using the obtained Young’s modulus, has been plotted. A good agreement between the experimental values and the analytical ones has been observed for cantilever’s lengths greater than 100 μm . The discrepancies observable for lengths of 50 μm are probably due to the undercut of the cantilever’s anchor during the release step. The presence of undercut at the

anchors makes the effective length of the cantilever longer so that the measured resonant frequency becomes lower (see Eq. 5.1), with the largest impact on the shortest cantilever.

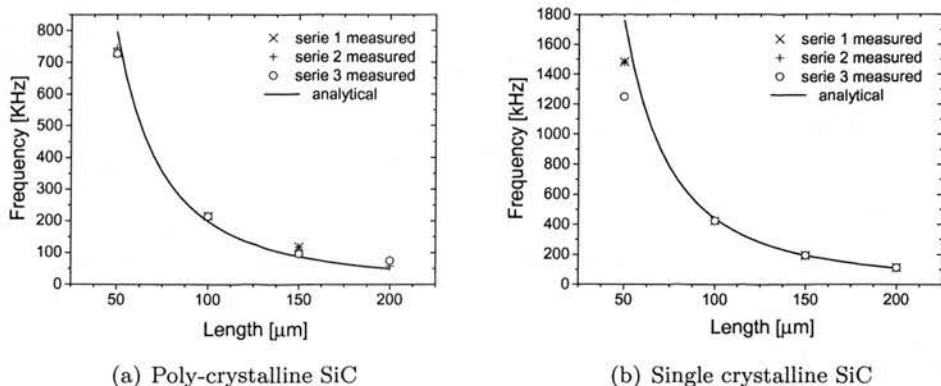


Figure 5.7: Measured and simulated SiC cantilevers resonant frequencies as a function of beams' length.

The technique of determining the Young's modulus of a thin film from the measured resonant frequency of a vibrating cantilever has been reported previously [108]. In the study presented in this chapter, beams with different lengths have been tested in order to minimise the influence of the anchor's undercut on the detected resonant frequency, hence leading to a more accurate calculation. Moreover, the fabricated cantilevers are relatively straight, indicating that the used growth and fabrication processes result in the presence of low internal and residual stress in the structures [109] [110]. Therefore, in Eq. 5.1, the influence of the stress on the resonant frequency could be neglected [111].

5.6 Conclusions

Materials characterisation is an important step for the optimisation of the performance of MEMS devices. The polytype, the crystal quality and orientation of the material used are essential factors for fabricating robust and reliable device structures.

In the first part of this chapter, Raman spectroscopy and X-ray diffraction (XRD) have been presented and introduced as non-destructive techniques to characterise the SiC films used for the fabrication of some devices studied in this thesis. The polytype and the crystal quality have been investigated by Raman spectroscopy while the crystal orientation has been analysed with XRD. The inspection has been carried out on two SiC layers grown on Si substrates by hot-wall LPCVD at different pressure and temperature conditions.

The Raman characterisation has indicated a 3C-SiC polytype for both SiC films showing a better crystal quality for the layer grown at lower pressure and higher temperature. In addition, from the XRD measurements, the film with a better crystal quality has been observed to have single crystalline orientation. The other layer, grown at higher pressure and lower temperature, has been observed to have a poly-crystalline orientation.

In the second part of the chapter, a measurement setup for testing MEMS devices has been presented. The testing system composed of a laser vibrometer connected to a computer has been used for measuring the resonant frequency optically and investigating the mechanical and electro-thermal behaviour of the devices studied in this thesis (see next chapters). The chips with the devices to be tested have been mounted on a piezo-electric disc and placed inside a vacuum chamber. By actuating piezo-electrically the disc, the induced vibrations have been transferred to the tested devices and their resonant frequency investigated with the vibrometer.

In addition, the Young's modulus of the SiC films has been calculated from the resonant frequency of cantilever beams. The process flow presented in the previous chapter has been used for fabricating single material SiC cantilevers. The testing system proposed has been used for actuating mechanically the fabricated cantilevers and for measuring their resonant frequency. A Young's modulus of 446 ± 3 GPa has been calculated for the SiC film that exhibited a good lattice quality and single crystalline orientation. A lower Young's modulus value of 246 ± 11 GPa has been obtained for the SiC film

having a relative poor lattice quality and poly-crystalline orientation.

Chapter 6

Electro-thermal actuation of SiC double clamped beam resonators with u-shaped electrodes

6.1 Introduction

In this chapter, the study of the electro-thermal behaviour of bimaterial Al/SiC double clamped (bridge) resonators is presented. The Al has been used as a top layer to implement the actuation electrode while the main structure to be actuated is made of SiC. The electrode's design plays an important role in the actuation of the bridge. As seen in Chapter 3, electro-thermal actuation is strictly related to the temperature gradients experienced by the structure. Therefore, the configuration, position and dimensions of the heating element are of key relevance for achieving an efficient actuation.

The electrode's architecture considered in this chapter is made of two Al arms, parallel to the longer side of the beam, connected by a perpendicular arm (u-shaped layout). This configuration has been studied with the use of finite element analysis (FEM) in order to determine the best electrode dimensions needed for maximising the deflection

of the structure. As a matter of fact, when considering the possibility of sensing the vibration electrically, relatively large displacements are preferred in order to facilitate the detection and enhance the electrical output.

Besides the simulations, the Al/SiC bridge resonators, fabricated as described in Chapter 4, have been actuated electro-thermally and the resonance of the structures measured. The vibration amplitudes at resonance have been investigated and compared with the simulated displacements.

6.2 Resonator and u-shaped electrode design

As discussed in Chapter 3, Section 3.2, a double clamped resonator is composed by a suspended beam clamped on both sides to an anchor thus forming a bridge structure. On top of the bridge, an electrode has been designed with two parallel arms connected by a perpendicular one. Fig. 6.1 shows the schematic of the designed SiC bridge structure and the associated Al electrode layout.

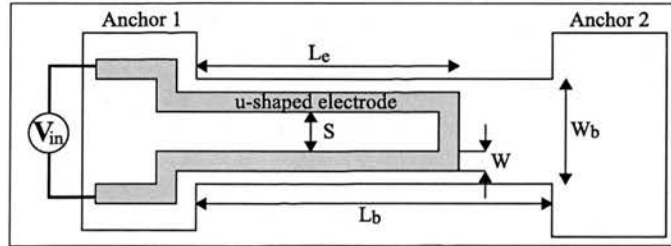


Figure 6.1: Schematic of the designed Al/SiC bridge resonators: u-shaped electrode layout with actuation voltage V_{in} applied.

The u-shaped configuration shown in Fig. 6.1 has been chosen because of its feasibility for analysing three different dimensional variations: the electrode's length (L_e), width (W) and spacing (S). In order to study only the influence of the electrode dimensions on the induced displacement, the beam dimensions have been fixed while the electrode ones have been varied. In particular, the beam thickness, width (W_b) and length (L_b) have been fixed at $2\text{ }\mu\text{m}$, $76\text{ }\mu\text{m}$ and $200\text{ }\mu\text{m}$, respectively. The electrode length (L_e),

width (W) and spacing (S) have been varied in the range 10 - 190 μm , 6 - 12 μm and 10 - 50 μm , respectively, and the thickness fixed at 0.5 μm .

6.3 Simulations

This section presents the results obtained from the FEM analysis of the electro-thermal actuation of the SiC bridges with top u-shaped Al electrodes.

The FEM analysis has been performed using *CoventorWare* (version 2004) as simulation software. The beam and the electrode have been fixed together and, in order to decrease the computational time, the substrate has been excluded from the analysis. As far as the mesh is concerned, elements with their top faces imprinted onto each other and extruded in the vertical directions have been used (extruded bricks created using a pave-type algorithm). The dimensions of the mesh elements have been optimised so that accurate results in reasonable computational times could be achieved. Therefore, initial simulations have been performed to test the accuracy of the results obtainable with different mesh element sizes (different number of elements). Bricks dimensions in (X,Y,Z) coordinates in a range between (1,1,0.5) μm (0.5 μm^3) and (4,5,2) μm (32 μm^3) have been considered. In this range, optimal brick dimensions of (2,2,0.5) μm (2 μm^3 corresponding to 15200 elements) have been chosen leading to displacement and resonant frequency accuracy of ± 1 nm and ± 1 Hz, respectively. As boundary conditions, the sides of the beam have been fixed and their temperature set at 300 K. Under these conditions, the two sides of the simulated beam correspond to the two clamped sides of the fabricated structures that are connected to the substrate thus acting as heat sink (fixed at room temperature in the measurements). The materials' parameters used for this study are listed in Appendix A. The actuation has been simulated by applying a DC voltage of 1 V across the top Al electrode as shown in Fig. 6.1. The value of 1 V has been chosen in order to match the DC voltage applied during the measurements. First, in order to understand the mechanism of electro-thermo-mechanical transduction

on the Al/SiC bridges, the effect of the actuation voltage on the general behaviour of the structure is observed. Then, the influence of the electrode dimensions on the induced displacement is discussed with the purpose of finding out the specifications for maximising the deflection. In particular, the influence of electrode length, width and spacing variations on the temperature changes within the beam are investigated.

6.3.1 General observations on the induced deflection

The effects obtained on the Al/SiC bridge by applying the actuation voltage to the top electrode are described. The attention is focused on the direction of the induced deflection and on the temperature changes.

When applying the voltage across the electrode, the overall structure Al electrode - SiC beam is observed to deflect vertically. The actuation electrode acts as a heater for the SiC bridge hence inducing a temperature change within the structure (see Chapter 3, Section 3.3.2). Before turning on the actuation voltage, the initial temperature T_0 of the structure is set at a constant value of 300 K (fixed by the boundary conditions at the anchors).

When the actuation voltage is turned on and the structure is in a steady-state, the final temperature T of the SiC beam is increased and its magnitude is observed to vary with the position along the beam. The difference between final and initial temperature is defined as $\Delta T = (T - T_0)$.

Besides the overall change of temperature, when the actuation voltage is on, different temperatures have been observed on the top and the bottom surfaces of the SiC beam due to the fact that the heating electrode is positioned on top of the beam and that the temperature at the bottom is fixed through the anchors at 300 K. The bottom and top temperature are referred as T_B and T_T , respectively, and their difference as vertical temperature difference $\Delta T_Z = (T_B - T_T)$.

For single material and bimaterial bridges, the effect of the temperature changes ΔT_Z

and ΔT are taken into account in the equations that describe the structure's maximum deflection (Chapter 3, Section 3.3).

In the particular case of a single material bridge, the maximum vertical deflection is a function of ΔT_Z and is given by Eq. 3.9 [78]:

$$y_{max} = \frac{1}{54} \frac{\gamma \Delta T_Z}{t} \frac{(2L_b - 3L_{\Delta T})^3 L_{\Delta T}}{(L_b - L_{\Delta T})^2}, \quad (6.1)$$

where t is the beam thickness, γ is the thermal expansion coefficient (TCE) of the beam material, $\Delta T_Z = (T_B - T_T)$ is the difference between bottom and top temperatures and assumed to be uniform along the beam length.

On the other hand, for a bimaterial bridge, the maximum vertical deflection is a function of ΔT and is given by Eq. 3.10 [78]:

$$y_{max} = \frac{1}{9} \frac{\Delta \gamma \Delta T (t_1 + t_2)}{K t_2^2} \frac{(2L_b - 3L_{\Delta T})^3 L_{\Delta T}}{(L_b - L_{\Delta T})^2}. \quad (6.2)$$

where index 1 and 2 are refer to the Al and SiC layers, respectively, $\Delta \gamma = (\gamma_2 - \gamma_1)$ is the difference between the two materials' TCE, $\Delta T = (T - T_0)$ is the difference between final and initial temperature (assumed uniform along the beam length), t_i and E_i are the thickness and the Young's Modulus of layer i , respectively, K is a positive constant proportional to E_i and t_i (see Chapter 3, Eq. 3.11).

If the deflection of the beam is observed in detail along its entire length, two different cases can be distinguished:

- i. Negative deflection where there is no electrode (single material part),
- ii. Positive deflection where the electrode overlaps the beam (bimaterial part).

Fig. 6.2 shows a schematic side view and a simulation snapshot of the Al/SiC bridge with the two different directions of deflection highlighted by the arrows in Fig. 6.2(a).

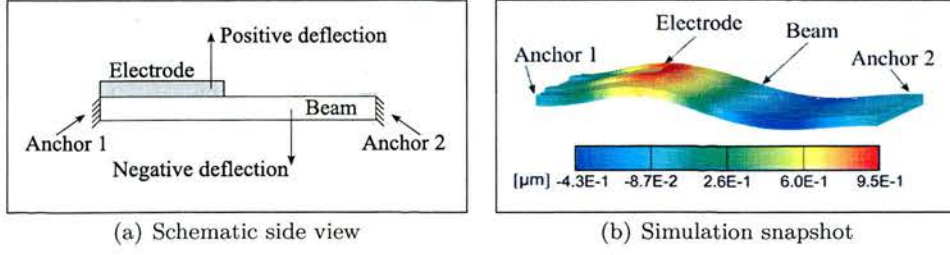


Figure 6.2: Simulations, u-shaped layout: illustration of the direction of the simulated deflections.

6.3.1.1 Negative deflection - single material thermal expansion effect

In the part of the beam where there is no electrode, only one material expands and the observed deflection is negative. To explain this behaviour, Eq. 6.1, that describes the maximum deflection of a single material bridge subjected to a temperature change, has to be considered. In the specific case of an electrode placed on top of the beam, the top temperature is higher than the bottom one making the vertical temperature difference ΔT_Z negative. In addition, the factor on the right hand of ΔT_Z is always positive as long as the length of the heated up area along the beam, where ΔT_Z has influence, $L_{\Delta T}$ is $< \frac{2}{3}$ of the entire length of the structure. Under these conditions, the displacement of the single material part of the beam is negative.

6.3.1.2 Positive deflection - bimaterial thermal expansion effect

On the contrary, a positive deflection occurs in the bimaterial part of the beam, where the electrode is overlapping the beam. In this case, Eq. 6.2, that describes the maximum deflection of a bimaterial bridge subjected to a temperature change, has to be considered. In Eq. 6.2, the conditions for a positive deflection are satisfied in the bimaterial part of the structure. In fact, the difference ΔT is always positive, the right hand term is negative because from the simulations $L_{\Delta T}$ is $> \frac{2}{3}$ of the length of the beam and $\Delta \gamma$ is negative because the TCE of Al ($\gamma_{Al} = 23.5 \cdot 10^{-6} \text{ K}^{-1}$) is higher than the SiC one ($\gamma_{SiC} = 2.5 \cdot 10^{-6} \text{ K}^{-1}$). Under these conditions, a positive deflection is

generated.

6.3.2 Influence of electrode length L_e on the bridge deflection

It has been observed that when applying the actuation voltage, the structure experiences an out-of-plane vertical deflection with an overall direction that depends on the electrode length L_e . The influence of L_e on the direction and on the magnitude of the deflection has been investigated.

As discussed above, a deflection in the vertical positive direction always occurs in the part of the bridge where the electrode is located (bimaterial part) and a deflection in the vertical negative direction is experienced on the area where there is no electrode (single material part) (Fig. 6.2). These two deflections in opposite directions interact together influencing the observed overall maximum displacement that could be positive or negative with respect to the initial position of the structure. This effect can be observed in Fig. 6.3, where the maximum displacement of the bridge is plotted as a function of the electrode length L_e with $W = 9 \mu\text{m}$ and $S = 30 \mu\text{m}$. The maximum deflection is negative when L_e ranges between 10 and 60 μm and positive for $L_e > 60 \mu\text{m}$. L_S is defined as the electrode length at which the sign of the deflection switches (in this case $L_S = 60 \mu\text{m}$).

In the previous sections and in Chapter 3, the deflection of structures excited electro-thermally has been shown to be strictly related to the temperature gradients generated when the actuation voltage is applied. As a matter of fact, the analytical formulas for single material (Eq. 6.1) and for bimaterial (Eq. 6.2) structures are proportional to the vertical temperature difference (ΔT_Z) and to the difference between final and initial temperature ($\Delta T = T - T_0$), respectively. Therefore, in order to explain the existence of positive and negative deflections along the bridge, the simulated temperature along the beam has been analysed. Fig. 6.4 shows the temperature changes ΔT and ΔT_Z as a function of the position along the beam for the different electrode lengths L_e . By

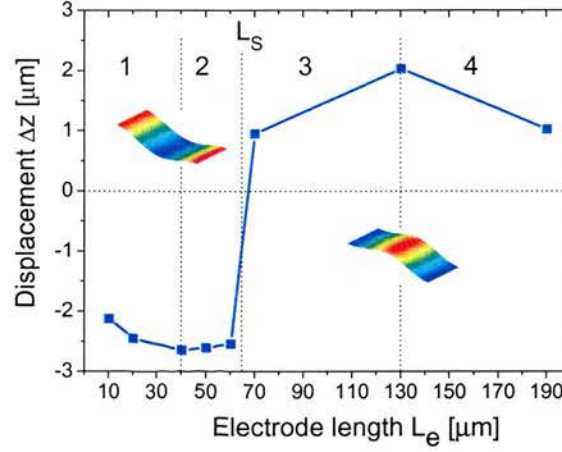


Figure 6.3: Simulations, u-shaped layout: maximum displacement for $L_b = 200 \mu\text{m}$ and $W_b = 76 \mu\text{m}$ as a function of the electrode length L_e (electrode width $W = 9 \mu\text{m}$, electrode spacing $S = 30 \mu\text{m}$).

applying the actuation voltage across the top electrode, the structure experiences at the same time an increase of temperature from T_0 to T (Fig. 6.4(a)) and a vertical temperature difference ΔT_Z (Fig: 6.4(b)). As discussed above, ΔT_Z is associated to the single material expansion and ΔT to the bimaterial expansion. Therefore, the simultaneous presence of these two temperature gradients shows that the deflection of the beam is influenced by both the single material and bimaterial thermal expansion effects. However, the vertical temperature gradient ΔT_Z decreases strongly for $L_e > 70 \mu\text{m}$ hence its influence is stronger for short electrode lengths ($L_e < 60 \mu\text{m}$).

From Fig. 6.3, four different cases can be defined as a function of L_e for the simulated displacement:

1. $L_e \ll L_S$ ($L_e < 40 \mu\text{m}$),
2. $40 \mu\text{m} < L_e < L_S$,
3. $L_S < L_e < 130 \mu\text{m}$,
4. $L_e > 130 \mu\text{m}$,

with L_S defined as the length at which the deflection switches.

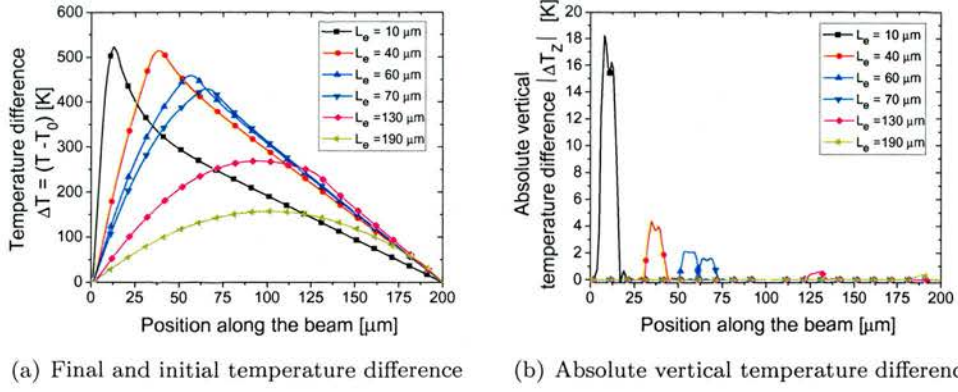


Figure 6.4: Simulations, u-shaped layout: temperature data of 200 μm long bridges for different electrode lengths L_e .

6.3.2.1 $L_e \ll L_S$, single material behaviour

For electrode lengths $L_e \ll L_S$ ($L_e < 40$ μm), the simulated ΔT_z (Fig. 6.4(b)) is relatively large while the bimaterial surface is small hence the bridge can be considered simply as a single material structure. In this design, the conditions for negative displacements are met because the length $L_{\Delta T}$ of the heated up area along the beam is $< \frac{2}{3} L_b$ and the temperature at the top of the beam is higher than the bottom part of the beam. However, a very small positive deflection is observed where the electrode overlaps the beam but is diminished by the reaction force exerted by anchor 1 (see Fig. 6.1). This effect can be observed in Fig. 6.5(a) showing the simulation snapshot for the case $L_e = 10$ μm. Moreover, in Fig. 6.3, when L_e increases towards L_S , the magnitude of the maximum displacement increases and reaches a maximum for $L_e = 40$ μm. However, ΔT_z drops with the increase of L_e (Fig. 6.4(a)) and the magnitude of the deflection would be expected to decrease as well. The negative deflection is observed to increase probably due to the more uniform heating of the structure as the electrode shifts towards the centre of the beam.

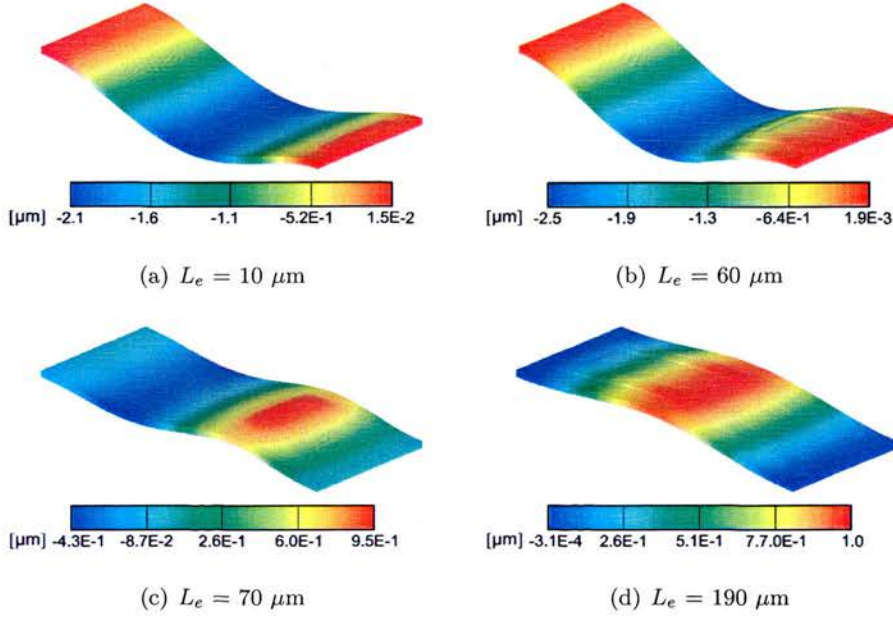


Figure 6.5: Simulations, u-shaped layout: snapshots for 200 μm long bridge as a function of the electrode length L_e ($W = 9 \mu\text{m}$ and $S = 30 \mu\text{m}$).

6.3.2.2 $40 \mu\text{m} < L_e < L_S$, single material - bimaterial behaviour

With the increase of the electrode length, the bimaterial effect starts to influence the beam behaviour and the magnitude of the negative displacement starts to decrease. When the value of L_e becomes close to L_S , the bridge behaves as a combined single material - bimaterial structure. The observed magnitude of the positive deflection, located on the electrode, appears and contrasts the negative deflection, located on the single material side of the beam (Fig. 6.5(b)). This interaction causes the negative displacement to decrease as the electrode length is increased from 40 μm to $L_S = 60 \mu\text{m}$.

6.3.2.3 $L_S < L_e < 130 \mu\text{m}$, single material - bimaterial behaviour

For $L_S < L_e < 130 \mu\text{m}$, both the single material and the bimaterial behaviours are still observed. However, when $L_e > L_S$, the bimaterial behaviour overcomes the single

material one and the maximum deflection becomes positive. This effect can be observed in Fig. 6.5(c) showing the simulation snapshot for $L_e = 70 \mu\text{m}$. Moreover, when L_e increases from $70 \mu\text{m}$ to $130 \mu\text{m}$, the maximum displacement becomes increasingly positive. In this case, the observation is believed to be due to the increase of the bimaterial effect overcoming the decrease of the single material effect. In fact, the bimaterial effect increases as the amount of bimaterial area increases with the electrode length. On the contrary, the single material effect is observed to decrease as a consequence of the decrease of ΔT_Z caused by the increase of the electrode length (Fig. 6.4(b)).

6.3.2.4 $L_e > 130 \mu\text{m}$, bimaterial behaviour

For a further increase of L_e from $130 \mu\text{m}$ to $190 \mu\text{m}$, the single material effect disappears ($\Delta T_Z \approx 0$) leaving only the bimaterial effect ($\Delta T \neq 0$) to govern the behaviour of the structure. The magnitude of the maximum displacement decreases because the temperature of the beam decreases (Fig. 6.4(a)). The drop of temperature is due to the fact that as the electrode length increases, a larger area of the beam has to be heated up and the electrode becomes closer to anchor 2 fixed at 300 K. In the case of $L_e < 130 \mu\text{m}$, described in the previous section, the decrease of temperature is compensated by the increase of the amount of expanding material thus the displacement has been observed to increase with the increase of electrode length. However, when $L_e > 130 \mu\text{m}$, the reaction force exerted by anchor 2 has a stronger influence on the mechanical behaviour of the beam thus having a damping effect on the induced displacement as the electrode length increases (Fig. 6.1).

6.3.3 Influence of electrode width W on the bridge deflection

The dependence of the simulated absolute displacement on the electrode width W has been analysed in order to optimise the electrode design for achieving maximum deflection. For this study, the absolute displacement has been investigated for electrode

widths W equal to 3, 6 and 9 μm , varying the electrode length L_e between 10 and 190 μm and fixing the electrode spacing S at 30 μm .

When applying the actuating voltage to the top electrode of the structure, the magnitude of the deflection has been observed to be related not only to the electrode length L_e but also to its width W . The absolute values of the displacement obtained with the different widths have been compared and discussed by observing the average and maximum temperature induced in the SiC bridge. The relationship between the induced temperature and the electrode length, observed in the previous section, has been confirmed and similar observations can be made here. However, because this section focuses mainly on the effects of the electrode width variations, the temperature figures are discussed as a function of W rather than L_e .

Fig. 6.6 summarises the results for the displacement and temperature obtained from the simulations. The absolute maximum displacement (Fig. 6.6(a)) and the average and maximum temperature (Fig. 6.6(b)) have been plotted as a function of L_e for $W = 6, 9, 12 \mu\text{m}$ and $S = 30 \mu\text{m}$. The maximum displacement has been plotted with its absolute value for facilitating the comparison between the curves.

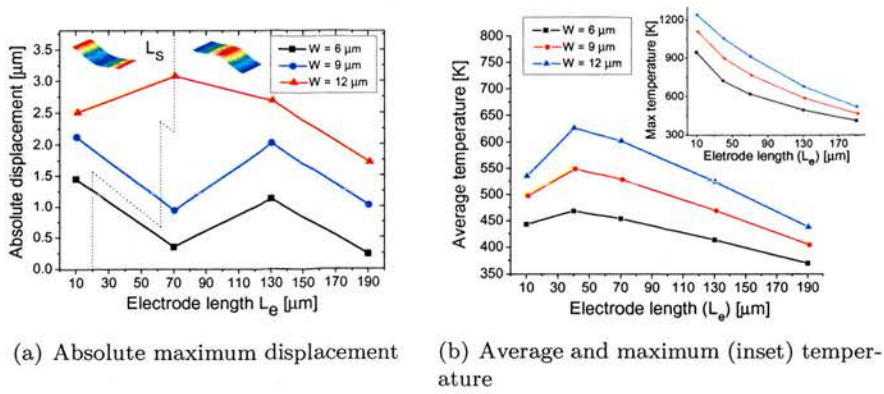


Figure 6.6: Simulations, u-shaped layout, width variations: displacement and temperature as a function of the electrode length L_e for electrode width $W = 6, 9, 12 \mu\text{m}$ (electrode spacing $S = 30 \mu\text{m}$).

From Fig. 6.6(a), the trend of all the curves for the maximum displacement is similar

to the one obtained in the previous section showing a negative displacement for short electrode lengths ($L_e < L_S$) and a positive one for long electrodes ($L_e > L_S$). This behaviour has been highlighted with the snapshots obtained from the simulations and plotted in the insets of Fig. 6.6(a).

The dotted line in Fig. 6.6(a) shows the electrode length L_S at which the transition from downward to upward bending occurs. The value of the electrode length L_S increases from 20, 60 to 70 μm for W increasing from 6, 9 and 12 μm . This is probably due to the interaction of the vertical temperature gradient ΔT_Z , that pushes the beam downwards (as in the single material case), and the overall thermal expansion of the resonator material, related to the temperature difference ΔT (as in the bimaterial case), that pushes the beam upwards. As the electrode width increases, the heating is more effective so that the vertical temperature gradient ΔT_Z effect becomes larger. Therefore, the L_S switching point will be reached at longer electrode length as the electrode width increases (i.e. L_S is shifted to greater values).

It is important to observe that by increasing the electrode width W the maximum displacement increases. This effect can be explained by investigating the average temperature (T_{av}) and the maximum temperature (T_{max}) induced within the beam. From Fig. 6.6(b), both temperature figures T_{av} and T_{max} increase when W is increased. Therefore, increasing the electrode width serves to increase the heater's area and generate a higher temperature. These two effects enhance the material's thermal expansion and consequently the magnitude of the deflection. The relatively high values observed for the simulated temperatures are related to the fact that the effect of the heat dissipation by convection and radiation has not been included in the simulations. However, the obtained values and trends are meaningful for describing the temperature variations induced when applying an actuating voltage to the structures.

The highest absolute displacements are achieved with the largest electrode configuration ($W = 12 \mu\text{m}$). From a design point of view, this observation is important for optimising

the actuation efficiency of the bimaterial Al/SiC structure.

6.3.4 Influence of electrode spacing S on the bridge deflection

After studying the influence of the electrode width W on the absolute displacement, the effect of the variations in the electrode spacing S have been analysed aiming to maximise the deflection of the bridge.

Similar to the study of the width variations, the simulated absolute displacement has been compared for values of spacing S equal to 10, 30 and 50 μm varying the electrode length L_e between 10 and 190 and fixing the electrode width W at 7 μm . The displacement has been observed to be influenced by the electrode spacing S and, confirming the results discussed in the previous sections, on the electrode length L_e . The values obtained from the simulations of the average and the maximum temperature induced in the SiC bridge have been used in the discussion for explaining the results obtained.

Fig. 6.7 summarises the results for the simulated displacement and temperature. The absolute maximum displacement (Fig. 6.7(a)) and the average and maximum temperature (Fig. 6.7(b)) have been plotted as a function of L_e for $S = 10, 30, 50 \mu\text{m}$ and $W = 7 \mu\text{m}$. As in the study of the width variations, the maximum displacement has been plotted with its absolute value for facilitating the comparison between the curves.

In Fig. 6.7(a), the change in the direction of the deflection from negative to positive, discussed in Section 6.3.2, is highlighted by the dotted line and with the simulations snapshots plotted in the insets. The change in the electrode spacing S does not influence the value of L_S at which the deflection switches.

It can be seen that the simulated maximum displacement decreases as the electrode spacing increases. An explanation to this effect can be found by observing the average temperature (T_{av}) and maximum temperature (T_{max}) induced within the beam. From Fig. 6.7(b), T_{av} and T_{max} drop as the electrode spacing is increased due to the enlargement of the beam area in between the electrode arms that is heated up. A

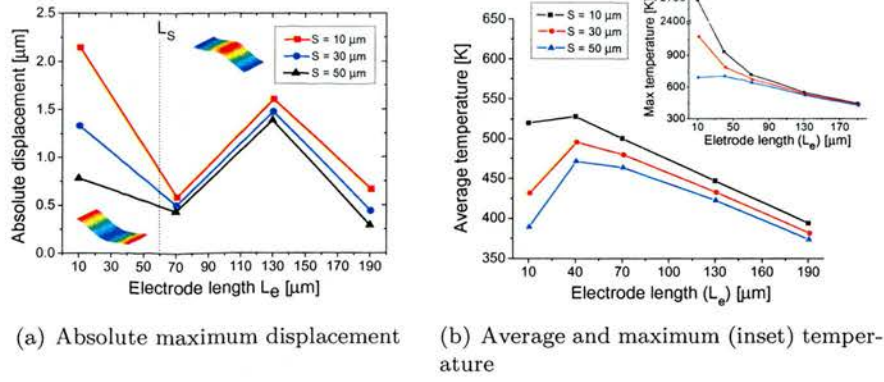


Figure 6.7: Simulations, u-shaped layout, spacing variations: displacement and temperature as a function of the electrode length L_e for electrode spacing $S = 10, 30, 50 \mu\text{m}$ (electrode spacing $W = 7 \mu\text{m}$).

significant example of this effect can be found in the decrease of the magnitude of the displacement when the electrode is applied at the root of the bridge ($L_e = 10 \mu\text{m}$). By comparison with Fig. 6.7(b), it can be seen that when S is increased from $10 \mu\text{m}$ to $30 \mu\text{m}$, the average temperature reduces to 20% of its initial value and a further reduction is observed for a further increase of S to $50 \mu\text{m}$.

The absolute displacement of the Al/SiC bridge is maximised when the electrode spacing S is minimised so that the electrode arms are close to each other. This observation is important if the design of the electrode has to be optimised in order to achieve maximum deflections.

6.4 Measurements: electro-thermal actuation and resonance detection

In this section, the results obtained from the testing of the fabricated bimaterial Al/SiC resonators are presented. The fabricated devices have been actuated electro-thermally and the resonant frequency detected with an optical technique.

The resonators have been fabricated as described in Chapter 4 and with the same

dimensional variations of the simulated structures. The devices have been tested at room temperature and under vacuum with a similar setup to the one described for the mechanical actuation of single material SiC resonators (Chapter 5, Section 5.4). With the measurement setup used, the resonant frequency has been determined with an error of ± 10 Hz. However, in this case, the structures have been actuated electro-thermally. Therefore, the fabricated chips have been mounted on a chip carrier plugged in a testing socket and a signal generator has been used to apply an input voltage across the actuation electrodes of the structures as shown in Fig. 6.1. A schematic of the measurement setup is shown in Fig. 6.8.

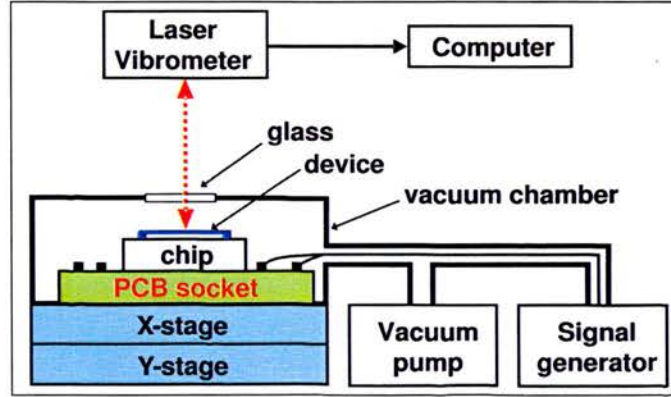


Figure 6.8: Measurement setup for the electro-thermal actuation of the fabricated Al/SiC bimaterial bridges.

Electro-thermal actuation has been performed by applying an input voltage $V_{in} = V_{ac} \sin \omega_{ac} t + V_{dc}$, having an AC amplitude $V_{ac} = 4$ V, a DC bias $V_{dc} = 1$ V and sweeping the input frequency ($f_{in} = \omega_{ac}/2\pi$) in a range ± 300 kHz around the resonant frequency value obtained with the simulations ($f_{res} = 585$ kHz for the $200 \mu\text{m}$ long beams). Fig. 6.9 shows a resonant peak at 694 kHz obtained when actuating electro-thermally one of the fabricated bridges. The calculated quality factor Q is ≈ 10000 .

The measured frequencies are in the range 650 - 700 kHz. The difference between the resonant frequency values obtained with the mechanical simulations and the ones obtained by electro-thermal actuation are attributed to the discrepancies between the

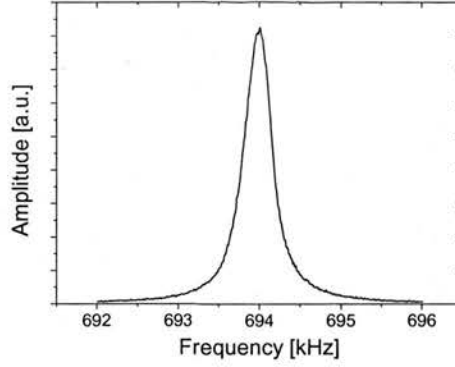


Figure 6.9: Measurements, u-shaped layout: resonant peak of an electro-thermally actuated Al/SiC bridge resonator 200 μm long and 2 μm thick ($Q \approx 10000$).

theoretical and actual parameters. The existence of tensile stress in the fabricated structures, due to the presence of residual stress resulting from the fabrication process and thermal stress consequence of the electro-thermal actuation, could give rise to the higher resonant frequencies detected. In addition, it is worth to notice that the resonant frequency is linearly dependent on the thickness of the beam (see Eq. 3.6). In the fabrication process used, the thickness of the final structure is determined by the thickness of the SiC and Al films. The possible non-uniformities in the materials' thickness, resulting from the growth and deposition processes, could influence the actual resonant frequency of the devices.

6.5 Measurements: vibration amplitude

The electro-thermal actuation performance of the u-shaped electrode layout has been investigated by measuring the vibration amplitude at resonance of the Al/SiC bimaterial bridges. The amplitude of the vibration has been observed as a function of the electrode length L_e for different electrode width W and spacing S . The tested devices have been fabricated with the same dimensions of the simulated ones so that the measurements results could be compared with the simulations performed.

The resonance of the structures has been detected as reported in the previous section with $V_{ac} = 4$ V, $V_{dc} = 1$ V, $f_{in} \leq f_{res} \pm 300$ kHz. Once the resonance has been detected by electro-thermal actuation, the input frequency has been fixed to match the exact value of the resonant frequency ($f_{in} = f_{res}$) so that the vibration amplitude at resonance could be measured with an error of ± 5 nm. The electrode length L_e , width W and spacing S have been observed to influence the bridges' vibration amplitude.

6.5.1 Influence of the electrode width W on vibration amplitude

The measured vibration amplitudes have been analysed as a function of L_e for different W . As mentioned before, the devices have been fabricated with the same dimensional variations of the simulated ones so that a comparison could be made between the trend of the measured vibration amplitude and the absolute simulated displacements and temperature (presented in Section 6.3.3). The influence of L_e and W on the vibration amplitude is discussed.

Fig. 6.10 shows the measurement results as a function of the electrode length L_e , for electrode widths $W = 6, 9, 12$ μm and spacing $S = 30$ μm . The trend of the measured vibration amplitudes as a function of L_e agrees with the one for the simulated absolute displacement (Fig. 6.6(a)). The influence of the single material and bimaterial effects on the vibration amplitude can be observed for all the electrode widths being more evident when $W = 6$ μm . In this case, the detected amplitude is observed to decrease when L_e is increased from 10 to 70 μm , to increase for a further increase of L_e to 130 μm and to decrease again when $L_e = 190$ μm .

The detected values range between 60 nm and 160 nm and are observed to increase when the electrode width W is increased. This result is in good agreement with the simulated absolute displacements that increase as W increases (Fig. 6.6(a)) and can be explained by the temperature simulations performed (Fig. 6.6(b)). As a matter of fact, as the electrode becomes wider, a higher temperature along the beam is generated

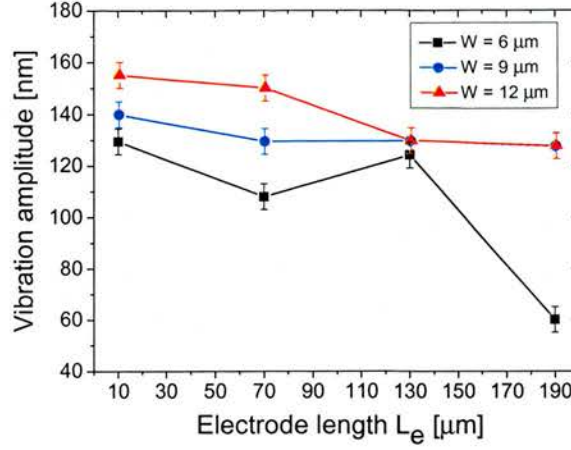


Figure 6.10: Measurements, u-shaped layout: vibration amplitude for 200 μm long bridges as a function of the electrode length L_e for different electrode width W .

so that the thermal expansion of the structure is enhanced hence giving rise to larger vibration amplitudes.

The simulated displacements and the measured vibration amplitudes differ by one order of magnitude. This difference is probably due to the presence of tensile and residual stress in the fabricated structures. In addition, it is believed that, because of the heat dissipation through the substrate, the temperature induced in the tested devices is lower than the simulated one. Under these conditions, the generated vibration amplitude is diminished. Furthermore, the detected amplitude could be affected by the low signal output of the measurement system due to the poor reflectivity of SiC.

It is worth pointing out that relatively large amplitudes are detected when an electrode having a large width is applied at the root of the beam corresponding to the absolute maximum displacement observed in the simulations. This result shows that an effective actuation can result when wide electrodes are applied close to the root of the bridge.

6.5.2 Influence of the electrode spacing S on vibration amplitude

The measured vibration amplitudes obtained when actuating with electrodes having different spacing S have been analysed as a function of the electrode length L_e . The tested devices had the same dimensions as in the simulations so that the trend of the measured vibration amplitude can be compared to the simulated absolute displacement and temperature presented in Section 6.3.4. The influence of L_e and of S on the vibration amplitude is discussed.

Fig. 6.11 shows the measured vibration amplitude as a function of the electrode length L_e for electrode spacing $S = 10, 30$ and $50 \mu\text{m}$ with $W = 7 \mu\text{m}$. The general trend of the measured vibration amplitude follows the one of the simulated absolute displacement (Fig. 6.7(a)). The combination of the single material and bimaterial effect is influencing the electro-thermal behaviour of the structure resulting in changes of the vibration amplitude as a function of the electrode length L_e . For all the electrode spacings S , the amplitude is seen first to decrease when L_e is increased from 10 to $70 \mu\text{m}$ and then to increase for a further increase of L_e to $130 \mu\text{m}$. When L_e is increased to $190 \mu\text{m}$, a decrease in the vibration amplitude has been observed for $S = 10$ and $50 \mu\text{m}$. However, in the case $S = 30 \mu\text{m}$, when L_e was increased from 130 to $190 \mu\text{m}$, an increase of amplitude has been detected. This difference in the behaviour between the case with $S = 10$ or $50 \mu\text{m}$ and $S = 30 \mu\text{m}$ is probably due to the fact that in some cases the beams were over-released (large undercut at the anchor), hence the effective beam length was greater than $200 \mu\text{m}$ thus making the relative electrode length shorter. Under these conditions, the detected resonant frequency is lower compared to the average value. Moreover, when the beam is over-released, the structure is anchored further away from the electrode thus the damping effect exerted by the reaction force of anchor 2 (Fig. 6.1) is weaker.

The measured values range between 50 nm and 180 nm and increase when the spacing S decreases. This result agrees with the simulated absolute displacement (Fig. 6.7(a))

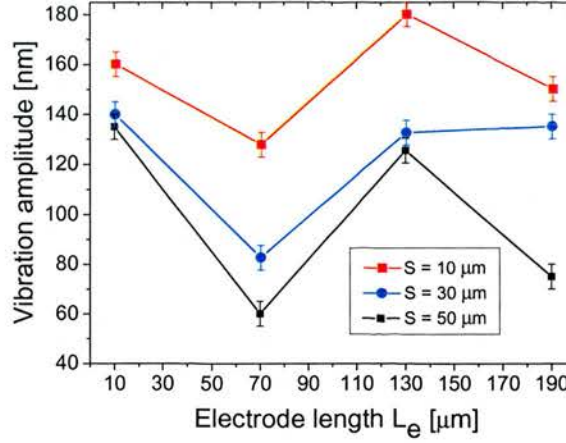


Figure 6.11: Measurements, u-shaped layout: vibration amplitude for 200 μm long bridges as a function of the electrode length L_e for different electrode spacing S .

that is seen to increase as the spacing S in between the electrodes becomes larger. An explanation can be found by observing the temperature simulations performed (Fig. 6.7(b)). As a matter of fact, by decreasing S the area between the electrode arms is reduced so that a smaller amount of material has to be heated up. Under these conditions, the generated temperature is higher leading to an enhancement of the thermal expansion of the structure and consequently to larger vibration amplitudes.

6.6 Conclusions

In this chapter, the study of the electro-thermo-mechanical transduction in bimaterial Al/SiC bridges has been presented. In particular, the influence of the dimensions of a u-shaped Al electrode on the actuation mechanism and on the bridge displacement has been investigated by finite element (FEM) simulations. In addition, measurements have been performed in order to study the influence of the electrode dimensions on the vibration amplitude at resonance.

From the simulations, it has emerged that the Al/SiC bridges behave at the same time as single material and bimaterial structures depending on the magnitude of the

temperature gradients generated by the electrode. It has been shown that the single material behaviour leads to a negative displacement on the side where the Al does not overlap the SiC while the bimaterial behaviour forces a positive displacement on the overlapping area between Al and SiC. The two opposite displacements interact together influencing the overall maximum displacement that has been observed to be either negative or positive.

The direction of the deflection depends on the electrode length. Negative deflections have been observed for short electrode lengths while longer electrodes give rise to positive deflections. High deflections values are obtained when wide electrodes with a short distance in between the electrode arms are placed close to the root of the beam.

Bimaterial Al/SiC bridges have been fabricated successfully with the same dimensions used for the simulations. The devices have been driven into vibration electro-thermally, the resonant frequency detected and the amplitude of the structures' vibration at resonance has been measured. In agreement with the trend of the simulated maximum displacement, it has been shown that large vibration amplitudes can be achieved by actuating with short and wide electrodes with the spacing between the electrode arms minimised. One of the most significant findings is that the simulated absolute displacement and the measured vibration amplitude induced with electrodes applied close to the root of the beam are comparable with the ones obtained with electrodes covering $\sim \frac{2}{3}$ of the beam length.

The results discussed in this chapter show that short electrodes can be used for performing electro-thermal transduction without decreasing the actuation efficiency. Moreover, for the purpose of detecting electrically the resonant frequency or the vibration amplitude, if a short actuation electrode is used, the remaining area of the beam is left available for designing additional sensing electrodes.

Chapter 7

Electro-thermal actuation of SiC double clamped beam resonators with slab electrodes

7.1 Introduction

In Chapter 6, the efficiency of the electro-thermal actuation with u-shaped electrodes in bimaterial Al/SiC bridge resonators has been optimised. In particular, it has been proved that when using a u-shaped electrode configuration the magnitude of the simulated displacement and the measured vibration amplitude can be enhanced by increasing the electrode width and decreasing the spacing between the electrode arms. In addition, the displacement and vibration amplitude induced by a u-shaped electrode applied close to the root of the beam are comparable to the ones obtained with the electrode covering $\sim \frac{2}{3}$ of the beam length.

This chapter explores the possibility of maximising the displacement and vibration amplitude induced electro-thermally on Al/SiC bridges. The width and the spacing of the u-shaped configuration have been maximised and minimised, respectively, thus

obtaining a plain plate (i.e. slab) layout. It is believed that by enlarging the area of the heating electrode, the generated temperature can be enhanced hence inducing higher displacements. The electro-thermal behaviour of the overall structure has been studied with the same methodology presented in Chapter 6 and focusing on the influence of the slab electrode length on the electro-thermal actuation mechanism of the bridge. In fact, the position of the electrode is still of key relevance so that the deflection can be optimised to reach a good compromise between the area defined for the actuation and the one defined for a possible sensing electrode.

In the first part of the chapter, the slab architecture has been studied with the use of FEM simulations to observe the induced displacement and temperature gradients. After, the SiC bridges fabricated with top slab Al electrodes have been actuated electro-thermally. In particular, the vibration amplitude at resonance has been measured and the results compared with the simulated ones.

In the second part of the chapter, in order to determine the most efficient actuation electrode layout, the performance of the slab configuration is compared to the u-shaped one. The electro-thermal actuation of bimaterial bridges with u-shaped electrodes has been simulated. The induced displacement and temperature have been compared to the ones obtained for the slab configuration. A further comparison has been made actuating electro-thermally the fabricated devices and measuring the vibration amplitude at resonance.

7.2 Resonator and slab electrode design

The bridge resonator considered in this chapter is similar to the one designed for the study of the u-shaped electrode configuration presented in Chapter 6. The main difference is that the top Al electrode has been designed as plain plate (i.e. slab).

Fig. 7.1 shows the schematic of the designed structure and the associated electrode

layout. For the study of this electrode configuration, the beam dimensions have been fixed at $W_b = 60 \mu\text{m}$ and $L_b = 150 \mu\text{m}$. The slab length L_e has been varied in a range 15 - 150 μm with the width W fixed at 30 μm .

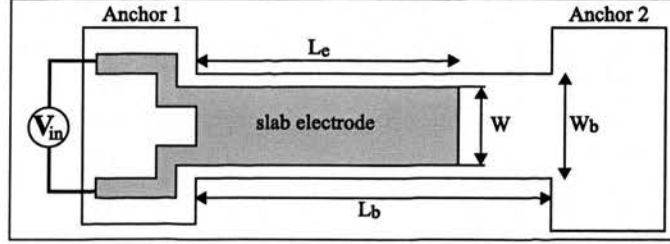


Figure 7.1: Schematic of the designed Al/SiC bridge resonators: slab electrode layout with actuation voltage V_{in} applied.

7.3 Simulations: the slab electrode

This section presents the results obtained from the simulations of Al/SiC bridges actuated electro-thermally with the slab electrode (Fig. 7.1).

The beam anchors have been fixed to the substrate and their temperature set at 300 K. The effect of the residual stress in the structure has been taken into account setting the stress in the SiC material's parameters at 400 MPa (Appendix A) [51]. The induced simulated displacement has been investigated when applying a DC voltage of 1 V across the electrode as shown in Fig. 7.1.

The temperature difference ΔT and ΔT_Z , introduced in Chapter 3 and Chapter 6, have been used to explain the influence of the slab architecture on the magnitude of the induced deflections. ΔT is the difference between the final temperature T , observed at steady-state when the actuation voltage is on, and the initial temperature T_0 , experienced by the structure before turning on the actuation voltage, fixed at 300 K by the boundary conditions ($\Delta T = T - T_0$). ΔT_Z is the vertical temperature difference between the temperature of the bottom surface T_B and the temperature of top surface T_T of the structure, observed when the actuation voltage is on and the beam is in a

steady-state ($\Delta T_Z = T_B - T_T$).

7.3.1 General observations

The simulated displacement has been observed to be always negative with its magnitude influenced by the electrode length L_e .

Fig. 7.2 shows the simulations results of the absolute maximum displacement as a function of the slab length L_e .

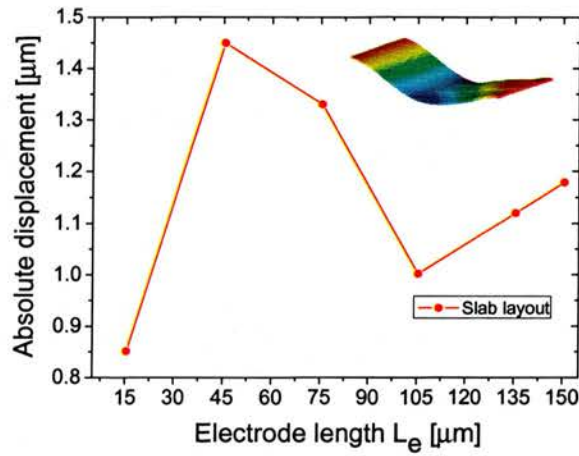


Figure 7.2: Simulations, slab layout: absolute maximum displacement for 150 μm long bridges actuated with the slab electrode layout (inset: snapshot with slab electrode length $L_e = 75 \mu\text{m}$).

A negative maximum displacement has been obtained for any value of the electrode length L_e (inset of Fig. 7.2). However, a deflection in the positive direction is observed on the part of the structure where the electrode overlaps the beam. Similar observations have been made for the u-shaped layout case in Chapter 6, Section 6.3.1, where the negative and positive deflections have been related to the vertical temperature difference ΔT_Z (single material thermal expansion effect) and to the difference between final and initial temperature ΔT (bimaterial thermal expansion effect).

As in the u-shaped case, in order to explain the negative sign of the maximum displace-

ment, the temperature experienced by the beam has been investigated. Fig. 7.3 shows ΔT (Fig. 7.3(a)) and ΔT_Z (Fig. 7.3(b)) generated with different slab lengths L_e .

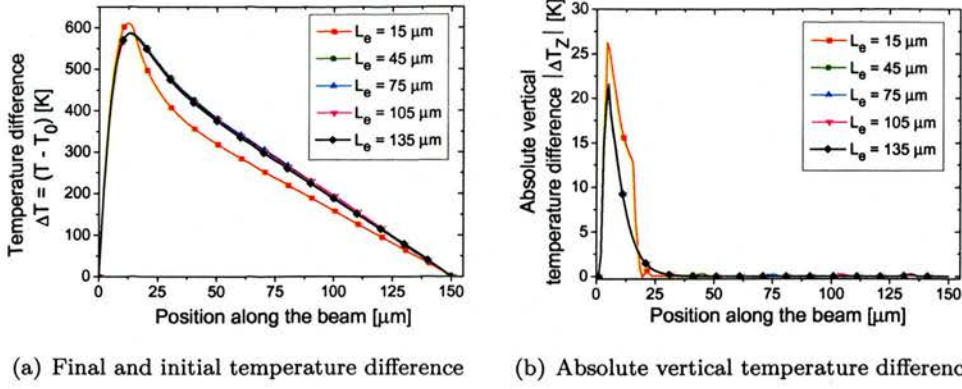


Figure 7.3: Simulations, slab layout: temperature data of 150 μm long bridges for different electrode lengths L_e .

It can be seen that the changes in the trend of ΔT and ΔT_Z are relatively small as the electrode length L_e is increased. Nevertheless, the constant presence of the vertical temperature gradient ΔT_Z suggests that the behaviour of the structure is dominated and influenced strongly by the single material thermal expansion effect. In addition, the overall downward deflection of the bridge is explained by the fact that ΔT_Z is relatively large and always present for any electrode lengths (see Chapter 6, Section 6.3.1).

7.3.2 Influence of the electrode length L_e on the bridge deflection

The influence of the electrode length L_e on the induced simulated displacement can be explained by observing the difference ΔT between final and initial temperature and the vertical temperature difference ΔT_Z generated by the slab electrode.

From Fig. 7.3(a), the trend of ΔT along the beam has been shown to be very similar for all the different electrode lengths L_e observing a relatively small variation only when L_e is increased from 15 to 45 μm. For $L_e > 45$ μm, the values of ΔT along the beam are the same for all the simulated electrode lengths. The curves of ΔT are seen to

increase to a maximum value of ~ 600 K at $15\ \mu\text{m}$ (1/10 of the beam length) and then to decrease to 0 K towards anchor 2.

As for the vertical temperature difference, shown in Fig. 7.3(b), the slab configuration generates a relatively large ΔT_Z that is concentrated close to the root of the beam (position along the beam $< 30\ \mu\text{m}$) due to the path of the current flowing through the electrode. In addition, ΔT_Z arises in the same location and do not decrease despite the increase of the electrode length. As mentioned above, the conditions for negative displacement in Eq. 3.9 are satisfied for any electrode lengths L_e (see also Chapter 6, Section 6.3.1).

The trend of the curves for ΔT and ΔT_Z is not affected strongly when the length of the electrode is increased, however changes in the magnitude of the simulated displacements are observed as the electrode length L_e is increased. It is believed that the changes in the absolute maximum displacement are due mainly to the increase of the electrode area as L_e increases. As a matter of fact, as the slab moves towards anchor 2, the bimaterial area increases hence increasing the influence of the bimaterial thermal expansion effect on the deflection of the bridge.

From Fig. 7.2, as L_e increases from 15 to $45\ \mu\text{m}$, the simulated absolute displacement is observed to increase to its maximum probably due to the increase of the area, where the vertical temperature gradient influences, from 20 to $30\ \mu\text{m}$ (Fig. 7.3(b)). However, when $L_e > 45\ \mu\text{m}$, the increase in the electrode area induces a larger bimaterial thermal expansion of the structure (i.e. positive displacement) opposite to the single material expansion (i.e. negative displacement) generated by the vertical temperature gradient, hence the magnitude of the overall displacement is observed to decrease. For $L_e > 105\ \mu\text{m}$, the further increase in the electrode area no longer dominates since the force exerted on the beam is damped by the reaction force exerted by anchor 2 (Fig. 7.1). Under these conditions, the absolute displacement is observed to increase slightly.

7.4 Measurements: the slab electrode

The Al/SiC bridges with the slab electrodes have been fabricated as described in Chapter 4. The resonance of the fabricated devices has been investigated by electro-thermal actuation with the same methodology used in Chapter 6, Section 6.4. Once, the resonance of the devices has been detected, the applied frequency has been set at the exact value of the structures' resonant frequency ($f_{in} = f_{res}$) so that the amplitude of the vibration at resonance could be investigated.

The inspection of the resonant frequency of the $150\text{ }\mu\text{m}$ long bridges has been focused in a range $\pm 300\text{ kHz}$ around the simulated value of 1.263 MHz . However, in the measurements, frequencies in the range $1 - 1.1\text{ MHz}$ have been obtained. The measured values are lower than the simulated ones probably due to an overestimation of the magnitude of the SiC tensile stress that has been included in the simulations. Fig. 7.4 shows one of the detected resonant peak with a Q factor ≈ 7500 .

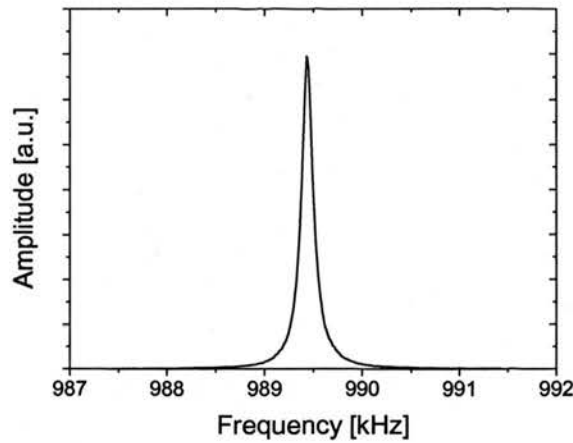


Figure 7.4: Measurements, slab layout: resonant peak of an Al/SiC bridge resonator $150\text{ }\mu\text{m}$ long actuated electro-thermally with a slab electrode.

Fig. 7.5 shows the measurements results as a function of the slab electrode length L_e . The detected amplitudes are in a range $80 - 150\text{ nm}$ showing to increase to a maximum value as L_e increases from 15 to $105\text{ }\mu\text{m}$. A further increase of L_e to $150\text{ }\mu\text{m}$ (i.e.

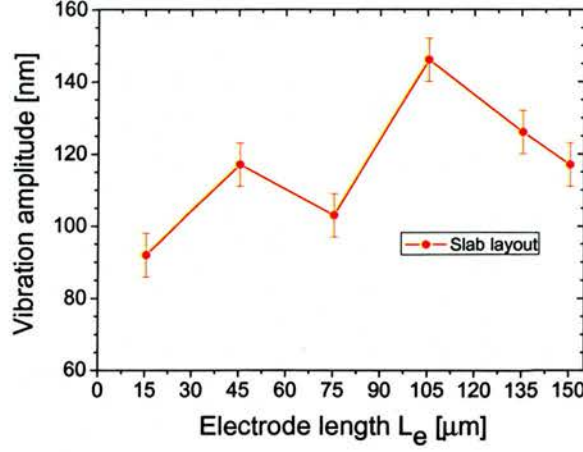


Figure 7.5: Measurements, slab layout: vibration amplitude as a function of electrode length L_e for 150 μm long bridges actuated with the slab electrode layout.

slab shifting towards anchor 2) causes the amplitude to decrease. As observed in the previous section, a consequence of the increase in the slab length is the increase of the area where ΔT_Z influences (increase of the single material thermal expansion effect) hence inducing a larger deflection of the structure. After a certain value of L_e (105 μm in the measured devices) the bimaterial thermal expansion effect starts to counterbalance the single material one resulting in a decrease of the absolute displacement.

In the simulations, the trend of the displacement is slightly different and the maximum vibration amplitude is reached at $L_e = 45 \mu\text{m}$. Probably, the discrepancies between simulations and measurements are due to the presence of undercut at the anchors of the fabricated bridges. As a consequence, the relative beam length L_b is longer hence shifting the maximum values of the measured vibration amplitudes to longer electrode lengths. In addition, the measured values differ by an order of magnitude to the simulated ones. As mentioned in the previous chapter, the temperature generated in the measured devices is lower than in the simulations thus resulting in a lower induced vibration amplitude. Furthermore, in the measurement system, the low reflectivity of the SiC influences the magnitude of the signal output so that the detected vibration amplitude is diminished to lower values.

7.5 Simulations: comparison between slab and u-shaped electrodes

In this section, in order to determine the best design strategy for the most efficient actuation layout, the slab and the u-shaped electrode architecture are compared. The simulated induced displacements and temperatures have been analysed.

For the u-shaped electrode design (Chapter 6, Fig. 6.1), the width W and the spacing S have been fixed at 6 and 28 μm , respectively, while the length L_e has been varied in the range 15 - 150 μm as in the slab study presented in Section 7.3. The beam dimensions L_b and W_b have been fixed at 150 and 60 μm , respectively, as for the slab simulations. The value of the width and spacing of the u-shaped electrode have been chosen so that the covered perimeter is comparable to the one covered by the slab electrode.

Fig. 7.6 shows the simulated absolute displacement obtained for the u-shaped and slab layouts.

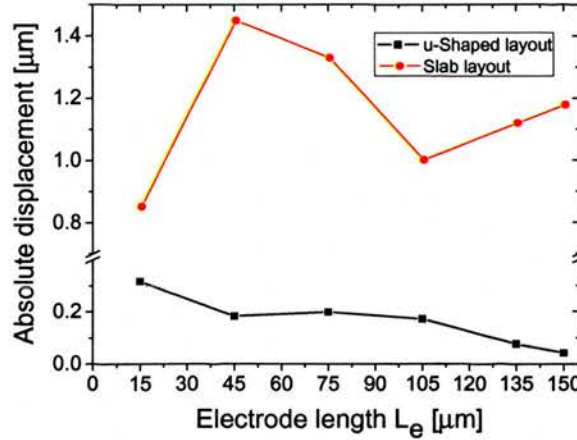


Figure 7.6: Simulations, slab and u-shaped layouts: maximum displacement as a function of the electrode length L_e for 150 μm long bridges.

In the u-shaped case, the effect of the SiC internal stress included in the simulations is observed as smaller displacement variations as a function of L_e compared to the case

when the stress is not considered (Chapter 6, Section 6.3).

Moreover, from Fig. 7.6, it is possible to observe that higher absolute displacements can be induced by actuating the Al/SiC bridges with the slab electrode configuration. This result can be explained by comparing the temperature generated by the two different electrode architectures.

The difference between final and initial temperature ΔT and the vertical temperature difference ΔT_z obtained from the simulations of the u-shaped electrode have been plotted in Fig. 7.7(a) and Fig. 7.7(b), respectively. In addition, for facilitating the comparison, the temperature graphs plotted in Fig. 7.3 for the slab layout have been included in Fig. 7.7(c) and Fig. 7.7(d).

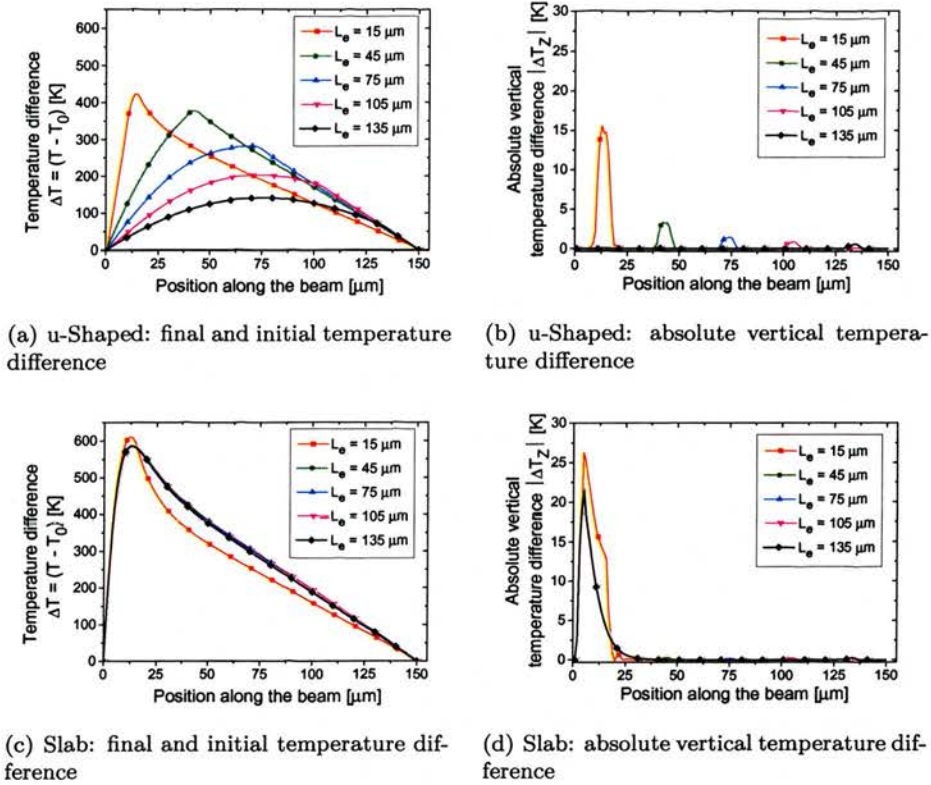


Figure 7.7: Simulations, slab and u-shaped layouts: temperature data of 150 μm long bridges for different electrode lengths L_e .

At first glance, it is possible to notice that the slab electrode generates higher temperature gradients compared to the u-shaped one. Both configurations are influenced by ΔT and ΔT_Z , nevertheless the interaction between single material and bimaterial thermal expansion effects is different depending on the considered architecture. In the u-shaped case, as the electrode length L_e increases, ΔT_Z disappears and ΔT distributes more uniformly along the beam. As discussed in Chapter 6, Section 6.3, the decrease of ΔT_Z involves a decrease of the single material thermal expansion effect while the more uniform distribution of ΔT involves an increase in the bimaterial thermal expansion effect. These two competing effects appear to have the same magnitude hence the absolute value of the displacement decreases. On the contrary, in the slab layout both ΔT_Z and ΔT are relatively large and no major changes are observed as a function of L_e . In this case, the single material thermal expansion effect is always present and is greater than the bimaterial thermal expansion effect hence dominating the overall magnitude of the displacement. The slab electrode generates a higher vertical temperature difference compared to the u-shaped electrode so that the induced simulated displacement is larger.

7.6 Measurements: comparison between slab and u-shaped electrodes

The devices with u-shaped electrodes fabricated with the same dimensions as in the simulations have been tested. The vibration amplitudes measured at resonance have been compared with the ones measured for the bridges having slab electrodes. Fig. 7.8 shows the measurement results as a function of the electrode length L_e for both architectures. The u-shaped electrode induces vibration amplitudes in the range 10 - 60 nm while the slab generates higher amplitudes in the range 80 - 150 nm. The largest difference in the measured amplitude is observed when $L_e = 105 \mu\text{m}$. In agreement with the simulations, the slab layout forces larger deflections compared to the u-shaped

architecture due to the relatively large vertical temperature gradient localised at the root of the beam.

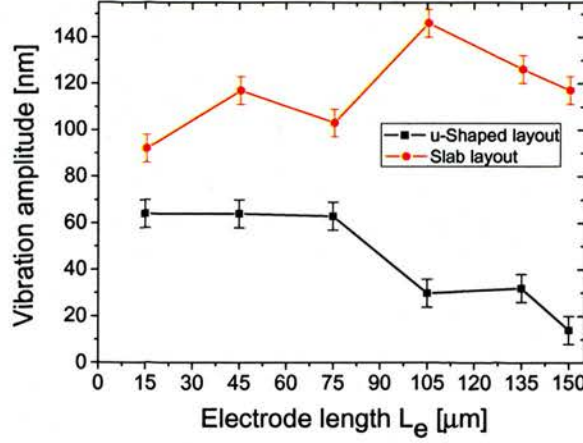


Figure 7.8: Measurements, slab and u-shaped layouts: vibration amplitude as a function of the electrode length L_e for 150 μm long bridges.

In the u-shaped configuration, the measured vibration amplitude is constant for $15 \mu\text{m} \leq L_e \leq 75 \mu\text{m}$ and decreases as the electrode length L_e is increased from 75 to 150 μm . For the slab configuration, the measured amplitude increases to a maximum value as L_e increases from 15 to 105 μm . Then, a further increase of the slab length towards anchor 2 (Fig. 7.1) causes the amplitude to decrease.

7.7 Conclusions

In this chapter, the possibility of maximising the efficiency of the electro-thermal actuation of bimaterial Al/SiC bridges by using a slab electrode configuration has been explored. The electro-thermo-mechanical transduction has been investigated as a function of the electrode length with simulations and measurements on the fabricated devices.

From the simulations, the bridge implemented with a slab layout has shown to behave at the same time as a single material and a bimaterial structure. As discussed in the previous chapter, the single material behaviour is related to the vertical temperature

difference and induces downwards deflections while the bimaterial behaviour is related to the difference between final and initial temperature and induces upwards deflections.

For the Al/SiC bridges with slab electrodes, a negative maximum displacement has been obtained for all the electrode lengths considered. This result is due to the vertical temperature difference that has been observed to be always present and located at the root of the beam regardless the electrode length.

The simulated absolute displacement is seen to be influenced by the electrode length. As the slab length increases, the absolute displacement is observed first to increase and then to decrease. The maximum value of the displacement is reached when the electrode covers $\frac{1}{3}$ of the beam length. When the electrode length increases, the electrode area increases thus enhancing the bimaterial thermal expansion effect. With the increase of the electrode area, the single material thermal expansion effect is counterbalanced by the increasing bimaterial thermal expansion effect resulting in a decrease of the absolute displacement.

The Al/SiC bridges fabricated with the slab electrodes have been actuated electro-thermally and the vibration amplitude at resonance has been measured. Similar to the simulations, as the slab length increases the detected amplitudes have been observed first to increase and then to decrease. In the measurements, the maximum vibration amplitude is obtained when the slab covers $\frac{2}{3}$ of the beam length. The discrepancies between simulations and measurements are associated probably to the longer dimension of the fabricated beams consequence of the undercut at the anchors.

In order to select the most efficient electrode design, the slab architecture has been compared with the u-shaped one by studying the simulated displacement and observing the differences in the temperature distribution along the beam. From the simulations, the slab configuration has been shown to induce deflection magnitudes higher than the u-shaped one due to the larger temperature gradients generated. The better performance of the slab layout has been confirmed with the measurements on the fabricated devices.

As a matter of fact, higher vibration amplitudes have been measured for the devices actuated with slab electrodes.

The results presented can be used for the optimisation of the design of Al/SiC bridge resonators. In particular, as discussed in Chapter 6, the ability of inducing large deflections by positioning the electrodes close to the root of the beam gives the possibility of designing additional sensing electrodes on the other side of the beam.

Chapter 8

Study of the mechanical behaviour and electro-thermal actuation of SiC ring resonators

8.1 Introduction

As discussed in Chapter 2, the resonant frequency range at which MEMS devices operate is of key relevance for the application considered. In the previous chapters, single and double clamped MEMS resonators have been shown to resonate in a frequency range from few hundreds of Hz to few MHz. However, for high frequency (HF) or radio frequency (RF) applications, higher resonant frequencies are needed. Chapters 6 and 7 have focused on the optimisation of the electrode design in order to maximise the actuation efficiency. In this chapter, the attention is focused on the possibility of increasing the resonant frequency range.

The analytical formulas for the resonant frequency of beams and disks have been presented in Chapter 3. It has been shown that disks can resonate at higher frequencies compared to double or single clamped beams resonators. However, as opposed to beam

resonators, the modal behaviour of circular structures has not been studied deeply in the literature. Circular membrane resonators have been considered and studied with the aim of increasing the resonant frequency range.

In particular, the investigated structures are circular membranes with a circular hole patterned in the centre (i.e. rings). The design, simulations and testing of single material SiC and bimaterial Al/SiC ring resonators is presented. The fabrication process used for fabricating the SiC ring resonators, described in Chapter 4, implies the patterning of a hole in the centre of the structure. The fabricated structures differ from simple plain disks hence the modal behaviour is not predictable with the analytical formula obtained by solving the wave equation. Therefore, the single material SiC rings have been simulated with FEM analysis for the purpose of studying the dependence of the resonant frequency on the radius dimension and hole size.

FEM simulations have been used also to investigate the possibility of actuating electro-thermally the bimaterial Al/SiC rings with three different Al electrodes configurations. In addition, the degree of deflection induced by the different electrode layouts has been observed with the aim of assessing the most efficient configuration.

The resonant frequency of the fabricated single material SiC rings have been investigated by actuating the structures mechanically. The frequency values obtained have been discussed and compared with the simulated ones. Furthermore, the bimaterial Al/SiC rings have been fabricated implementing the same electrode configurations that have been analysed in the simulations. The fabricated Al/SiC rings have been actuated electro-thermally to obtain out-of-plane deflections. The vibration amplitude at resonance induced with the three electrode layouts has been measured and compared.

8.2 Resonator and electrodes design

The design of the simulated SiC ring structures and top Al electrodes is described.

Fig. 8.1 shows the schematic of the simulated single material SiC ring resonators. The thickness t has been fixed at $2\ \mu\text{m}$, the ring radius R varied in a range between 20 and $200\ \mu\text{m}$ and the hole radius h increased from $0\ \mu\text{m}$ (plain disk) to 6 and $15\ \mu\text{m}$. With the considered dimensional variations, the dependence of the resonant frequency on the ring and hole radius has been studied.

In addition, bimaterial Al/SiC rings have been designed to examine the feasibility of actuating electro-thermally the rings. Al electrodes with single u-shaped (see Chapter 6), double u-shaped and inter-digitated (IDT) configurations have been considered for this study. Fig. 8.2 shows the schematic of the three different electrode layouts that have been designed on top of the SiC rings.

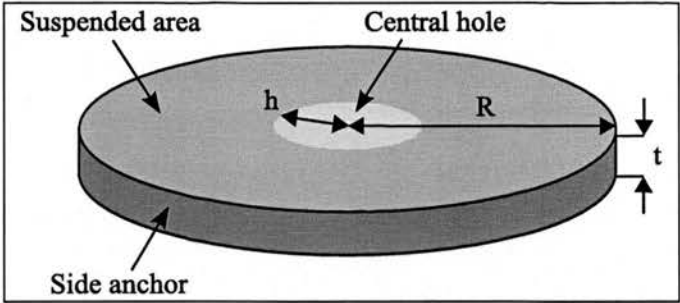


Figure 8.1: Schematic of the designed SiC rings.

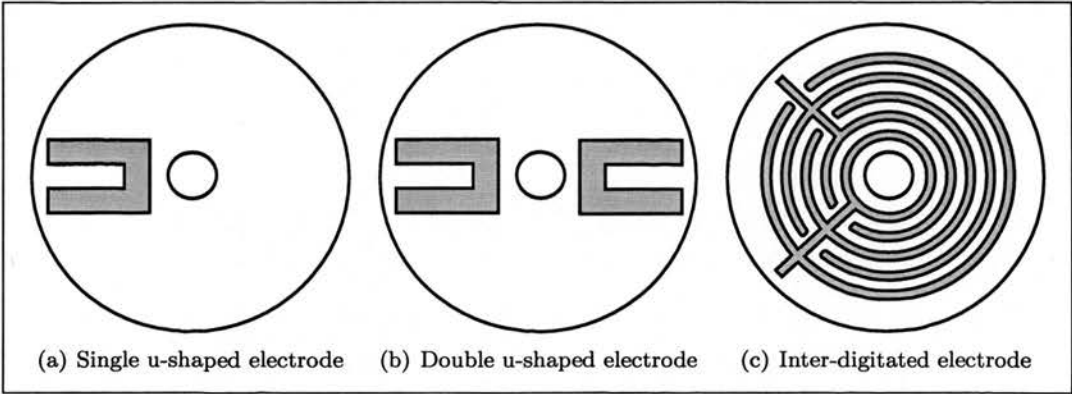


Figure 8.2: Schematic of the designed electrodes on SiC rings.

8.3 Simulations: mechanical behaviour

In this section, the simulated mechanical behaviour of the SiC rings is presented. The results are discussed focusing on the resonant frequency and its dependence on the ring radius R and hole radius h . The structures have been simulated by fixing the side of the ring as an anchor and inducing out-of-plane deflections. The simulations have been performed with *CoventorWare* (version 2004) and the mesh type and size has been optimised to obtained relatively accurate results in a reasonable computational time (see Chapter 6). In the case of rings, an extruded bricks mesh created with a pave-type algorithm has been used obtaining ~ 8000 elements.

When actuated in the vertical direction, the simulated rings have the same first mode shape as disk structures. Fig. 8.3 shows a snapshot obtained from the mechanical simulation of the first mode of a SiC ring with $R = 80 \mu\text{m}$ and $h = 6 \mu\text{m}$.

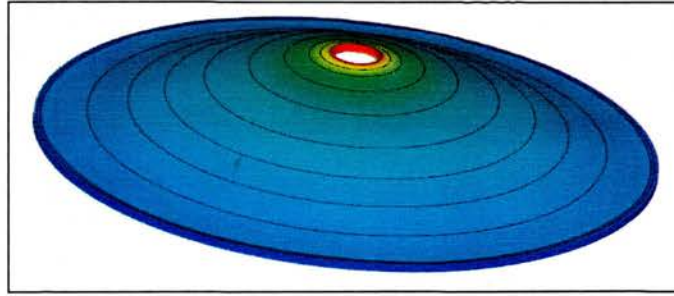


Figure 8.3: Simulations: snapshot of the first mode shape for a SiC ring with $R = 80 \mu\text{m}$ and $h = 6 \mu\text{m}$.

Fig. 8.4 shows the obtained resonant frequency plotted as a function of the ring radius R for hole radius $h = 0, 6, 15 \mu\text{m}$. The resonant frequency is seen to increase when R decreases achieving values up to 30 MHz for $R = 20 \mu\text{m}$ and $h = 6 \mu\text{m}$. Frequencies higher than 30 MHz have been obtained for smaller rings (up to ≈ 148 MHz with $R = 20 \mu\text{m}$ and $h = 15 \mu\text{m}$). The quadratic dependence of the frequency on the radius length R is in good agreement with the analytical formula reported for disk structures (see Eq. 3.7 in Chapter 3, Section 3.2). When $R > 80 \mu\text{m}$, the resonant frequency

values obtained for the different hole sizes remain constant while for $R \leq 80 \mu\text{m}$, the resonant frequencies obtained for $h = 15 \mu\text{m}$ (i.e. narrow ring size) are observed to be higher than those obtained for $h = 0$ and $6 \mu\text{m}$ (i.e. wide ring size).

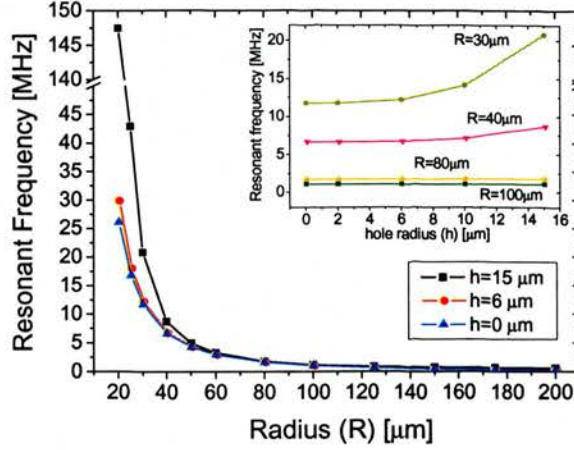


Figure 8.4: Simulations: results for the resonant frequency of SiC ring resonators as a function of the ring radius R for different hole radius h (inset: resonant frequency as a function of the hole radius for different R).

In order to observe in detail the influence of the central hole on the modal behaviour of the structure, the resonant frequency as a function of the hole radius h for ring radius $R = 30, 40, 80, 100 \mu\text{m}$ has been plotted in the inset of Fig. 8.4. It can be seen that for $R > 80 \mu\text{m}$ the resonant frequency remains constant despite the increase in the hole size. On the contrary, for $R \leq 80 \mu\text{m}$, the resonant frequency is observed to increase as h increases from 6 to 15 μm , more so for smaller R . The impact of the size of the central hole h on the resonant frequency becomes more evident as R decreases (i.e. as the width of the ring becomes smaller). As expected from the comparison between the analytical formulas for the resonant frequency of beams and disks (see Eq. 3.5, Eq. 3.6 and Eq. 3.7 in Chapter 3, Section 3.2), the simulated SiC rings resonate at higher natural frequencies compared to beam resonators with similar dimensions.

8.4 Simulations: electro-thermal behaviour

The possibility of exciting the rings electro-thermally has been investigated with the use of FEM simulations. On top of the SiC rings, Al electrodes have been designed with single, double and inter-digitated configurations. The influence of the electrode architecture on the induced displacement and on the amount of deflected area has been analysed. The side of the ring has been fixed as an anchor and its temperature set at 300 K as a thermal boundary condition. Under these conditions, the side of the simulated ring correspond to the clamped side of the fabricated structures and it is connected to the substrate that acts as heat sink (fixed at room temperature in the measurements). The actuation of the SiC rings has been simulated by applying a DC voltage of 1 V across the top electrodes.

From the simulations, the maximum displacement has been observed to be always on the part of the ring where the electrodes lie. In this area, the mechanical stress and displacement are higher compared to the other parts of the structure due to the heating effect of the electrodes and to the difference in the TCEs of the two materials. However, the magnitude of the displacement and the amount of deflected area depend on the different electrode configuration. In general, the single electrode has shown to induce a higher displacement compared to the double electrode and the IDT electrode. The lowest displacement is induced by the IDT architecture. The difference in the induced magnitudes of displacement can be explained by observing the simulated temperature induced by the electrodes. Fig. 8.5 shows the snapshots of the simulated temperature distribution on the Al/SiC rings ($R = 100 \mu\text{m}$ and $h = 6 \mu\text{m}$) obtained with the different electrode configurations. It has been found that the average temperature generated by the single (570 K) and double (505 K) electrode configuration is much higher than the one obtained with the IDT electrode (310 K). Furthermore, if the temperature is considered along with the heated up area, the double electrode configuration is found to be the most efficient design showing a relatively high average temperature and the

largest heated up area, hence inducing a large and uniform deflection of the structure.

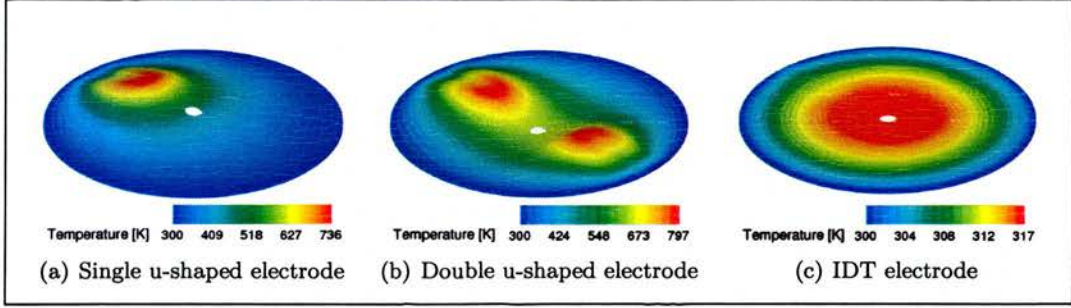


Figure 8.5: Simulations: snapshots with temperature distribution for rings with $R = 100 \mu\text{m}$ and $h = 6 \mu\text{m}$.

8.5 Measurements: mechanical actuation

Single material SiC ring resonators have been fabricated with different ring radius R and hole radius h as described in Chapter 4, Section 4.6. In this section, the mechanical actuation of the fabricated resonators is discussed together with the measurement of the resonant frequency. The results obtained from the measurements are presented and compared with the simulations.

The SiC rings fabricated having $30 \mu\text{m} < R < 200 \mu\text{m}$ and hole radius $h = 6, 10, 15 \mu\text{m}$ have been actuated mechanically with the use of a piezo-electric disc. The resonant frequency has been detected optically with the same measurement setup presented in Chapter 5, Section 5.4. Resonant frequencies up to 3.5 MHz could be investigated due to the limitation of the optical vibrometer used.

Fig. 8.6 shows the measured and simulated resonant frequency as a function of the radius R for the mechanically actuated SiC ring structures with $h = 6$ and $15 \mu\text{m}$. It can be seen that in general, the measured values are higher than the simulated ones. It is well known that the presence of stress in the structures results in an increase of the resonant frequency. In the design, the internal stress is not relieved through the side of the structure, as in a beam design, but only through the central hole that has a

relatively small size compared to the entire structure. This can result in a large stress within the fabricated ring resonators. However, the quadratic trend observed in the measured values and the higher resonant frequencies measured for rings with a larger hole are in good agreement with the simulations results. Furthermore, it can be seen that the effect of a larger hole size ($15\ \mu\text{m}$) serves to increase the measured resonant frequency further at $R < 120\ \mu\text{m}$ (i.e. smaller rings). In the simulations, the onset for the increase in the resonant frequency, as a result of larger h , is observed at smaller R ($< 80\ \mu\text{m}$). This observation could be attributed to the presence of stress in the fabricated devices.

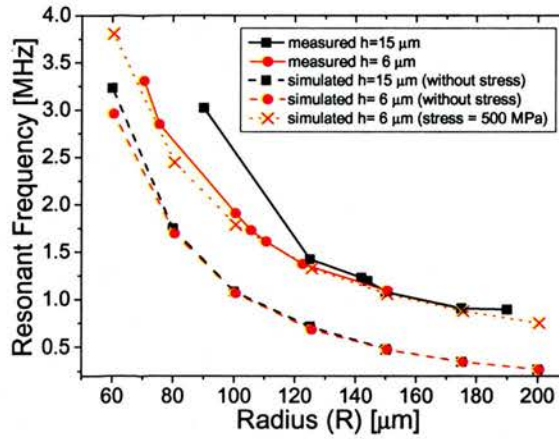


Figure 8.6: Ring resonators: measured and simulated resonant frequency as a function of the ring radius R for hole radius $h = 6$ and $15\ \mu\text{m}$.

In order to confirm the effect of the internal stress on the fabricated SiC rings, additional parametric simulations have been performed as a function of the stress and a value of 500 MPa has been obtained as the best fitting parameter. The resonant frequencies simulated for rings with $h = 6\ \mu\text{m}$ and including the effect of the stress in the SiC layer have been plotted as a function of the radius R in Fig. 8.6 (dotted line).

8.6 Measurements: electro-thermal actuation

In addition to the single material SiC structures, bimaterial Al/SiC ring resonators have been fabricated and actuated electro-thermally. As in the structures studied in the simulations and presented in Section 8.4, the Al has been used to implement top electrodes having single u-shaped, double u-shaped and IDT configurations. The Al/SiC rings have been fabricated using the process described in Chapter 4, Section 4.6. The resonant frequency has been investigated together with the vibration amplitude at resonance when actuating electro-thermally. For these measurements, the same setup presented in Chapter 6, Section 6.4 has been used.

Electro-thermal actuation has been performed by applying an input voltage across the top electrodes with a similar configuration as the electro-thermal actuation of Al/SiC bridges (see Fig. 6.1 in Chapter 6). The AC amplitude V_{ac} and the DC bias V_{dc} have been set equal to 6 V and 2 V, respectively. The input frequency (f_{in}) has been varied in a range ± 500 kHz around the resonant frequency values detected when actuating the rings mechanically. The rings have been driven into resonance successfully using the three different electrode configurations.

Fig. 8.7 shows one of the resonant peaks measured at ≈ 1.43 MHz ($Q \approx 12000$) for a ring with $R = 125 \mu\text{m}$ and $h = 15 \mu\text{m}$ actuated electro thermally with a single electrode configuration. The tested devices have shown Q factors in the range 10000 - 12000. These values are higher than the ones reported in the literature for out-of-plane vertical resonators, ≈ 1000 for Si beam resonators [112] and ≈ 10000 for SiC beam resonators [51].

The resonant frequencies detected when actuating the structures electro-thermally are $\approx 2 - 3$ kHz lower than the ones measured when actuating mechanically. This is probably due to the increase of temperature experienced by the structure when the actuation voltage is applied. This temperature increase induces a thermal compressive stress and leads to a decrease of the Young's modulus of the material forming the

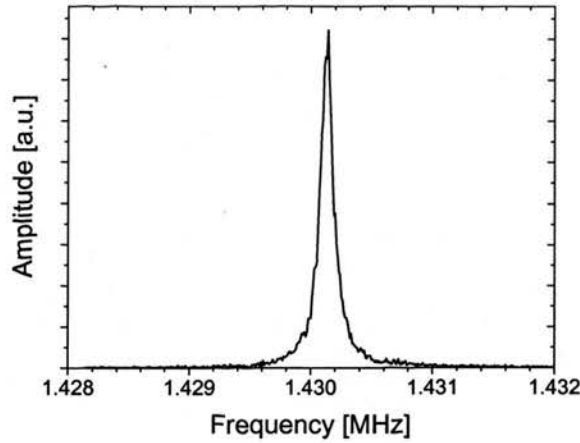


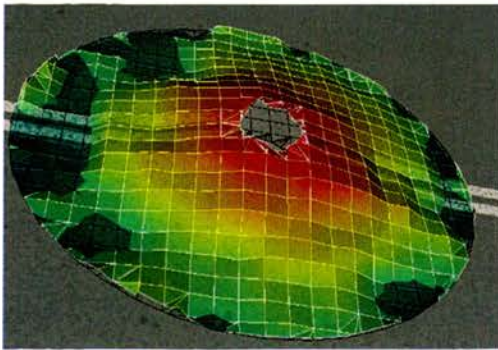
Figure 8.7: Ring resonators: resonant peak of an Al/SiC bimaterial ring with radius $R = 125 \mu\text{m}$ and hole radius $h = 15 \mu\text{m}$ ($Q \approx 12000$).

resonator [53] [113]. From the equations presented for the resonant frequency of flexural-mode resonators in Chapter 3, Section 3.2, a decrease in the Young's modulus leads to a decrease in the frequency while the presence of tensile stress leads to an increase of the resonant frequency. Therefore, it is believed that in the fabricated structures the decrease in the Young's modulus has a greater influence than the increase in the tensile stress thus the resonant frequency is found to decrease.

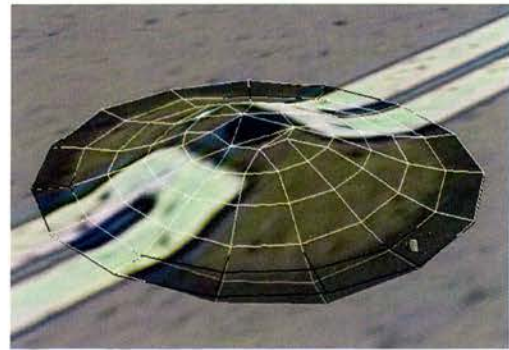
The vibration amplitude of a ring with $R = 190 \mu\text{m}$ and $h = 15 \mu\text{m}$ has been investigated when actuating with the single, double and IDT electrode designs. The amplitude has been measured on a circular trajectory with a radius equal to $R/2$. In the single electrode case, the amplitude has been measured to be $\sim 460 \text{ nm}$ on top of the Al and $\sim 180 \text{ nm}$ on the part of the ring not covered by the electrode. On the contrary, constant vibration amplitude of 460 nm and 10 nm has been detected on the measuring circumference when actuating with the double and IDT electrodes, respectively.

A further confirmation of the higher actuation efficiency achievable with the double electrode configuration has been given when testing the devices at atmospheric pressure. Some of the fabricated Al/SiC bimaterial rings have been actuated electro-thermally without the use of a vacuum chamber. Under these conditions, only the resonant

frequency of rings having a double electrode layout could be detected showing that this configuration can induce detectable vibration amplitudes at atmospheric pressure. Fig. 8.8 shows the measurement snapshots obtained for two of the fabricated rings actuated electro-thermally with a double u-shaped electrodes and at atmospheric pressure. The resonance of the ring with $R = 195 \mu\text{m}$ and $h = 15 \mu\text{m}$ has been measured at 888 kHz with a Polytec multipoint vibrometer (Fig. 8.8(a)). The ring with $R = 46 \mu\text{m}$ and $h = 6 \mu\text{m}$ has been tested with a Polytec UHF vibrometer showing a resonant frequency of 7.79 MHz (Fig. 8.8(b)).



(a) Multipoint vibrometer measurement; ring dimensions: $R = 195 \mu\text{m}$ $h = 15 \mu\text{m}$; resonant frequency = 888 kHz



(b) UHF vibrometer measurement; ring dimensions: $R = 46 \mu\text{m}$ $h = 6 \mu\text{m}$; resonant frequency 7.79 MHz

Figure 8.8: Measurements: snapshots of bimaterial Al/SiC rings actuated electro-thermally with double electrode configuration at atmospheric pressure.

8.7 Conclusions

In this chapter, the implementation of SiC ring resonators has been discussed for exploring the possibility of achieving frequencies suitable for HF and RF applications. Out-of-plane deflections have been simulated and the resonant frequency has been studied. In addition, the possibility of actuating electro-thermally the SiC rings with top Al electrodes has been investigated. The single material SiC and bimaterial Al/SiC ring structures have been fabricated as presented in Chapter 4. The fabricated devices have been actuated mechanically and electro-thermally. The results obtained from the

measurements performed on the fabricated devices have been discussed and compared with the results obtained from the simulations.

From the mechanical simulations, the SiC rings have been shown to resonate at frequencies up to 145 MHz. The simulated resonant frequency has been shown to increase quadratically as the ring radius decreases. One significant finding is that for rings having a radius below a certain threshold, the resonant frequency can be increased by increasing the size of the central hole (i.e. reducing the width of the ring).

The possibility of actuating electro-thermally the SiC rings by applying a voltage to top Al electrodes has been investigated with the use of electro-thermal simulations. Single u-shaped, double u-shaped and IDT electrode configurations have been studied. Deflections have been induced when actuating with any of the three electrode layouts thus showing that the bimaterial Al/SiC are suitable for electro-thermal excitation. The best compromise between induced displacement and amount of deflected area has been obtained with the double u-shaped electrode design.

The fabricated devices have been actuated mechanically in order to confirm the functionality of the SiC rings. When actuating mechanically, resonant frequencies up to 3.3 MHz have been detected optically with a laser vibrometer capable of measuring frequencies up to 3.5 MHz. In good agreement with the simulations, the resonant frequency has been observed to increase quadratically with the decrease of the ring radius and to increase as the hole radius increases. The measured values have been observed to be higher than the simulated ones due to the presence of stress in the SiC. A tensile stress of 500 MPa could be deduced by comparing the measurements results with the simulated ones.

The fabricated Al/SiC rings have been driven into resonance successfully by electro-thermal actuation. Resonant frequencies up to 7.79 MHz have been detected and Q factors of ≈ 12000 have been obtained. The vibration amplitude at resonance induced by the single u-shaped, double u-shaped and IDT electrodes has been measured and

compared. The single and double u-shaped layouts have been shown to induce higher vibration amplitudes compared to the IDT architecture. In addition, the double u-shaped layout is capable of deflecting a larger area compared to the single u-shaped electrode.

In this chapter, SiC ring resonators have been shown to be feasible for operating at higher frequencies compared to beam resonators. Furthermore, the possibility of actuating electro-thermally bimaterial Al/SiC rings has been demonstrated.

Chapter 9

Electro-thermal mixing with bimaterial Al/SiC resonators

9.1 Introduction

In the previous chapters, the electro-thermal transduction mechanism on bimaterial Al/SiC structures has been studied. The electro-thermal actuation of SiC bridges and rings with top Al electrodes has been investigated with the use of FEM simulations and measurements performed on the devices fabricated as described in Chapter 4. The attention has been focused mainly on the influence of the electrode configuration and dimensions on the induced displacement and vibration amplitude. The electrode has been optimised in order to enhance the deflection of the structures. Ring structures have been shown to resonate at higher frequencies compared to beam resonators.

As discussed in Chapter 2, the resonators studied could find possible applications in electronic circuits as reference oscillators, filters and mixers. This chapter aims to extend the functionality of the designed resonators for performing frequency mixing functions with the use of electro-thermal transduction.

In the first part of the chapter, the mechanism of electro-thermal mixing is discussed

recalling the theory of electro-thermal transduction presented in Chapter 3.

In the second part, the measurements performed on the fabricated Al/SiC cantilevers and rings are presented and examined. First, the devices have been actuated electro-thermally by applying an input alternating voltage to the top Al electrodes. Then, the mixing function has been studied by investigating the resonance of the devices when two alternating voltages have been used for the actuation.

9.2 Electro-thermal actuation theory

In Chapter 3, the mechanism of electro-thermal transduction mechanism has been introduced and discussed in detail for bimaterial structures. In this section, the electro-thermal actuation theory has been recalled in order to extend the case of the actuation induced with one input voltage to the case of two input voltages applied.

A common case of a bimaterial device is constituted of a suspended structure with a top electrode that acts as a heater for the bottom material. When a voltage is applied to the electrode, an electric current is generated so that Joule heat occurs within the overall structure. Under these conditions, a temperature gradient is originated and a mechanical strain is experienced due to the thermal expansion of the materials and to the difference in the two materials' TCEs.

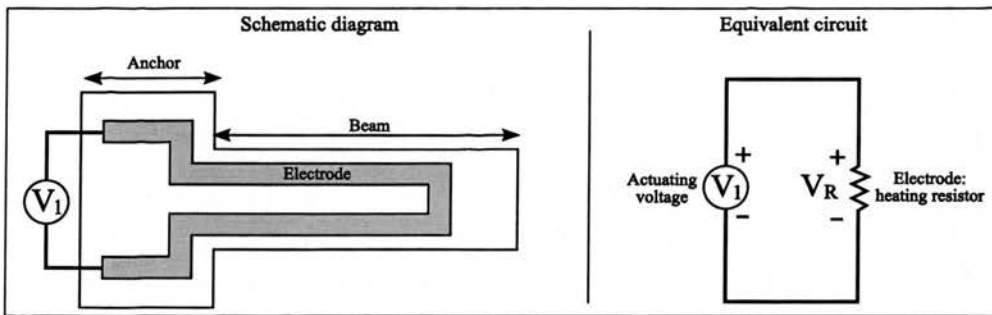


Figure 9.1: Schematic of a cantilever with one voltage applied to the top electrode.

9.2.1 Actuation with one voltage

In general, electro-thermal actuation is performed by applying one input voltage to the actuating electrode. Fig. 9.1 shows the schematic diagram and the electrical equivalent circuit for the case of an actuating voltage applied to the top electrode (also referred as heating resistor) of a suspended cantilever. If a constant voltage is applied, a steady deflection is generated. When applying an alternating voltage, the induced temperature oscillations give rise to vibrations of the overall structure. The driving force is proportional to the power dissipated in the heating resistor R . From Fig. 9.1, if the input signal is formed by an AC voltage superimposed to a DC bias $\mathbf{V}_1 = V_1 \sin \omega_1 t + V_{dc1}$, the power dissipated in R results (Eq. 3.12):

$$P = \frac{V_R^2}{R} = \frac{(V_1 \sin \omega_1 t + V_{dc1})^2}{R}. \quad (9.1)$$

From Eq. 9.1, if f_0 is the natural frequency of the structure and $f_1 = \omega_1/2\pi$ is the input frequency, resonance can be achieved when f_1 matches f_0 (see Chapter 3, Section 3.3.3). Under these conditions, the structure acts as a resonator performing a thermo-mechanical filtering of frequency components different from f_0 .

9.2.2 Actuation with two voltages

Now the case of two input voltages applied to the actuating electrode is explored. Fig. 9.2 shows a schematic diagram and the equivalent electrical circuit when applying two input signals to the top electrode of a suspended cantilever. In this case, the mechanical displacement of the structure is induced by the driving force generated by the two applied voltages. As in the case of one applied voltage, the driving force is proportional to the power dissipated in the heating resistor.

From Fig. 9.2, if the two input signals are two alternating voltages $\mathbf{V}_1 = V_1 \sin \omega_1 t + V_{dc1}$ and $\mathbf{V}_2 = V_2 \sin \omega_2 t + V_{dc2}$, the power dissipated in R equals:

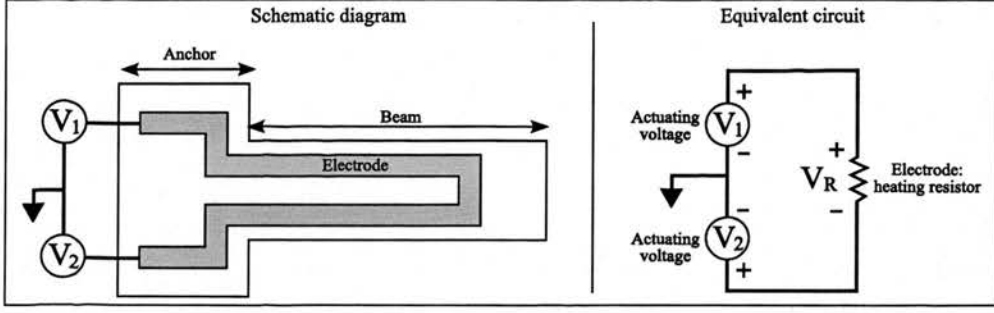


Figure 9.2: Schematic of a cantilever with two voltages applied to the top electrode.

$$P = \frac{V_R^2}{R} = \frac{(V_1 \sin \omega_1 t - V_2 \sin \omega_2 t + V_{dc})^2}{R}, \quad (9.2)$$

where $V_{dc} = V_{dc1} - V_{dc2}$.

Solving Eq. 9.2 and ignoring the terms with components multiple of ω_1 and ω_2 , the AC component of the power results:

$$P_{AC} \propto \frac{V_1 V_2 (\cos(\omega_1 + \omega_2)t - \cos(\omega_1 - \omega_2)t)}{R}. \quad (9.3)$$

Due to the quadratic dependence of the power on the applied voltage, the driving force is proportional to the components formed by the sum and the difference of the input angular frequencies ω_1 and ω_2 . Under these conditions, resonance will be achieved if the sum $(\omega_1 + \omega_2)/2\pi$ or the difference $(\omega_1 - \omega_2)/2\pi$ equals the natural frequency f_0 of the structure. In both cases, the resonator acts as a thermo-mechanical filter for frequency components not matching f_0 and as a mixer for frequencies which their sum or difference matching the beam resonance.

9.3 Measurements on cantilevers

In the previous section, electro-thermal mixing has been discussed theoretically. In this section, measurements have been performed on Al/SiC cantilevers fabricated with

the process flow described in Chapter 4. First, in order to measure the fundamental resonant frequency f_0 , the cantilevers have been actuated electro-thermally by applying one input signal. After, an additional input has been introduced to explore the ability of using two signals to induce the resonance of the structure. The measurements have been performed with the same setup and methodology described in Chapter 6, using a laser vibrometer to detect the resonance of the devices.

The electro-thermal mixing principle has been examined by testing bimaterial Al/SiC cantilevers with a length comprised between 50 and 200 μm and with an open-circuit electrode configuration. Fig. 9.3 shows one of the tested cantilevers with a length of 100 μm . The measurements have been performed by applying the actuating voltages to the top electrode as shown in the schematics in Fig. 9.1 (one input) and Fig. 9.2 (two inputs).

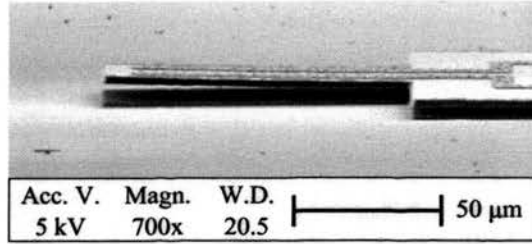


Figure 9.3: Scanning electron micrograph of one of the Al/SiC cantilevers used for the measurements.

When measuring the resonant frequency, a voltage $V_1 = V_1 \sin \omega_1 t + V_{dc1}$ has been applied with $V_1 = 4 \text{ V}$ and $V_{dc1} = 1 \text{ V}$. The fundamental frequency has been investigated by sweeping the input frequency f_1 and keeping the V_1 and V_{dc1} constant.

Once the cantilevers' ability to resonate has been confirmed and the resonant frequency f_0 detected, an additional input signal generator has been introduced. Two alternating voltages $V_1 = V_1 \sin \omega_1 t + V_{dc1}$ and $V_2 = V_1 \sin \omega_2 t + V_{dc2}$ have been applied with $V_1 = V_2 = 4 \text{ V}$, $V_{dc1} = V_{dc2} = 1 \text{ V}$, $f_1 = \omega_1/2\pi$ and $f_2 = \omega_2/2\pi$. The possibility of driving the structures into resonance has been explored using $f_1 + f_2 = f_0$ or $f_1 - f_2 = f_0$.

9.3.1 Sum

Solving Eq. 9.2, it has been shown that the frequencies of the two input signals can be thermo-mechanically added together if their sum matches the fundamental mechanical resonant frequency of the structure. As discussed above, first the resonant frequency of the cantilevers has been measured by actuating electro-thermally using one input voltage. Afterwards, the ability of inducing resonance by applying two input voltages has been investigated.

When applying two voltages, the input frequency f_1 has been fixed at a value $< f_0$ while the input frequency f_2 has been varied. Resonance has been detected successfully when $f_{sum} = f_1 + f_2 \approx f_0$.

Fig. 9.4 shows the resonant peaks detected for a $200\ \mu\text{m}$ long cantilever. In particular, Fig. 9.4(a) shows the resonant peak at $\sim 89\ \text{kHz}$ obtained when actuating with one input voltage. Fig. 9.4(b) shows the resonant peak obtained when applying two input voltages. The input frequencies $f_1 = 50\ \text{kHz}$ and $f_2 = 39.91\ \text{kHz}$ have been added and resonance has been obtained at $f_{sum} = 89.91\ \text{kHz}$.

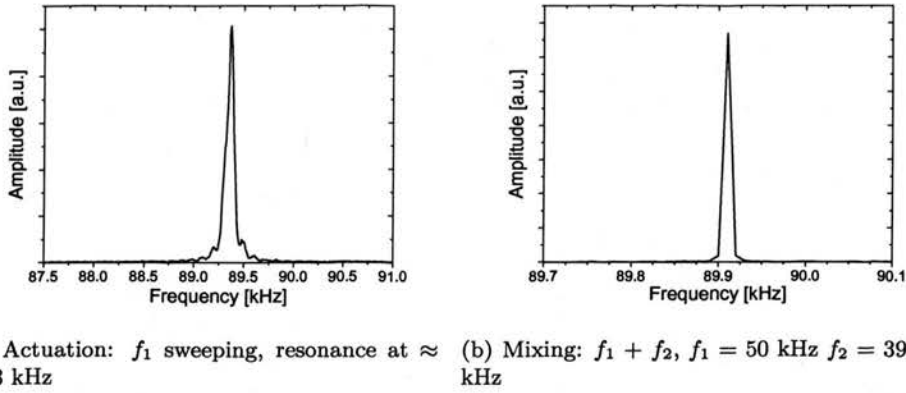


Figure 9.4: Measurements, actuation and mixing: resonant peaks for a $200\ \mu\text{m}$ Al/SiC cantilever.

9.3.2 Difference

From Eq. 9.3, the frequencies of the two input signals can be thermo-mechanically subtracted when their difference matches the fundamental frequency of the structure. As in the study of the frequency sum, first the devices have been actuated electro-thermally with one input voltage for detecting the resonant frequency. Then, two input voltages have been applied together.

The possibility of inducing resonance with the difference of the input frequencies has been investigated by fixing f_1 at a value $> f_0$ and sweeping f_2 . The resonance of the devices has been detected successfully when $f_{diff} = f_1 - f_2 \approx f_0$.

Fig. 9.5 shows the peaks measured for a $50 \mu\text{m}$ long cantilever. Fig. 9.5(a) shows the resonant peak at $\sim 944.5 \text{ kHz}$ obtained when actuating with one voltage. Fig. 9.5(b) shows the mixing peak obtained by subtracting thermo-mechanically $f_1 = 1200 \text{ kHz}$ and $f_2 = 255 \text{ kHz}$ so that $f_{diff} = f_1 - f_2 = 945 \text{ kHz}$.

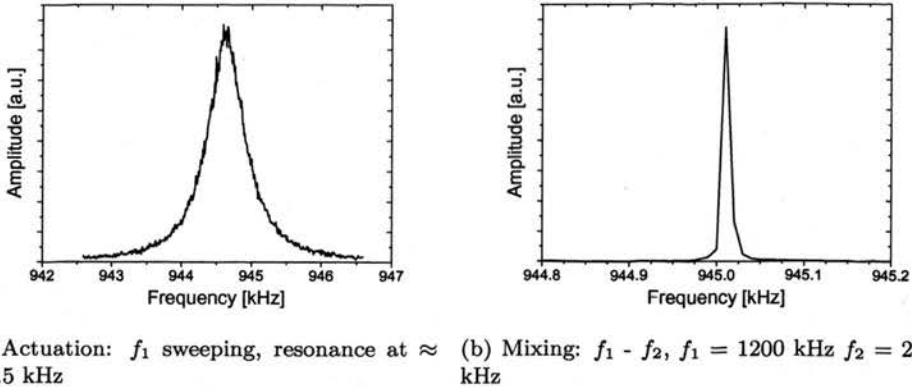


Figure 9.5: Measurements, actuation and mixing: resonant peaks for a $50 \mu\text{m}$ Al/SiC cantilever.

It is worth noting that resonance has been detected only when the sum or the difference between f_1 and f_2 is close to the resonant frequency f_0 measured when applying only one actuating signal. The cantilever achieves resonance by converting the electrical inputs into temperature fluctuations and then into mechanical vibrations, hence performing a

thermo-mechanical mix of the input frequencies directly within the bimaterial structure.

9.3.3 Mixing resonant frequencies - mechanical and thermal considerations

The frequency of the resonant peaks obtained when mixing two input signals are ~ 0.5 kHz higher compared to the ones obtained when applying only one input. In the mixing configuration (Fig. 9.2), if the DC amplitude is the same for V_1 and V_2 , the DC voltage drop across the heating electrode V_R is lower compared to actuation case with one voltage applied (Fig. 9.1). The temperature experienced by the structure is proportional to the power dissipated in the resistor. Consequently, the induced temperature within the beam in the mixing configuration is lower than in the actuating one. Under these conditions, the dimensional changes due to the thermal expansion can be reduced resulting in an effective smaller beam length. In addition, the Young's modulus could be slightly higher due to its inverse proportionality with the temperature [113]. Therefore, the increase of the resonant frequency observed is probably due to the smaller length and higher Young's modulus experienced when mixing (see Eq. 3.5 for the natural resonant frequency of cantilevers).

9.3.3.1 Thermal stress in cantilevers

It is important to highlight that the resonant frequency can be influenced by the variations of the structures' thermal stress arising from the temperature changes experienced by the cantilevers. In particular, the major contribution to the thermal stress σ_{th-C} in a bimaterial cantilever is determined by the difference in the TCEs of the materials forming the structure: $\sigma_{th-C} = \sigma_{SiC-Al}$, where σ_{SiC-Al} is the stress due to the difference between the TCEs of SiC (main structure) and Al (electrode). The degree of the total thermal stress σ_{th-C} can vary due to the dependence of σ_{SiC-Al} on the temperature. It is believed that the decrease in temperature leads to a decrease in

σ_{th-C} thus diminishing the resonant frequency of the devices.

The precise contribution of the change in geometry, Young's modulus and thermal stress on the resonant frequency is complex to evaluate and would require the measurement of temperature variations as a function of the actuating voltage. However, the increase in the resonant frequency observed is probably a consequence of the fact that the dimensional changes (i.e. smaller length) and the increase in the Young's modulus have a stronger influence than the decrease in the thermal stress. Therefore, the resonant frequency is observed to increase.

9.3.4 Vibration amplitude

A resonant peak has been obtained when the sum or the difference of the two input frequencies match the fundamental mechanical resonant frequency of the structure. In order to confirm the fact that mixing occurs only under these conditions, the frequency difference has been shifted from the resonant frequency and the magnitude of the vibration amplitude has been investigated.

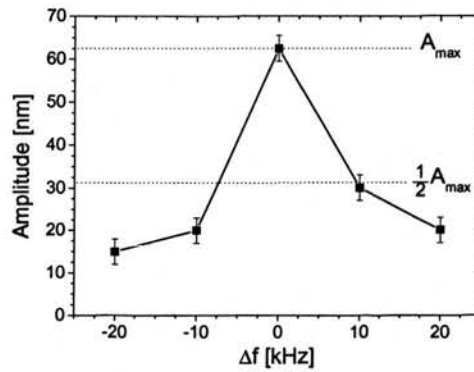


Figure 9.6: Measurements: mixing amplitude detected for a cantilever 50 μm long, $f_1 - f_2 \pm \Delta f$, $f_1 = 1200$ kHz $f_2 = 255$ kHz.

In order to shift $f_{diff} = f_1 - f_2$ from the natural frequency f_0 of the structure, the frequency of the second input signal f_2 has been varied by a factor $\pm \Delta f$. Fig. 9.6 shows the detected vibration amplitude for the 50 μm long cantilever as a function of

the frequency when Δf equals 0, 10 and 20 kHz. A maximum vibration amplitude A_{max} of 62 nm has been measured when $\Delta f = 0$. When Δf is increased to 10 kHz, the measured amplitude is lower than $\frac{1}{2}A_{max}$ and decreases as Δf increases to 20 kHz. Moreover, no vibrations have been detected for a further increase of Δf . In fact, when shifting from the natural frequency of the structure, resonance is no longer achieved and the amplitude of the vibration is observed to decrease [53].

9.4 Measurements on rings

In this section, the electro-thermo-mechanical mixing function is tested on Al/SiC rings resonators in order to confirm the functionality of this mechanism on different type of structures. As discussed in Chapter 8, ring structures offer the possibility of achieving higher resonant frequencies compared to beam architectures. The ability of mixing two input frequencies electro-thermally with ring resonators could contribute to the use of the studied mechanism for high frequency applications.

The measurements have been carried out on the SiC rings fabricated with top Al electrodes using the process flow described in Chapter 4, Section 4.6. The same measurement setup used for the cantilevers, described in detail in Chapter 6, has been utilised.

As for the tests performed on cantilevers, first, the resonant frequency has been measured by actuating the SiC rings electro-thermally with one input signal. Then, the mixing function has been investigated by connecting two input signals to the top electrode. In addition, the behaviour of the structures has been examined when varying the bias voltage of one of the input signals.

9.4.1 Actuation and mixing

Rings of different sizes have been measured in a frequency range between 500 kHz and 3 MHz. The results obtained from the actuation measurements have been shown to be consistent with the ones described in Chapter 8. After confirming the ability of inducing the resonance by electro-thermal actuation, resonant peaks have been detected successfully by applying two input signals with the sum or difference of their frequencies matching the fundamental frequency of the rings. Fig. 9.7 shows one of the tested devices.

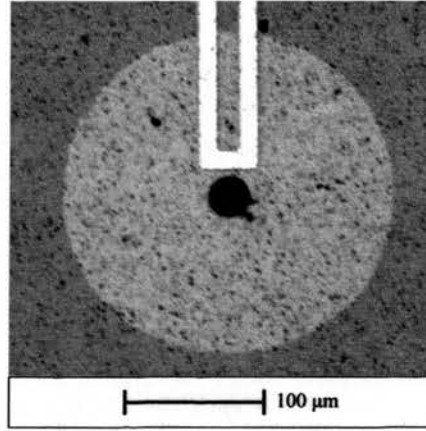


Figure 9.7: Optical micrograph of one of the Al/SiC rings used for the measurements.

As an example, Fig. 9.8 shows the resonant peaks obtained for an Al/SiC ring with a hole radius h and a ring radius R of 15 and 190 μm , respectively. Fig. 9.8(a) shows the peak at ~ 891 kHz (Q-factor ≈ 22300) measured when actuated electro-thermally by applying an AC voltage superimposed to a DC bias with amplitudes of $V_{pp} = 6$ V and $V_{dc} = 2$ V, respectively. Fig. 9.8(b) shows the resonant peak obtained by applying two input voltages V_1 and V_2 with $f_1 = 400$ kHz and f_2 sweeping in a range between 450 - 550 kHz. In this case, the DC amplitudes have been set at $V_{dc1} = 1.5$ V and $V_{dc2} = 2$ V while the AC amplitudes have been fixed at $V_{pp1} = V_{pp2} = 6$ V. The mixing resonant peak has been detected at $f_1 + f_2 = 892.6$ kHz that is approximately the measured frequency when actuating with one signal.

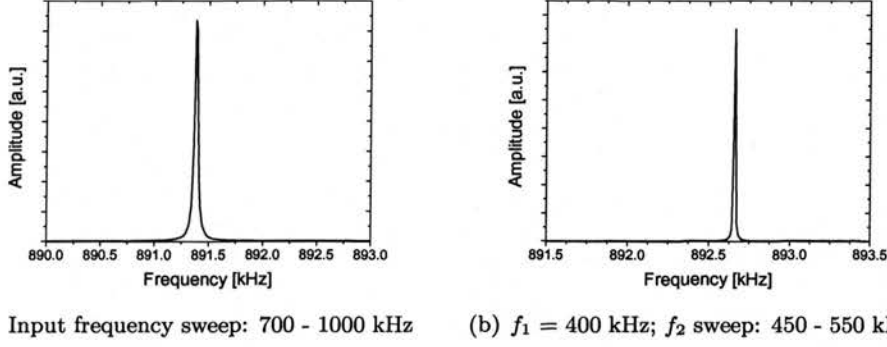


Figure 9.8: Measurements: actuation and mixing with a ring with $R = 190 \mu\text{m}$ $h = 15 \mu\text{m}$.

In general, similar to the results obtained for the cantilevers, the measured peaks obtained when performing the mixing tests have been shown to be higher than the ones measured for the standard electro-thermal actuation. As discussed in Section 9.3.2, when actuating with two inputs, the heating efficiency is lower compared to the actuation with one input. Therefore, the structure's thermal expansion is reduced and the Young's modulus is increased. Under these conditions, the resonance is shifted to higher frequencies compared to the ones detected when performing electro-thermal actuation with one input signal.

9.4.2 Resonant frequency shift - mechanical and thermal considerations

When electro-thermal actuation is performed, changes in the resonant frequency can be obtained by varying the bias amplitude of the actuating voltage [53]. This effect is due to the fact that when the bias voltage changes, the temperature within the device varies thus influencing the thermal expansion of the structure (i.e. geometry), the mechanical properties of the material (i.e. Young's modulus) and the thermal stress. As a consequence, the resonant frequency can be varied by operating on the input bias. As shown in Fig. 9.8, the shifting of the resonant peak when mixing has been observed

on the ring with $R = 190 \mu\text{m}$ and $h = 15 \mu\text{m}$. In the following experiments, the resonant frequency has been investigated by varying the DC bias voltage of one of the input signal and keeping the other one constant. In particular, V_{dc1} has been varied from 0.5 to 2 V, V_{dc2} kept constant at 2 V and $V_{pp1} = V_{pp2}$ set at 6 V. Fig. 9.9 shows the measured resonant frequency plotted as a function of V_{dc1} .

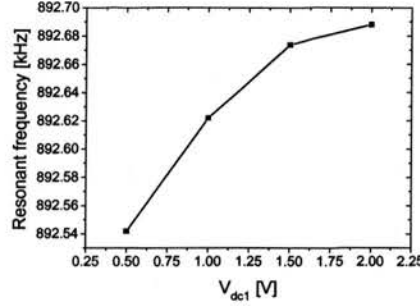


Figure 9.9: Measurements: mixing with a ring with $R = 190 \mu\text{m}$ $h = 15 \mu\text{m}$.

As the voltage increases, the resonant frequency has been observed to increase non-linearly from 892.54 to 892.69 kHz. In addition, when increasing V_{dc1} from 0.5 to 2 V the degree of the frequency shift has been shown to decrease from 8 to 1.4 %.

The influence of the changes in the bias voltage on the resonant frequency can be explained in a speculative way considering the temperature experienced by the structure. When one of the bias voltage changes, the temperature varies as a function of the power dissipated in the heating resistor hence influencing the degree of thermal expansion and the value of the Young's modulus.

Observing the equivalent circuit of the mixing configuration in Fig. 9.2, when the bias voltage V_{dc1} is increased from 0.5 to 2 V and V_{dc2} is fixed at 2 V, the resulting voltage drop V_R across the heating electrode decreases from 1.5 to 0 V. Similar to the case of mixing with cantilevers, the decrease of V_R leads to a decrease of the temperature induced within the structure. As a result, the ring radius becomes smaller due to the reduced thermal expansion effect while the Young's modulus increases [113]. These two effects contribute to the increase in the resonant frequency of the rings (see Eq. 3.7 and

Chapter 8 for the resonant frequency of disks and rings).

9.4.2.1 Thermal stress in rings

In addition to the change of geometry and Young's modulus, the effect of the thermal stress of the structure could influence the value of the resonant frequency. The total thermal stress σ_{th-R} for rings can be expressed as the sum of different factors and written as $\sigma_{th-R} = \sigma_{exp} + \sigma_{SiC-Si} + \sigma_{SiC-Al}$, where σ_{exp} is the stress due to the thermal expansion of the ring, σ_{SiC-Si} and σ_{SiC-Al} are the stress due to the difference between the TCEs of SiC (main structure), Si (substrate) and Al (electrode). The total thermal stress σ_{th-R} can change as a result of the dependence of these factors on temperature. In particular, the degree of σ_{th-R} is believed to diminish as the temperature decreases thus leading to a frequency decrease.

As discussed for cantilevers in Section 9.3.3.1, the precise contribution of these effects on the resonant frequency is difficult to evaluate. In the rings, as the voltage across the actuating electrode decreases, the resonant frequency is seen to increase probably due to the dimensional changes (i.e. smaller radius) and to the increase of the Young's modulus that have a stronger influence than the decrease of the total thermal stress of the structure. In addition, the saturation of the frequency shift as a function of the voltage could be explained by the interplay of the thermal effects as described.

9.5 Conclusions

In this chapter, thermo-mechanical frequency mixing has been demonstrated. First, the theory of electro-thermal transduction has been reviewed. Then, the possibility of mixing the frequencies of two input signals has been investigated theoretically. Frequency mixing has been demonstrated by testing cantilevers and rings fabricated with the techniques described in Chapter 4.

In general, electro-thermal transduction is performed by applying an alternating voltage to the structure that is to be actuated. In this way, electric current is dissipated thus generating Joule heat and inducing temperature oscillations within the device. As a result, a varying mechanical strain is experienced and vibrations are induced. Resonance is achieved when the frequency of the actuating voltage matches the natural resonant frequency of the structure. The induced force is proportional to the electrical power dissipated showing a quadratic dependence on the actuating voltage. The quadratic proportionality between the force induced and the input voltage can be exploited to implement the frequency mixing function. When two alternating voltages are applied, resonance can be achieved if the sum or the difference of the input frequencies equals the natural frequency of the structure.

The thermo-mechanical mixing of two input frequencies has been successfully achieved with the fabricated bimaterial Al/SiC cantilevers and rings. First, the structures have been actuated with one input signal so that the fundamental resonant frequency has been detected. Then, by applying two signals, resonance has been achieved when the sum or the difference of the two input frequencies matched the resonant frequency previously detected.

The mixing behaviour of the resonators has been confirmed by varying one of the input frequencies and measuring the vibration amplitude. In this way, lower vibration amplitudes have been obtained when shifting the frequency difference from the resonant frequency. This result has shown that mixing is achieved only when the structure's resonant frequency is matched.

In addition, the possibility of tuning the resonant frequency has been explored by varying the DC amplitude of one of the input voltages. An increase in frequency of ~ 0.15 Hz/V has been obtained. It is worth noting that the ability to shift the resonant frequency favours the integration of the devices for applications that may require the tuning of the operating frequency.

Chapter 10

Piezo-electric driven SiC single clamped beam resonators

10.1 Introduction

In the previous chapters, electro-thermal transduction has been explored as an actuation mechanism to induce resonance in bimaterial Al/SiC structures. The influence of the dimensions of Al electrodes on the induced deflections has been studied for optimising the performance of clamped-clamped beams resonators. Ring architectures have been proposed so that a higher resonant frequency range has been achieved. In addition, the possibility of performing frequency mixing with the bimaterial Al/SiC resonators has been demonstrated. The resonant frequency has been detected with an optical technique using a laser vibrometer. However, in order to employ these devices for MEMS sensors or RF applications, the electrical detection of the resonant frequency is required.

In this chapter, the piezo-electric transduction mechanism is explored for driving SiC MEMS resonators because of its feasibility as both actuation and sensing technique.

SiC single clamped beams (i.e. cantilevers) with top piezo-electric layers have been

studied. Lead zirconium titanate (PZT) has been chosen for the implementation of the electrodes because of its high piezo-electric coefficient. Particular attention has been focused on the electrodes dimensions because of the key role played in the actuation efficiency of the devices. The mechanical and modal behaviour of the devices has been investigated with finite element (FEM) simulations. An electrical characterisation has been performed by analysing the equivalent electrical circuit. Moreover, the SiC structures with top piezo-electric layers and fabricated with the process flow presented in Chapter 4 have been tested.

First, some considerations on the design and on the choice of the materials for fabricating the electrodes will be discussed. Then, the simulations and measurements results will be presented discussing the influence of the electrode dimensions on the actuation of the cantilevers and on the electrical output.

10.2 General considerations

10.2.1 Piezo-electric actuation and sensing

The mechanism of piezo-electric transduction has been introduced and discussed in Chapter 3, Section 3.4. When a piezo-electric material experiences a mechanical strain, a charge is induced on the material's surface and an electric field is observed within the material.

This mechanism can be used for inducing (actuating) or detecting (sensing) a mechanical deformation of a structure. In the actuation case, if the electric field is applied as a voltage difference across a piezo-electric suspended structure, a mechanical strain is generated and a deflection is observed. When an alternating voltage is applied, the structure can be driven into resonance if the voltage frequency matches the structure's fundamental mechanical resonant frequency. In the sensing case, if a deflection is experienced by a suspended piezo-electric structure, an electric field is generated across

the material thus a voltage difference is observed. In particular, if the structure is resonating, a change in the magnitude and phase of the impedance of the piezo-electric material is observed at the frequency of the vibration.

10.2.2 Design and fabrication

Piezo-electric layers have been implemented on top of suspended SiC cantilevers in order to investigate the possibility of inducing deflections in the vertical direction. As piezo-electric material, lead zirconium titanate (PZT) has been chosen because of its very high piezo-electric coefficient compared to other materials such as zinc oxide (ZnO) or aluminium nitride (AlN) (see Chapter 3, Section 3.4). In order to provide an electrical contact with the PZT, Pt has been used rather than Al because of the good adhesion with PZT. The details of the fabrication process have been presented in Chapter 4, Section 4.5.

With the described design, it has not been possible to bond the chips containing the fabricated devices to a chip carrier because of the incompatibility of gold-wire bonding with the Pt. Therefore, the devices could be tested only with probes at atmosphere pressure due to the limitations of the facilities available for the measurements.

Fig. 10.1 shows the schematic top and side views of the designed devices with the associated dimensions. The devices have been designed with a beam length L_b of 200 and 150 μm and electrode lengths L_e equal to L_b or $\frac{1}{2} \cdot L_b$. The materials forming the actuating electrode (Pt and PZT) have a relative large mass density. Therefore, as the electrode dimensions increase, the consequent increase in the electrode mass is expected to influence the fundamental mechanical resonant frequency of the cantilevers. FEM simulations and measurements have been performed in order to investigate the influence of the electrode length L_e on the mechanical and modal behaviour of the devices.

In order to apply a vertical electric field across the piezo-electric layer, bottom and top contact electrodes have been implemented with the Pt and made accessible separately

(see Fig. 10.1). Electrical insulation between the top and bottom Pt electrodes has been provided by the PZT itself exploiting its very low conductivity.

Particular attention has been paid on the capacitance of the electrode stack (Pt/PZT/Pt) because of its influence on the resonant behaviour of the structure [114]. This capacitance is directly dependent on the length of the track L_t that connects the actuating part of electrode (overlapping the suspended beam) to the external pad for the top contact (see Fig. 10.1). The effects of the electrode track length L_t and consequently of its capacitance on the overall impedance have been investigated first by simulating the device equivalent electrical circuit and then with measurements on the actual fabricated devices.

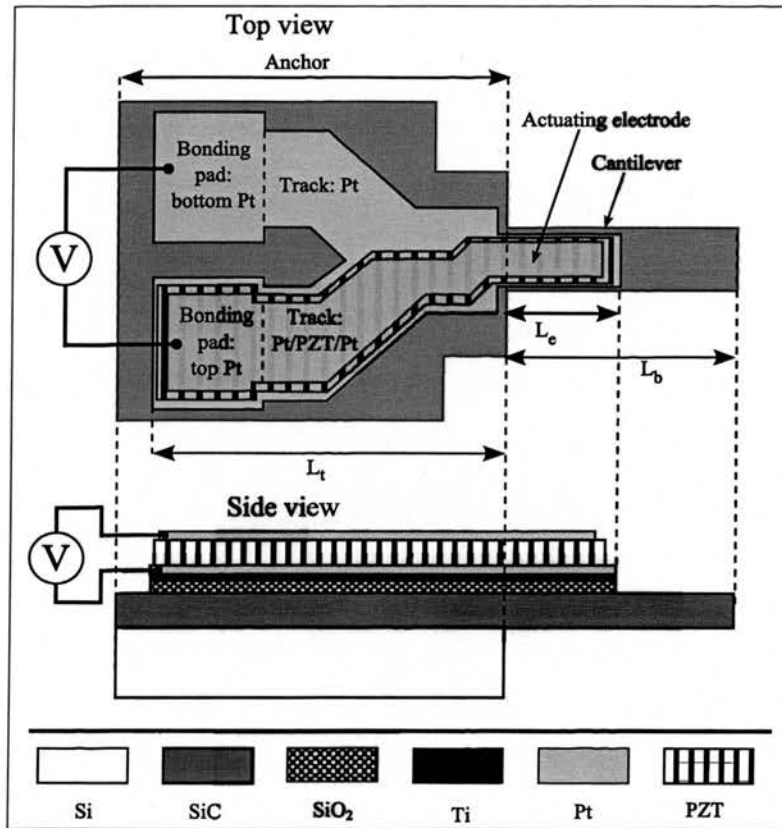


Figure 10.1: Schematic of the designed piezo-electric SiC cantilevers.

10.3 Simulations

The mechanical and modal behaviour of the SiC cantilevers as a function of the electrode length has been investigated with FEM simulations. In addition, the influence of the electrical capacitance, given by the piezo-electric layer, on the output impedance has been studied by simulating the resonator equivalent electrical circuit.

10.3.1 Mechanical behaviour - finite element analysis for different electrode lengths L_e

As mentioned in the previous section, the changes in the total mass of the structure due to the variations of the electrode dimensions are expected to influence the mechanical behaviour of the devices.

The study of the influence of the actuating electrode length L_e on the resonant frequency has been performed by fixing the cantilever length L_b at 200 μm and varying L_e in a range between 25 and 200 μm . The magnitude of the vertical displacement and the resonant frequency obtainable with different values of L_e has been investigated to optimise the design of the electrodes dimensions. Harmonic analysis has been performed to observe the influence of the electrode length L_e on the harmonic displacement.

10.3.1.1 Mechanical and modal analysis

The mechanical simulations have been performed applying a voltage difference of 0.5 V between the top and bottom surfaces of the PZT electrode thus inducing vertical deflections. Fig. 10.2 shows the displacement (10.2(a)) and the resonant frequency (10.2(b)) as a function of the electrode length L_e for a 200 μm long SiC cantilever. The inset of Fig. 10.2(a) shows one of the simulations snapshots.

From Fig. 10.2(a), the magnitude of the vertical displacement is observed to increase as the electrode length L_e increases. This is due to the fact that by increasing the

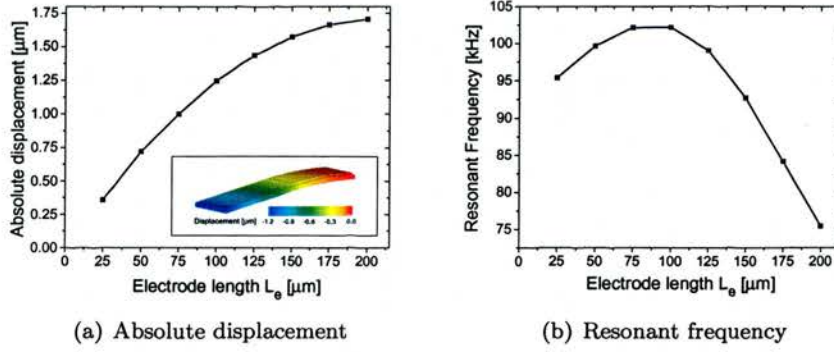


Figure 10.2: Simulations: static displacement and resonant frequency as a function of electrode length L_e of a SiC cantilever with $L_b = 200$ μm actuated piezo-electrically with a voltage of 0.5 V.

length of the actuating electrode, the induced force is distributed on a larger area. In addition, when the electrode moves towards the free end of the beam, the induced force is applied on the cantilever part that can deflect more.

From Fig. 10.2(b), the resonant frequency is observed first to increase as L_e increases from 25 to 100 μm and then to decrease for a further increase of L_e to 200 μm. This effect is probably due to the fact that the fundamental resonant frequency of a cantilever is directly proportional to the spring constant (dependent on the thickness and Young's modulus) and inversely proportional to the mass of the structure (see Eq. 3.1 in Chapter 3, Section 3.2). As the electrode length increases, the spring constant increases together with the mass of the structure. Initially, the increase of the spring constant has probably a stronger influence on the frequency than the increase of the mass and the resonant frequency is observed to increase. After a threshold of the electrode length $L_e \approx 100$ μm, the increase of the mass overwhelms the effect of the increase in the spring constant and the resonant frequency starts to decrease.

10.3.1.2 Harmonic analysis for different electrode lengths L_e

For the harmonic analysis, the simulations have been performed by applying an AC voltage of 0.5 V across the PZT electrode and scanning in a range of 8 Hz around the resonant frequency of the structure. Fig. 10.3 shows the obtained harmonic displacement plotted as a function of the frequency shift from the resonant frequency for electrode lengths $L_e = 25, 100, 150$ and $200 \mu\text{m}$. When actuating with longer electrodes, higher harmonic displacements have been obtained at resonance. These results are in good agreement with the mechanical analysis showing that as the electrode length L_e increases, the magnitude of the cantilever displacement increases.

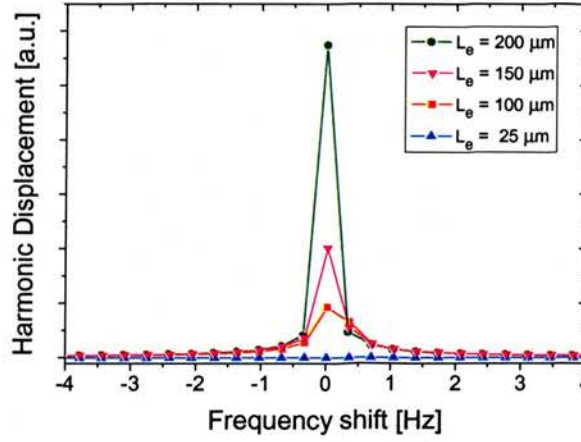


Figure 10.3: Simulations: harmonic displacement as a function of the shift from the resonant frequency for different electrode length L_e ($L_b = 200 \mu\text{m}$, actuation voltage = 0.5 V).

10.3.2 Electrical behaviour - circuit analysis for different track lengths

L_t

The electrical behaviour of a piezo-electric oscillator can be represented with an equivalent electrical circuit composed by resistive, capacitive and inductive elements. Simulations in the AC domain have been performed with a numerical computing environment (MATLAB) in order to investigate the influence of the electrodes dimensions on the

resonant behaviour of the structures.

Fig. 10.4(a) shows the Butterworth - Van Dyke equivalent circuit representation for electro-mechanical oscillators. The branch formed by the resistance R_m , the inductance L_m and the capacitance C_m is referred usually as the motional branch because it describes the mechanical behaviour (i.e. resonant frequency) of the structure. The electrical behaviour of the devices (i.e. static capacitance of the piezo-electric material) is represented by the parallel capacitance C_p (also referred as feedthrough capacitance).

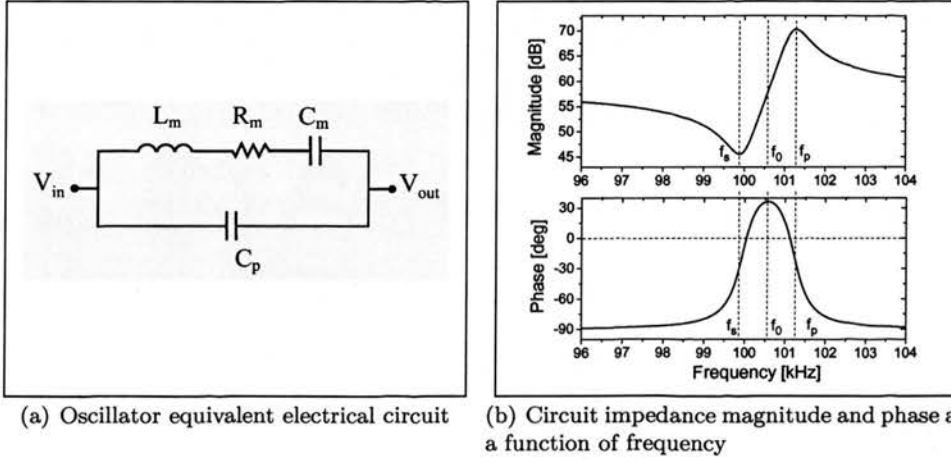


Figure 10.4: Butterworth - Van Dyke equivalent representation for electro-mechanical resonators.

The circuit represented in Fig. 10.4(a) is characterised by two frequencies referred as series resonant and parallel resonant frequency (f_s and f_p) because of their dependence on the elements in series (R_m , L_m , C_m) in the motional branch and to the parallel capacitor (C_p), respectively. In particular, the values of the two frequencies are given by:

$$f_s \approx \frac{1}{2\pi\sqrt{L_m C_m}} \quad (10.1)$$

and by

$$f_p \approx \frac{1}{2\pi\sqrt{L_m \frac{C_m C_p}{C_m + C_p}}} \quad (10.2)$$

Fig. 10.4(b) shows the typical plot of the impedance magnitude and phase for the Butterworth - Van Dyke equivalent circuit. The minimum and maximum values of the impedance magnitude are observed for frequencies matching f_s and f_p , respectively. It is important to notice from Eq. 10.1 and Eq. 10.2 that if $C_p \gg C_m$, the values of f_s and f_p are very similar so that the peaks of minimum and maximum impedance magnitude get very close to each other.

In the specific case of the designed piezo-electric SiC cantilevers, the series resonant frequency f_s is linked to the mechanical behaviour of the device thus representing the fundamental mechanical resonant frequency and depending on the dimensions of the suspended structure. The parallel resonant frequency f_p is related to the electrical capacitance and consequently to the dimensions of the piezo-electric layer (i.e. L_e of the actuating electrode and L_t of the electrode track, see Fig. 10.1). As mentioned in Section 10.2.2, in the designed devices, the parallel capacitance C_p can strongly influence the impedance of the electrode due to the relative large length L_t of the electrode track.

The impedance magnitude and phase have been simulated for different values of C_p in order to study the influence of the parallel capacitance on the electrical output of the devices. A capacitance of ~ 1.5 nF has been calculated for the piezo-electric track C_p assuming an electrical permittivity of 850 for the PZT layer [101]. The behaviour of the circuit has been explored by varying the value of C_p in the range between 0.5 and 1.5 nF. As far as the value of C_m is concerned, the calculations are quite complicated and require solving the Bessel function for the vibrational modes of the cantilever. However, by observing that C_m is related to the dimensions of piezo-electric part of the suspended structure, a good approximation can be obtained by calculating the capacitance of the actuating electrode. With this approximation, C_m has been set at 10 pF.

Fig. 10.5 shows the results obtained for the magnitude and phase of the circuit impedance as a function of the frequency shift from the series resonant frequency f_s .

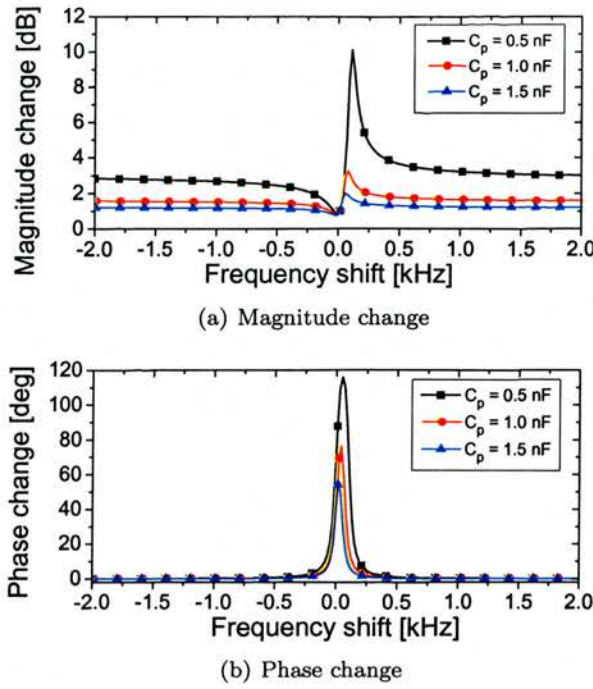


Figure 10.5: Simulations of equivalent electrical circuit: impedance change at resonance for different values of C_p .

As expected from Eq. 10.1 and Eq. 10.2, when the value of C_p decreases towards values comparable to C_m , the difference between the values of f_s and f_p becomes larger.

10.4 Measurements

The SiC cantilevers ($L_b = 200$ and $150 \mu\text{m}$) fabricated with top piezo-electric layers ($L_e = L_b$ and $\frac{1}{2} L_b$) have been actuated piezo-electrically and the resonant frequency detected by measuring the change of the impedance across the actuating electrode. In this section, the measurements setup and results are presented.

10.4.1 Measurements setup

Fig. 10.6 shows the schematic of the setup used for testing the fabricated devices. An LCR meter has been used to apply an alternating (AC) excitation voltage to the piezo-

electric layer and to monitor the impedance across the same electrode. In particular, the voltage has been applied to the piezo-electric layer with two probes connected to the top and bottom Pt contact pads (see Fig. 10.1). The electrode impedance has been analysed with a computer connected to the LCR meter.

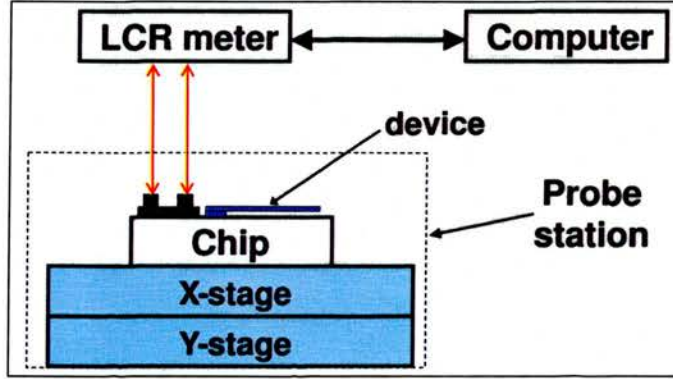


Figure 10.6: Schematic of the testing system setup for the piezo-electric driving (actuation and sensing) of the fabricated cantilevers.

In order to detect the resonance of the devices, the electrode impedance is investigated as a function of the frequency of the actuating voltage. When the input frequency matches the resonant frequency f_0 of the structure, a peak of the impedance phase is observed at f_0 that is positioned midway between f_s and f_p while minimum and maximum peaks of the impedance magnitude are observed at f_s and f_p , respectively, (see Fig. 10.4(b)).

10.4.2 Measurements results

The fabricated cantilevers have been actuated piezo-electrically by applying an alternating voltage with amplitude of 0.5 V and varying the input frequency between 50 and 200 kHz. The change of impedance at resonance has been investigated and compared for the two different electrode lengths. In addition, a further study has been performed to confirm the influence of the parallel capacitance C_p on the impedance change.

10.4.2.1 Impedance change at resonance

For cantilevers with a length $L_b = 200 \mu\text{m}$, resonant frequencies around 120 and 95 kHz have been detected for $L_e = 100$ and $200 \mu\text{m}$, respectively. In the case of cantilevers with a length $L_b = 150 \mu\text{m}$, frequencies around 180 and 140 kHz have been measured for $L_e = 75$ and $150 \mu\text{m}$, respectively. In agreement with the modal simulations, for a fixed beam length L_b , the cantilevers with electrodes covering the full length of the beam ($L_e = L_b$) have been shown to resonate at lower frequencies compared to the ones with electrodes covering the half length of the beam ($L_e = \frac{1}{2}L_b$). However, the tested devices have shown a higher resonant frequency compared to the simulated structures probably because the materials' stress has not been included in the simulations.

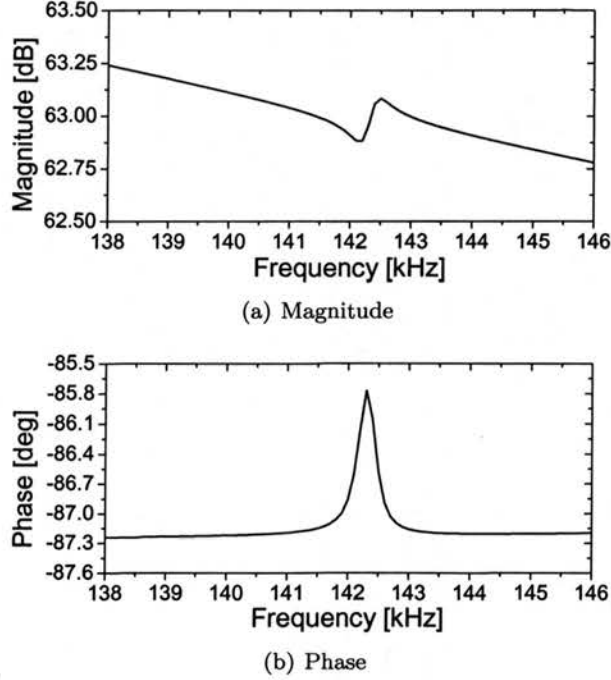


Figure 10.7: Measurements: electrode impedance (magnitude and phase) of a SiC cantilever $150 \mu\text{m}$ long actuated piezo-electrically.

Fig. 10.7 shows the impedance magnitude and phase detected for one of the tested cantilevers having a length $L_b = 150 \mu\text{m}$ and an electrode length $L_e = 75 \mu\text{m}$. For this device, the impedance peaks have been detected at $f_0 \approx 142.3 \text{ kHz}$. Although the

piezo-electric layer has been poled after deposition, for all the devices tested, relatively small changes in the impedance magnitude and phase have been detected. This effect is related to the fact that the devices have been tested at atmospheric pressure so that the mechanical vibration of the structure has been damped. Under these conditions, the change in the electrode impedance has been limited. In addition, by comparison with the simulations of the equivalent electrical circuit (Section 10.3.2), the small change in magnitude and phase indicates probably that the fabricated devices have a high parallel capacitance C_p (see Fig. 10.4).

10.4.2.2 Impedance change for different electrode lengths L_e

The change of impedance obtained when actuating with electrode lengths $L_e = L_b$ and $\frac{1}{2}L_b$ has been compared. A larger impedance change has been obtained with cantilevers actuated with longer electrodes.

As an example, Fig. 10.8 shows the impedance magnitude and phase obtained for two cantilevers having same beam length $L_b = 200 \mu\text{m}$ and different electrode length $L_e = 200$ and $100 \mu\text{m}$. It can be seen that the cantilever with a longer electrode exhibits a larger change in impedance magnitude (Fig. 10.8(a)) and a larger phase lag (Fig. 10.8(b)). An explanation of this can be found in the results of the mechanical simulations where the cantilevers deflection has been observed to increase as the electrode length increases. As a matter of fact, it is believed that the larger change of impedance is probably enhanced by the larger deflection induced with electrodes covering the full beam length ($L_e = L_b$).

10.4.2.3 Impedance change for different track lengths L_t - change of C_p

As mentioned above, the change of impedance magnitude and phase at resonance has been observed to be relatively small due to the fact that the testing has been performed at atmospheric pressure. However, as demonstrated in Section 10.3.2, the parallel

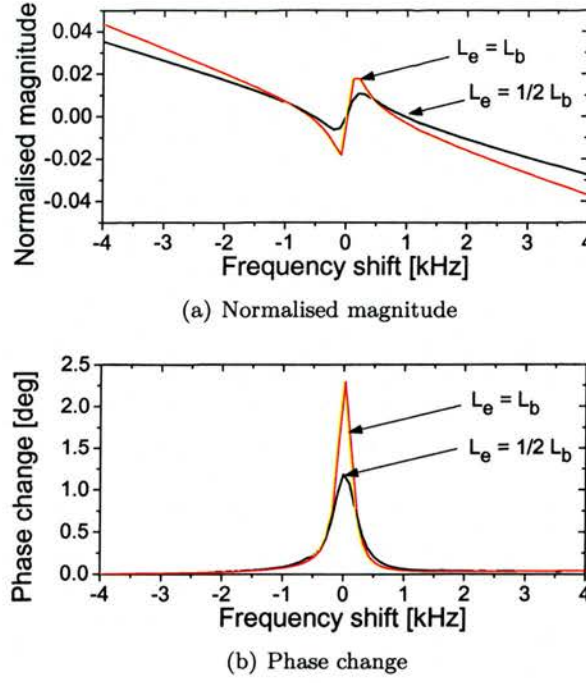


Figure 10.8: Measurements results: impedance change as a function of frequency shift from resonance for a SiC cantilever 200 μm long actuated piezo-electrically with electrode length $L_e = 200$ and $100 \mu\text{m}$.

capacitance C_p can influence the changes in magnitude and phase of the impedance. In particular, from the simulations, it has been observed that by decreasing the value of C_p , the change of magnitude and phase increases.

As discussed in Section 10.3.2, the parallel capacitance C_p is associated to the electrical behaviour of the resonator. Consequently, the value of C_p is given with a good approximation by the capacitance measured across the patterned piezo-electric layer formed by the actuating part overlapping the cantilever and by the track connecting to the bonding pads (see Fig. 10.1). In the fabricated structures, the dimensions of the track (i.e length and width) are much greater than the actuating electrode ones. Therefore, the value of C_p is affected mainly by the electrode track. The total capacitance between top and bottom Pt has been measured with the LCR meter at 20 Hz showing values in a range between 1 and 1.2 nF depending on the tested device.

In order to decrease the parallel capacitance, a Focused Ion Beam (FIB) has been used to cut the electrode track formed by the Pt/PZT/Pt stack (see Fig. 10.1) of one of the cantilevers with $L_b = 200 \mu\text{m}$ and $L_e = 100 \mu\text{m}$. The cuts have been performed in three different points starting from a position close to the bonding pads. Fig. 10.9 shows the SEM picture taken after performing the cuts on the electrode track. After each cut, the capacitance has been measured, the cantilever actuated and the change of impedance at resonance investigated. The measurements have shown that the capacitance has been reduced from $\sim 1 \text{ nF}$ (before cutting) to $\sim 20 \text{ pF}$ (after the third cut).

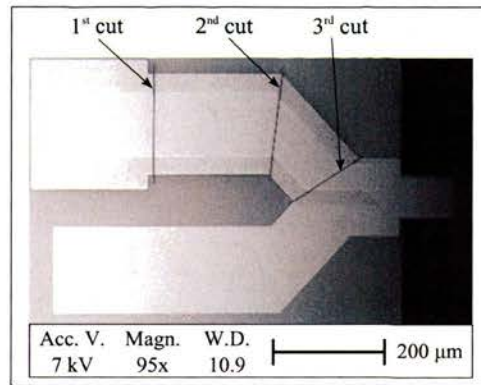


Figure 10.9: Scanning electron micrograph of the Pt/PZT/Pt electrode showing the three cuts performed with the FIB tool.

Fig. 10.10 shows the impedance magnitude and phase measured for the different values of capacitance obtained. The normalised magnitude and phase change have been plotted as a function of the frequency shift from resonance for facilitating the comparison between the different curves.

The lowest peak of magnitude and the smallest phase lag have been obtained for the highest value of $C_p = 960 \text{ pF}$. In addition, as expected from the simulations of the equivalent electrical circuit, by decreasing the value of C_p , the change of magnitude and the phase lag at resonance have been shown to increase. With the lowest value of $C_p = 20 \text{ pF}$, a change of impedance magnitude of $\sim 2.5 \text{ dB}$ and a phase lag of ~ 16 degrees have been obtained.

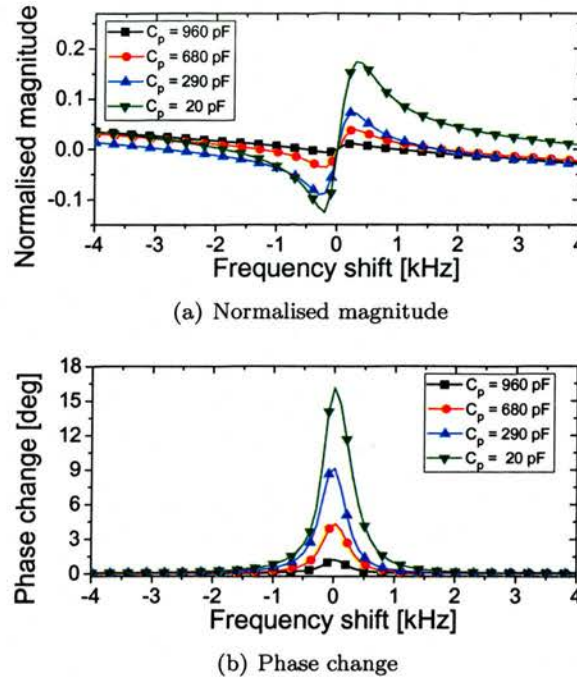


Figure 10.10: Measurements results: impedance change as a function of frequency shift from resonance for different values of C_p .

10.5 Conclusions

In this chapter, piezo-electric transduction has been explored as a technique for driving SiC MEMS. In particular, it has been used to induce resonance to SiC cantilevers and to detect the resonant frequency of the structure. The results obtained from the simulations of the designed devices and from the measurements performed on the fabricated structures have been presented. Particular attention has been focused on the influence of the electrode capacitance on the changes of the electrode impedance at resonance.

FEM simulations have been used to study the mechanical and modal behaviour of SiC cantilevers with top electrodes formed by a stack of Pt/PZT/Pt. The simulations have been performed using the PZT layer as piezo-electric active material and applying a voltage drop across the piezo-electric layer thus inducing vertical deflections. The

influence of the electrode dimensions on the induced displacement and on the resonant frequency has been analysed. The cantilever absolute displacement, the fundamental resonant frequency and the harmonic displacement have been investigated as a function of the actuating electrode length. The absolute displacement has been shown to increase as the electrode length increases (i.e. the electrode moves towards the free end of the beam). The same trend has been observed for the harmonic displacement at resonance. The resonant frequency has been observed first to increase reaching a maximum when the electrode covers the half of the beam and then to decrease for further increases of the electrode length. These results have shown that an accurate design of the actuating electrode dimensions gives the possibility of maximising the beam deflection and/or tuning the resonant frequency. It is believed that the maximisation of the absolute displacement facilitates its detection when the sensing of the vibration is required.

In addition to the FEM analysis, the Butterworth - Van Dyke equivalent electrical circuit of the resonators has been studied. This equivalent model is formed by two impedance branches representing the motional (i.e. series impedance) and electrical (i.e. parallel capacitance) behaviour of the resonator. In agreement with the literature, the simulations have shown that a change in the circuit impedance is observed when the circuit experiences resonance. The degree of impedance magnitude and phase change has been observed to increase as the value of the parallel capacitance decreases. Due to the correspondence between the resonator and the equivalent circuit, the change of impedance can be used to detect the resonant frequency of the actual fabricated devices.

SiC cantilevers with a length of 200 and 150 μm have been fabricated with top electrodes formed by a stack of Pt/PZT/Pt. The fabrication process flow has been presented and discussed in Chapter 4, Section 4.5. The devices fabricated with different electrode lengths have been tested at atmospheric pressure with the use of an LCR meter. The structures have been actuated piezo-electrically by applying an AC voltage across the top and bottom Pt contacts so that a vertical electric field has been generated across the

piezo-electric PZT layer. Resonant frequencies in the kHz range have been detected by monitoring the change of impedance of the piezo-electric layer. The influence of the electrode length on the resonant frequency and on the electrode impedance has been investigated. In agreement with the FEM simulations, for a fixed beam length, the resonant frequency has been shown to be higher when the electrodes cover half of the beam compared to the case of electrodes covering the full length of the beam. In addition, the change of impedance magnitude and phase is larger for longer electrodes probably due to the larger deflection induced.

In general, the changes of the impedance magnitude change and phase have been observed to be relatively small with values of ~ 0.25 dB and ~ 2 degrees, respectively. This effect is due to the fact that the devices have been tested at atmospheric pressure and to the influence of the electrical capacitance formed by the actuating part of the piezo-electric layer (overlapping the cantilever) and by the track connecting to the bonding pads. The electrical capacitance has been decreased by cutting some parts of the electrode track with the use of a FIB tool. In this way, the initial capacitance has been decreased from ~ 1 nF to ~ 20 pF. In agreement with the equivalent circuit analysis, the change of impedance has been observed to increase as the electrical capacitance decreases. Values of ~ 2.5 dB for the magnitude change and ~ 16 degrees for the phase lag have been obtained with an electrical capacitance of 20 pF.

The piezo-electric transduction technique has been shown to be an optimum technique to drive SiC resonators combining actuation and sensing on the same electrode. In addition, piezo-electric sensing can be considered as a method for detecting the resonant frequency of devices actuated with other excitation techniques. In particular, it could be combined with electro-thermal actuation for the implementation of MEMS filters and mixers with an electrical reading output.

Chapter 11

Conclusions and future work

This thesis has presented the design, fabrication and characterisation of SiC micro-mechanical vertical resonators. A fabrication process flow for SiC structures has been developed with the option of integrating metal electrodes on top of the devices. SiC cantilevers, bridges and rings (circular membranes with a hole in the centre) have been fabricated. The quality and structure of the SiC crystals and the elastic modulus have been evaluated. Electro-thermal and piezo-electric transductions have been used as actuation and sensing techniques. The influence of the electrodes' dimensions on the electro-mechanical behaviour of the devices has been investigated in order to optimise the actuation efficiency. The relationship between the rings' dimensions and the resonant frequency has been studied with the aim of maximising the operating frequency of the devices. Furthermore, the ability of performing electro-thermal frequency mixing has been demonstrated. As a technique for detecting the devices' resonance, piezo-electric sensing has been explored focusing on the influence of the electrode dimensions and feedthrough capacitance on the electrical output.

In the first part of this chapter, the major findings and conclusions presented in the previous chapters are summarised. In the second part, the discussion continues with some suggestions on future investigations and work that have emerged from the results

obtained in the thesis.

11.1 Fabrication of SiC MEMS resonators

SiC resonators with rectangular and circular shapes have been fabricated using a surface micromachining process that has been described in Chapter 4. Single and polycrystalline SiC films grown on single crystalline Si substrates and polycrystalline SiC films grown on poly-Si/SiO₂/Si substrates have been used. The process flow has been shown to be particularly suitable for SiC surface micromachining. Nevertheless, some modifications can be introduced for adapting it to bulk micromachining.

The SiC structures have been patterned with a one-step etch and release process. In particular, using an inductively coupled plasma with a SF₆/O₂ gas mixture, first the SiC epilayer has been etched and then the bottom Si sacrificial layer removed. An additional step of XeF₂ dry vapour etching has been employed to complete the removal of large volumes of sacrificial material. The release rate during the XeF₂ etching has been controlled by operating on the process pressure conditions so that the structures' undercut could be minimised.

In the first stage of the development of the process flow, the SiC etch and release step has been characterised and single material structures fabricated. Optimal etching and release conditions have been obtained with a chamber pressure of 7 mT and SF₆ and O₂ flow rates of 55 and 10 sccm, respectively. The platen and coil power have been fixed at 50 W and 900W. Under these conditions, the SiC is etched at ~ 200 nm/min and the Si released at ~ 10 μ m/min.

In the second stage, a metallisation step has been introduced before the SiC etch and release so that top metal electrodes could be patterned in order to provide an electrical connection to the devices. Al layers have been used for implementing top electrodes on SiC bridges and rings (bimaterial Al/SiC structures). In addition, PZT

electrodes have been implemented on SiC cantilevers. In this case, the PZT layer has been stacked between two Pt layers to obtain ohmic contacts (PZT/SiC structures). All the fabricated devices have been employed as vertical resonators. Electro-thermal and piezo-electric transductions have been performed to actuate the Al/SiC and PZT/SiC structures, respectively.

11.2 Characterisation of SiC

After presenting the fabrication process flow, the results from the characterisation of two type of SiC layers grown on single crystalline Si substrates have been discussed in Chapter 5. The analysed SiC layers have been grown by hot-wall LPCVD in the Department of Physics, Chemistry and Biology of *Linköping University* (Sweden) at different temperature and pressure conditions (400 mbar - 1280 °C and 300 mbar - 1350 °C). Raman spectroscopy measurements have shown that the SiC grown at lower pressure and higher temperature exhibits a higher crystal quality compared to the one grown at higher pressure and lower temperature. In addition, the X-ray diffraction analysis has shown a single crystalline orientation for the film with a better crystal quality.

The Young's modulus of the SiC layers has been calculated from the fundamental resonant frequency of the single material cantilevers fabricated with different lengths. In this case, the structures have been actuated with an external mechanical excitation (piezo-electric disc) and the resonant frequency detected with an optical technique (laser vibrometer). A Young's modulus of 446 ± 3 GPa and 246 ± 11 GPa has been calculated for the single and poly-crystalline layers, respectively, confirming the higher quality of the single crystalline SiC grown at lower pressure and higher temperature conditions.

11.3 Optimisation of electro-thermal actuation - shape and dimensions of the electrode

Investigations on the shape and dimensions of the actuating electrodes have been carried out for optimising the efficiency of electro-thermal transduction in SiC bridges with top Al electrodes. The influence of the electrode design (u-shaped and slab) and dimensions (length, width and spacing) on the induced temperature gradients, structures' displacement and vibration amplitude has been analysed and the results have been presented in Chapter 6 and Chapter 7.

Finite element (FEM) simulations have been used for studying the bridges' steady displacements and temperature gradients when applying a DC voltage to the Al actuating electrode. Optical measurements have been used for detecting the vibration amplitude at resonance when applying an AC input voltage to the Al actuating electrode. Bridges with a length of 200 and 150 μm have been simulated and tested and resonant frequencies up to ~ 1.1 MHz have been measured.

In the simulations for the DC input voltage, an absolute temperature difference (i.e. increase of the structure's initial temperature) has been observed to be induced together with a vertical temperature difference between the top and bottom surfaces. The interaction between these two temperature gradients has been shown to be a key factor for the mechanical behaviour of the structures. A correspondence between the simulated displacement magnitude and the measured vibration amplitude has been observed.

11.3.1 U-shaped electrodes

The simulations have shown that the u-shaped electrodes induce downwards deflections on the side of the bridge where the Al does not overlap the SiC (single material behaviour influenced by the vertical temperature difference) and upwards deflections where the Al overlaps the SiC (bimaterial behaviour influenced by the absolute temper-

ature difference). These two opposite displacements interact together influencing the overall maximum displacement that has been observed to be either negative or positive.

As the electrode length increases, the absolute temperature difference decreases and appears to be more distributed along the beam while the vertical temperature difference decreases. Short electrodes ($< \frac{1}{3}$ of the bridge length) induce a relatively large vertical temperature difference thus leading to a negative (downwards) maximum displacement. Long electrodes ($> \frac{1}{3}$ of the bridge length) induce a small vertical temperature difference thus leading to a positive (upwards) maximum displacement.

The simulated displacement magnitude and the measured vibration amplitude can be maximised using short and wide electrodes designed with a small distance between the electrode arms. The most significant finding is that when the u-shaped electrode covers less than $\frac{1}{4}$ of the bridge length, the induced simulated displacement magnitude and measured vibration amplitude are comparable (and larger for wide electrodes) to the ones obtained when the electrode covers $\sim \frac{2}{3}$ of the bridge length.

11.3.2 Slab electrodes

If a slab (or plate) configuration is used, the width and the spacing of the u-shaped electrode are maximised and minimised, respectively. Therefore, the possibility of enhancing the displacement magnitude and vibration amplitude of the Al/SiC bridges with slab electrodes has been investigated with simulations and measurements, respectively.

The length of a slab electrode influences the simulated displacement and the measured vibration amplitude of the bridge similar to the u-shaped case. However, downwards simulated deflections have been obtained for all the electrode lengths due to the relatively large vertical temperature difference always present and located at the root of the bridge. The maximum simulated displacement is reached when the slab covers $\frac{1}{3}$ of the bridge length while the maximum measured vibration amplitude is obtained for

an electrode length of $\frac{2}{3}$ of the bridge length. This discrepancy has been attributed to the length of the fabricated bridges that is longer than the simulated one due to the undercut at the anchors. The slab electrodes generate larger temperature gradients compared to u-shaped architectures with comparable lengths thus inducing larger displacement magnitudes and vibration amplitudes.

11.4 Maximisation of resonant frequency - shape and dimensions of the structure

SiC ring structures have been analysed in order to increase the frequency range of the devices. The results from this investigations have been discussed in Chapter 8.

From the simulations and measurements performed on the fabricated devices, rings have been shown to resonate at higher frequencies than bridges or cantilevers with comparable dimensions. In addition, the resonant frequency has been observed to increase when the ring becomes thinner (i.e increasing the size of the central hole and keeping the distance between the centre of the structure and outer perimeter constant). Frequencies up to ~ 150 MHz have been simulated with rings having a radius of $20\ \mu\text{m}$ and a hole diameter of $15\ \mu\text{m}$. However, due to the limitations of the measurement setup, values only up to ~ 8 MHz could be detected for the devices fabricated with a radius of $46\ \mu\text{m}$ and a hole radius of $6\ \mu\text{m}$.

The Al/SiC rings have been actuated electro-thermally. The simulated displacement magnitude and the measured vibration amplitude have been maximised by using two u-shaped electrodes positioned diametrically opposed. Quality factors up to 22000 have been measured for the rings fabricated with single crystalline SiC.

11.5 Electro-thermal mixing on Al/SiC structures

Once the criteria for maximising the electro-mechanical coupling and resonant frequency in SiC vertical resonators have been defined, the ability of mixing electro-thermally two input frequencies has been demonstrated in Chapter 9. When performing electro-thermal actuation, the induced mechanical force is proportional to the power dissipated in the electrode and consequently to the square of the input voltage. Frequency mixing can be performed by exploiting this square-law proportionality existing between the mechanical and electrical domains.

Electro-thermal mixing has been demonstrated with Al/SiC cantilevers and rings resonating at frequencies up to ~ 900 kHz. Resonance has been detected when applying two input voltages with the sum or difference of their frequencies matching the fundamental resonant frequency of the structures. In this way, the two input electrical signals are converted and elaborated in the mechanical domain resulting in the mechanical resonance of the structure. Therefore, the “output” resonant frequency is the result of the mixing of the two input frequencies. Furthermore, by varying the DC bias of one of the input signals, the ability of tuning the mixed frequency has been demonstrated in a ring resonator obtaining a tuning capability of 0.15 Hz/V.

11.6 Piezo-electric driving of SiC cantilevers

The resonant frequency of the devices actuated electro-thermally has been detected optically with the use of a laser vibrometer. However, electrical detection is required if aiming to the connection and integration of the devices with a sustaining electronic circuit. In Chapter 10, piezo-electric transduction has been investigated as a driving (actuating and sensing) technique for SiC cantilevers focusing on the influence of the electrode length on the performance of the devices. The measurements could be performed only at atmospheric pressure due to the limitations of the testing system. As

a consequence, cantilever architectures have been preferred because of the ability of generating relatively large displacements.

PZT has been chosen as the electrode material because of its high piezo-electric coefficients. The PZT electrodes have been positioned on top of the SiC cantilevers so that vertical deflections could be induced. The fabricated devices have been successfully actuated and resonant frequencies up to ~ 180 kHz have been detected by monitoring the peaks of impedance magnitude and phase of the electrode.

FEM simulations have been used to investigate the influence of the electrode length on the induced deflection and resonant frequency. As the electrode length increases, the absolute maximum displacement increases reaching a maximum when the electrode covers the full-length of the beam. In addition, due to the relatively large dimensions and mass of the electrode, the resonant frequency is influenced strongly by the electrode length and is maximised when the electrode covers $\frac{1}{2}$ of the beam length.

An electrical equivalent model for the resonator has been developed to study the influence of the feedthrough capacitance on the output impedance of the device. In agreement with the results obtained from the electrical model, the measurements have demonstrated that the electrical output is enhanced (i.e. large change of impedance magnitude and phase at resonance) by minimising the feedthrough capacitance. Furthermore, an additional enhancement of the electrical output has been obtained by using an electrode covering the full-length of the cantilever.

11.7 Future work

The results presented in this thesis open new perspectives for MEMS resonators in the field of RF applications. However, future work is required in order to provide a complete characterisation and optimisation of the proposed devices.

11.7.1 Electro-thermal actuation reliability

The possibility of implementing an electro-thermo-mechanical oscillator capable of performing simultaneously frequency filtering and mixing functions has been demonstrated. The performance of the devices actuated electro-thermally should be tested with reliability and lifetime measurements to observe the influence of the environment conditions (i.e. temperature, pressure and humidity) and structure's degradation on the operating resonant frequency. Afterwards, the reliability, power consumption and overall dimensions of the SiC devices need to be compared to the ones of similar devices made of Si and quartz.

11.7.2 piezo-electric active layers design

Piezo-electric transduction has been demonstrated to be a suitable method for sensing electrically the structures' resonance. The integration of piezo-electric active layers for sensing purposes brings two major advantages. First, the limitations of optical measuring tools could be overcome thus eliminating the issues related to the detection of very high frequencies. Second, an electrical output signal could be generated and transferred directly to the sustaining electronics. However, in order to provide a considerable electrical output, the feedthrough capacitance has to be minimised. Therefore, some modifications are required to the design proposed and to the fabrication process developed for the piezo-electric layers. In addition, a very thin Al layer is needed on top of the Pt bonding pads to wire-bond the devices. It is worth noting that the chips with the piezo-electric devices have not been mounted on a testing package because of the inability of bonding with gold wires to the Pt pads. Consequently, the testing of the devices has been performed at atmospheric pressure due to the limitations of the equipment available. The packaging of the fabricated chips will allow the testing of the devices in vacuum. Finally, investigations similar to the ones carried out for the piezo-electrically driven cantilevers should be performed for bridge and ring structures

so that the electro-mechanical coupling and operating frequency can be maximised.

11.7.3 SiC electro-thermal filter-mixer with piezo-electric sensing

Electrodes for electro-thermal actuation and piezo-electric sensing can be integrated on a single SiC structure. In this device, the input electrical signals are converted and elaborated electro-thermally into the mechanical domain. Then, the signal is reconverted into the electrical domain through piezo-electric transduction and the electrical output sent forward to the sustaining electronics. The proposed device could substitute the analogue circuitry that performs frequency filtering and mixing in the existing transceivers having possible advantages such as lower power consumption and smaller occupied areas. Fig. 11.1 shows a schematic of a possible SiC electro-thermal filter-mixer with piezo-electric sensing.

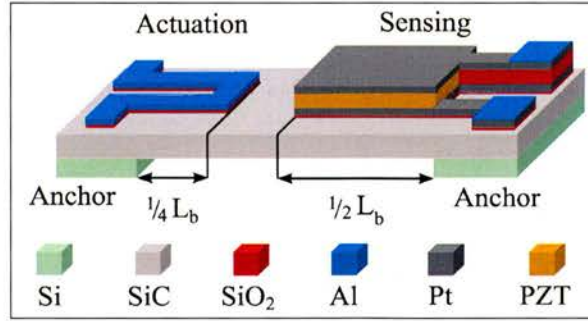


Figure 11.1: Schematic of SiC bridge with top electrodes for electro-thermal actuation and piezo-electric sensing.

In light of what has been found in this thesis, the structure shown in Fig. 11.1 should be made of single crystalline SiC in order to maximise the operating frequency of the device. The distance between the actuating and sensing electrodes should be maximised in order to reduce any cross-talk issues. Therefore, the actuating electrode is designed with a u-shaped or slab configuration having a length equal to $\frac{1}{4}$ of the bridge length so that the vibration amplitude is maximised. Furthermore, if short actuating electrodes are designed, the remaining area is available for the sensing electrodes.

The piezo-electric active layer should cover $\frac{1}{2}$ of the bridge length so that the electrical

output can be maximised. It is important to notice that in order to minimise the feedthrough capacitance, a layer of SiO_2 has been introduced between the top and bottom Pt layers in the track connecting to the sensing electrode. Finally, a very thin layer of Al on top of the Pt pads should be included for bonding purposes.

A similar design as the one proposed for bridges in Fig. 11.1 can be adopted for ring structures thus increasing the operating frequency of the devices.

11.8 Final conclusions

The work presented has shown that electro-thermal and piezo-electric transductions are suitable actuating and sensing methods for SiC vertical resonators. SiC cantilever, bridge and ring resonators have been fabricated and tested successfully. The design of the electrodes has been optimised in order to enhance the electro-mechanical coupling. The resonant frequency is an important factor when designing micro-mechanical resonators in order to match the application requirements. For vertical resonators, the frequency increases with the shrinking in size of the structure. The possibility of increasing the frequency up to tens of MHz without reducing dramatically the structures' dimensions has been demonstrated using SiC rings. In addition, this thesis has demonstrated the ability of using electro-thermal transduction for performing frequency mixing that is one of the essential functions in transceiver devices. Piezo-electric transduction has been shown to be a suitable detection method for sensing the resonance of the SiC devices. When piezo-electric sensing is employed, the electrode design plays an important role for the maximisation of the electrical output.

The discussed results can contribute to the introduction of MEMS resonators in RF applications. Due to its excellent mechanical properties, SiC is expected to improve the performance and reliability of MEMS resonators. The fabrication process, structures and transduction methods developed in this work can be employed in other applications such as sensors or energy harvesting devices.

Appendix A

Materials parameters used in the simulations

Material properties of Silicon (Si), Silicon carbide (SiC) and Silicon oxide (SiO₂).

parameter	Si	SiC	SiO ₂
Young's Modulus [GPa]	170	440	70
Poisson ratio	0.3	0.186	0.17
Mass density [kg/m ³]	2500	3210	2150
Stress [MPa]	-	200 - 500	-
Thermal exp. coeff. [10 ⁻⁶ /°C]	2.5	2.5	0.5
Thermal conductivity [W/m °C]	148	400	1.4
Electrical conductivity [S/m]	-	66.6	0
Piezo-electric coeff. (d ₃₁) [m/V]	-	-	-

Table A.1: Material properties used in the finite element simulations.

Material properties of Aluminium (Al), Platinum (Pt), Lead zirconium titanate (PZT) and Titanium (Ti).

parameter	Al	Pt	PZT	Ti
Young's Modulus [GPa]	77	145	63	110
Poisson ratio	0.3	0.35	0.31	0.33
Mass density [kg/m ³]	2300	21400	7600	4500
Stress [MPa]	100	-	-	-
Thermal exp. coeff. [10 ⁻⁶ /°C]	23	8.9	-	8.6
Thermal conductivity [W/m °C]	240	71.6	-	21.9
Electrical conductivity [S/m]	$3.54 \cdot 10^7$	$9.45 \cdot 10^6$	$9.45 \cdot 10^{-18}$	$2.56 \cdot 10^6$
Piezo-electric coeff. (d ₃₁) [m/V]	-	-	$1.8 \cdot 10^{-10}$	-

Table A.2: Material properties used in the finite element simulations.

Appendix B

Fabrication process details

B.1 Tools used for the fabrication

- Karl Suss: photolithography (3-8 inch wafers);
- Cobilt: photolithography (1 cm² chips);
- Balzers: metal sputterer;
- STS PECVD: plasma enhanced chemical vapour deposition tool used for depositing SiO₂;
- STS RIE: reactive ion etching used for metals;
- STS ICP - RIE etcher: inductively coupled plasma reactive ion etching used for SiC etching and release;
- ANS Veeco Ion Source: Ion Beam tool used for Ar milling of Pt;
- Plasmatherm: SiO₂ etching;
- Barrel Asher: O₂ plasma used for photoresist removal;
- MEMSSTAR: XeF₂ dry chemical etching.

B.2 PZT etching

Concentrations of the different acids used:

- HF: 48%;
- NH_4F : 40%;
- HCl: 38%;
- NH_4Cl : 99.8%;
- HNO_3 : 60%;

Appendix C

Young's modulus calculation

C.1 Measured resonant frequencies

(a) Poly-crystalline SiC

Length	Resonant frequency		
	device 1	device 2	device 3
[μm]	[kHz]	[kHz]	[kHz]
200	n.a.	57.5	74.7
150	118.9	119.2	96.5
100	215.5	208.6	214.5
50	730.0	745.0	727.0

(b) Single crystalline SiC

Length	Resonant frequency		
	device 1	device 2	device 3
[μm]	[kHz]	[kHz]	[kHz]
200	113.4	113.5	113.0
150	196.1	196.6	196.3
100	423.5	424.6	424.1
50	1483.0	1480.0	1250.0

Table C.1: Measured resonant frequencies.

C.2 Average Young's modulus and standard deviation

Cantilever resonant frequency:

$$f_C = 0.162 \sqrt{\frac{E}{\rho}} \frac{t}{L^2}. \quad (\text{C.1})$$

Solving Eq. C.1, the Young's modulus results:

$$E = \left(\frac{f_C \cdot L^2}{0.162 \cdot t} \right)^2 \cdot \rho. \quad (\text{C.2})$$

Young's modulus calculated from the measured resonant frequencies using Eq. C.2 with associated average and standard deviation values:

(a) Poly-crystalline SiC

Length	Young's modulus			Average	STDV
	E_1	E_2	E_3	E_{av}	ΔE
[μm]	[GPa]	[GPa]	[GPa]	[GPa]	[GPa]
200	n.a.	329	555	442	160
150	445	447	293	395	88
100	289	271	286	282	10
50	207	216	206	210	6

(b) Single crystalline SiC

Length	Young's modulus			Average	STDV
	E_1	E_2	E_3	E_{av}	ΔE
[μm]	[GPa]	[GPa]	[GPa]	[GPa]	[GPa]
200	471	474	475	473	2
150	449	451	449	450	1
100	413	416	415	415	1
50	317	316	225	316	53

Table C.2: Young's modulus calculated from the measured resonant frequencies.

C.3 Final value of the Young's modulus and error estimation

C.3.1 Poly-crystalline SiC

Young's modulus:

$$E_f = \frac{282 + 210}{2} = 246 \text{ GPa} \quad (\text{C.3})$$

Standard deviation:

$$\Delta E_f = \sqrt{10^2 + 6^2} = 11 \text{ GPa} \quad (\text{C.4})$$

C.3.2 Single crystalline SiC

Young's modulus:

$$E_f = \frac{473 + 450 + 415}{3} = 446 \text{ GPa} \quad (\text{C.5})$$

Standard deviation:

$$\Delta E_f = \sqrt{2^2 + 1^2 + 1^2} = 3 \text{ GPa} \quad (\text{C.6})$$

Appendix D

Published and accepted papers

T. T. Zhu, P. Argyrakis, E. Mastropaolo, K. K. Lee and R. Cheung; "Dry etch release processes for micromachining applications"; *Journal of Vacuum Science and Technology B*, **25**, 2553, 2007.

E. Mastropaolo and R. Cheung; "Electrothermal actuation studies on silicon carbide resonators"; *Journal of Vacuum Science and Technology B*, **26**, 2619, 2008.

E. Mastropaolo, R. Cheung, A. Henry and E. Janzn; "Fabrication of beam resonators from hot-wall chemical vapour deposited SiC"; *Microelectronic Engineering*, **86**, 1194, 2009.

E. Mastropaolo, R. Cheung, A. Henry and E. Janzn; "Electrothermal actuation of silicon carbide ring resonators"; *Journal of Vacuum Science and Technology B*, **27**, 3109, 2009.

A. Henry, E. Janzn, E. Mastropaolo and R. Cheung; "Single Crystal and Polycrystalline 3C-SiC for MEMS Applications"; *Materials Science Forum*, **615-617**, 625, 2009.

E. Mastropaolo, G.S. Wood and R. Cheung; "Electro-thermal behaviour of Al/SiC clampedclamped beams"; *Microelectronic Engineering*, **87**, 573, 2010.

E. Mastropaolo, I. Gual, and R. Cheung; "Silicon carbide electrothermal mixer-filters"; *Electronics Letters*, **46**, 62, 2010.

E. Mastropaolo, I. Gual and R. Cheung; "Silicon carbide electro-mechanical resonators"; *Proceedings of the Institution of Mechanical Engineers, Part N, Journal of Nanoengineering and Nanosystems*, **223**, 176, 2010.

E. Mastropaolo, I. Gual, G. Wood, A. Bunting and R. Cheung; "Piezo-electrically driven silicon carbide resonators"; to be published in Journal of Vacuum Science and Technology B, 2010.

References

- [1] V. Kaajakari, *Practical MEMS*. Small Gear Publishing, 2009. 2, 4, 48
- [2] R. P. Feynman, "There's plenty of room at the bottom." Presentation at the American Physical Society, 1959. 2
- [3] H. C. Nathanson, W. E. Newell, R. A. Wickstrom, and D. J. R., "The resonant gate transistor," *IEEE Transactions On Electron Devices*, vol. 14, 1967. 2
- [4] R. J. Wilfinger, P. H. Bardell, and D. S. Chhabra, "The resonistor: A frequency selective device utilizing the mechanical resonance of a silicon substrate," *IBM Journal of Research and Development*, vol. 12, p. 113, 1968. 2, 35, 39
- [5] Petersen, "Micromechanical light modulator array fabricated on silicon," *Applied Physics Letters*, 1977. 2, 44
- [6] K. Petersen, "Silicon as a mechanical material," *Proceedings of the IEEE*, vol. 70, pp. 420 – 457, may 1982. 3
- [7] R. T. Howe and R. S. Muller, "Polycrystalline silicon micromechanical beams," *Journal of The Electrochemical Society*, vol. 130, no. 6, pp. 1420–1423, 1983. 3
- [8] H. Helvajian, ed., *Microengineering Aerospace Systems*. American Institute of Aeronautics and Astronautics/Aerospace Press, 1999. 3
- [9] L.-S. Fan, Y.-C. Tai, and R. Muller, "Integrated movable micromechanical structures for sensors and actuators," *Electron Devices, IEEE Transactions on*, vol. 35, pp. 724 –730, jun 1988. 3
- [10] W. C. Tang, T.-C. H. Nguyen, M. W. Judy, and R. T. Howe, "Electrostatic-comb drive of lateral polysilicon resonators," *Sensors and Actuators A: Physical*, vol. 21, no. 1-3, pp. 328 – 331, 1990. Proceedings of the 5th International Conference on Solid-State Sensors and Actuators and Eurosensors III. 3
- [11] F. Houston, "Toward the creation of the worlds smallest radio," *NRL Review acoustics 2005*, 2005. 3

- [12] N. Tien, A. Ongkodjojo, R. Roberts, and D. Li, "The future of MEMS in energy technologies," *Solid-State and Integrated-Circuit Technology, 2008. ICSICT 2008. 9th International Conference on*, pp. 2452–2455, oct. 2008. 3
- [13] K. C. Schwab and M. L. Roukes, "Putting mechanics into quantum mechanics," *Physics Today*, p. 36, 2005. 3
- [14] J. Bryzek, S. Roundy, B. Bircumshaw, C. Chung, K. Castellino, J. Stetter, and M. Vestel, "Marvelous MEMS," *Circuits and Devices Magazine, IEEE*, vol. 22, pp. 8–28, march-april 2006. 4
- [15] B. Tilmans, De Raedt, "MEMS for wireless communications: from RF-MEMS components to RF-MEMS-SiP," *Journal of Micromechanics and Microengineering*, vol. 13, p. S139S163, 2003. 4
- [16] J.-C. Eloy and M. E., "Update of MEMS markets." www.semiconductor.net, March 2008. 5
- [17] C. Lam, "A review of the recent development of MEMS and crystal oscillators and their impacts on the frequency control products industry," in *Ultrasonics Symposium, 2008. IUS 2008. IEEE*, pp. 694–704, 2-5 2008. 5
- [18] R. Linker, "Silicon MEMS oscillators," 2009. 5
- [19] A. Partridge and J. McDonald, "MEMS resonators look to displace quartz oscillators," *MEMS Manufacturing*, pp. 11–14, 2006. 5, 6
- [20] S. Mushell and S. Ohr, "MEMS resonators vs. crystal oscillators for IC timing circuits." *Small Times*, 2009. 6
- [21] G. Brezeanu, "Silicon carbide (SiC): a short history. An analytical approach for SiC power device design," in *Semiconductor Conference, 2005. CAS 2005 Proceedings. 2005 International*, vol. 2, pp. 345–348 vol. 2, 5-5 2005. 6
- [22] G. L. Harris and C. V.-W. Yang, eds., *Amorphous and crystalline silicon carbide I*, vol. 34 of *Springer Proceedings in Physics*, Springer-Verlag, 1989. 7
- [23] G. L. Harris and C. V.-W. Yang, eds., *Amorphous and crystalline silicon carbide II*, vol. 43 of *Springer Proceedings in Physics*, Springer-Verlag, 1989. 7
- [24] L. Tong, M. Mehregany, and L. G. Matus, "Mechanical properties of 3C silicon carbide," *Applied Physics Letters*, vol. 60, no. 24, pp. 2992–2994, 1992. 7
- [25] C. A. Zorman, A. J. Fleischman, A. S. Dewa, M. Mehregany, C. Jacob, S. Nishino, and P. Pirouz, "Epitaxial growth of 3C-SiC films on 4 in. diameter (100) silicon wafers by atmospheric pressure chemical vapor deposition," *Journal of Applied Physics*, vol. 78, no. 8, pp. 5136–5138, 1995. 7, 15

- [26] G. Krotz, W. Legner, C. Wapner, H. Moller, H. Sonntag, and G. Muller, "Silicon carbide as a mechanical material," *Solid-State Sensors and Actuators, 1995 and Eurosensors IX.. Transducers '95. The 8th International Conference on*, vol. 2, pp. 186 –189, jun 1995. 7
- [27] M. Mehregany, C. Zorman, N. Rajan, and C. H. Wu, "Silicon carbide MEMS for harsh environments," *Proceedings of the IEEE*, vol. 86, pp. 1594 –1609, aug 1998. 7, 14, 15, 23, 24
- [28] P. M. Sarro, "Silicon carbide as a new MEMS technology," *Sensors and Actuators A: Physical*, vol. 82, no. 1-3, pp. 210 – 218, 2000. 7, 15, 17, 20
- [29] R. Cheung, ed., *Silicon carbide microelectromechanical systems for harsh environments*. Imperial College Press, 2006. 7, 14, 15, 16, 25
- [30] F. Bechstedt, P. Kckell, A. Zywiets, K. Karch, B. Adolph, K. Tenelsen, and J. Furthmller, "Polytypism and properties of silicon carbide," *phys. stat. sol. (b)*, vol. 202, p. 35, 1997. 12
- [31] M. Willander, M. Friesel, Q. Wahab, and B. Straumal, "Silicon carbide and diamond for high temperature device applications," *Journal of Materials Science: Materials in Electronics*, vol. 17, p. 1, 2006. 12, 14
- [32] V. Cimalla, J. Pezoldt, and O. Ambacher, "Group III nitride and SiC based MEMS and NEMS: materials properties, technology and applications," *Journal of Physics D: Applied Physics*, vol. 40, no. 20, pp. 6386–6434, 2007. 14, 16, 17, 40, 43
- [33] O. Kordina, L. O. Bjrkettun, A. Henry, C. Hallin, R. C. Glass, L. Hultman, J. E. Sundgren, and E. Janzn, "Growth of 3C–SiC on on-axis Si(100) substrates by chemical vapor deposition," *Journal of Crystal Growth*, vol. 154, no. 3-4, pp. 303 – 314, 1995. 15
- [34] X.-A. Fu, J. L. Dunning, C. A. Zorman, and M. Mehregany, "Polycrystalline 3C-SiC thin films deposited by dual precursor LPCVD for MEMS applications," *Sensors and Actuators A: Physical*, vol. 119, no. 1, pp. 169 – 176, 2005. 15
- [35] M. Mehregany and C. A. Zorman, "SiC MEMS: opportunities and challenges for applications in harsh environments," *Thin Solid Films*, vol. 355-356, pp. 518 – 524, 1999. 15
- [36] A. Henry, E. Janzén, E. Mastropaolo, and R. Cheung, "Single crystal and polycrystalline 3C-SiC for MEMS applications," *Materials Science Forum*, vol. 615-617, pp. 625–628, 2009. 15, 68
- [37] F. Liu, C. Carraro, A. P. Pisano, and R. Maboudian, "Growth and characterization of nitrogen-doped polycrystalline 3C-SiC thin films for harsh environment MEMS applications," *Journal of Micromechanics and Microengineering*, vol. 20, no. 3, p. 035011, 2010. 15

-
- [38] J. Hong, R. J. Shul, L. Zhang, L. F. Lester, H. Cho, Y. B. H. and. C. Hays, K. B. Jung, S. J. Pearton, C. M. Zetterling, and M. Östling, "Plasma chemistries for high density plasma etching of SiC," *Journal of Electronic Materials*, vol. 28, p. 196, 1999. 16, 17
- [39] F. A. Khan, B. Roof, L. Zhou, and I. Adesida, "Etching of silicon carbide for device fabrication and through via-hole formation," *Journal of Electronic Materials*, vol. 30, pp. 212–219, 2001. 16
- [40] P. H. Yih, V. Saxena, and A. J. Steckl, "A review of SiC reactive ion etching in fluorinated plasmas," *physica status solidi (b)*, vol. 202, pp. 605–642, 1997. 16
- [41] B. Li, L. Cao, and J. H. Zhao, "Evaluation of damage induced by inductively coupled plasma etching of 6H-SiC using Au Schottky barrier diodes," *Applied Physics Letters*, vol. 73, no. 5, pp. 653–655, 1998. 16
- [42] Beheim, "Deep RIE process for silicon carbide power electronics and MEMS," *Materials Research Society Symposium Proceedings*, vol. 622, 2000. 16
- [43] N. O. V. Plank, M. A. Blauw, E. W. J. M. van der Drift, and R. Cheung, "The etching of silicon carbide in inductively coupled SF_6/O_2 plasma," *Journal of Physics D: Applied Physics*, vol. 36, no. 5, p. 482, 2003. 17, 21
- [44] J. W. Palmour, R. F. Davis, T. M. Wallett, and K. B. Bhasin, "Dry etching of β -SiC in CF_4 and $CF_4 + O_2$ mixtures," *Journal of Vacuum Science & Technology A: Vacuum, Surfaces, and Films*, vol. 4, no. 3, pp. 590–593, 1986. 17
- [45] L. Jiang, R. Cheung, R. Brown, and A. Mount, "Inductively coupled plasma etching of SiC in SF_6/O_2 and etch-induced surface chemical bonding modifications," *Journal of Applied Physics*, vol. 93, no. 3, pp. 1376–1383, 2003. 17, 54
- [46] T. Zhu, P. Argyrakis, E. Mastropaolo, K. K. Lee, and R. Cheung, "Dry etch release processes for micromachining applications," *Journal of Vacuum Science & Technology B*, vol. 25, no. 6, pp. 2553–2557, 2007. 19, 20, 55
- [47] A. Fleischman, S. Roy, C. Zorman, M. Mehregany, and L. Matus, "Polycrystalline silicon carbide for surface micromachining," *Micro Electro Mechanical Systems, 1996, MEMS '96, Proceedings. 'An Investigation of Micro Structures, Sensors, Actuators, Machines and Systems'. IEEE, The Ninth Annual International Workshop on*, pp. 234 –238, feb 1996. 19, 24
- [48] D. J. Young, I. E. Pehlivanoglu, and C. A. Zorman, "Silicon carbide MEMS-resonator-based oscillator," *Journal of Micromechanics and Microengineering*, vol. 19, no. 11, p. 115027 (10pp), 2009. 19, 25
- [49] Y.-I. Lee, K.-H. Park, J. Lee, C.-S. Lee, H. Yoo, C.-J. Kim, and Y.-S. Yoon, "Dry release for surface micromachining with HF vapor-phase etching," *Microelectromechanical Systems, Journal of*, vol. 6, pp. 226 –233, sep 1997. 20

- [50] A. Witvrouw, B. D. Bois, P. D. Moor, A. Verbist, C. A. V. Hoof, H. Bender, and C. Baert, "Comparison between wet HF etching and vapor HF etching for sacrificial oxide removal," *Micromachining and Microfabrication Process Technology VI*, vol. 4174, no. 1, pp. 130–141, 2000. 20
- [51] L. Jiang, R. Cheung, M. Hassan, A. J. Harris, J. S. Burdess, C. A. Zorman, and M. Mehregany, "Fabrication of SiC microelectromechanical systems using one-step dry etching," *Journal of Vacuum Science & Technology B: Microelectronics and Nanometer Structures*, vol. 21, no. 6, pp. 2998–3001, 2003. 21, 54, 106, 126
- [52] L. Jiang, M. Hassan, R. Cheung, A. Harris, J. Burdess, C. Zorman, and M. Mehregany, "Dry release fabrication and testing of SiC electrostatic cantilever actuators," *Microelectronic Engineering*, vol. 78–79, pp. 106 – 111, 2005. Proceedings of the 30th International Conference on Micro- and Nano-Engineering. 21, 25
- [53] L. Jiang, R. Cheung, J. Hedley, M. Hassan, A. Harris, J. Burdess, M. Mehregany, and C. Zorman, "SiC cantilever resonators with electrothermal actuation," *Sensors and Actuators A: Physical*, vol. 128, no. 2, pp. 376 – 386, 2006. 21, 25, 36, 38, 39, 127, 140, 142
- [54] R. Cheung and P. Argyrakis, "Micro-scale sensors based in silicon carbide and silicon," *Proceedings of the Institution of Mechanical Engineers, Part C, Journal of Mechanical Engineering Science, Special Issue on Microsystems Technology*, vol. 222, pp. 19–26, 2008. 21
- [55] T. Nagai and M. Itoh, "SiC thin-film thermistors," *Industry Applications, IEEE Transactions on*, vol. 26, pp. 1139 –1143, nov/dec 1990. 22
- [56] K. Kamimura, T. Miwa, T. Sugiyama, T. Ogawa, N. Nakao, and Y. Onuma, "Preparation of polycrystalline SiC thin-film and its application to resistive sensors," *Silicon Carbide and Related Materials*, vol. 142, pp. 825–828, 1996. 22
- [57] R. S. Okojie, A. A. Ned, and A. D. Kurtz, "Operation of $\alpha(6H)$ -SiC pressure sensor at 500 °C," *Sensors and Actuators A: Physical*, vol. 66, no. 1–3, pp. 200 – 204, 1998. 22
- [58] R. Ziermann, J. von Berg, W. Reichert, E. Obermeier, M. Eickhoff, and G. Krotz, "A high temperature pressure sensor with β -SiC piezoresistors on SOI substrates," *Solid State Sensors and Actuators, 1997. TRANSDUCERS '97 Chicago., 1997 International Conference on*, vol. 2, pp. 1411 –1414 vol.2, jun 1997. 23
- [59] A. R. Atwell, R. S. Okojie, K. T. Kornegay, S. L. Roberson, and A. Beliveau, "Simulation, fabrication and testing of bulk micromachined 6H-SiC high-g piezoresistive accelerometers," *Sensors and Actuators A: Physical*, vol. 104, no. 1, pp. 11 – 18, 2003. 23
- [60] L. Pakula, H. Yang, and P. French, "A CMOS compatible SiC accelerometer," *Sensors, 2003. Proceedings of IEEE*, vol. 2, pp. 761 – 764 Vol.2, oct. 2003. 24

- [61] L. Pakula, H. Yang, and P. French, "3-D silicon carbide surface micromachined accelerometer compatible with CMOS processing," *Advanced Semiconductor Devices and Microsystems, 2008. ASDAM 2008. International Conference on*, pp. 227 – 230, 2008. 24
- [62] S. Roy, R. DeAnna, C. Zorman, and M. Mehregany, "Fabrication and characterization of polycrystalline sic resonators," *Electron Devices, IEEE Transactions on*, vol. 49, pp. 2323 – 2332, dec 2002. 24
- [63] W.-T. Chang and C. Zorman, "Electrical characterization of microelectromechanical silicon carbide resonators," *Sensors*, vol. 8, no. 9, pp. 5759–5774, 2008. 24
- [64] C.-C. Nguyen, "Vibrating RF MEMS for next generation wireless applications," *Custom Integrated Circuits Conference, 2004. Proceedings of the IEEE 2004*, pp. 257 – 264, 3-6 2004. 25
- [65] J. Melzak, "Silicon carbide for RF MEMS," in *Microwave Symposium Digest, 2003 IEEE MTT-S International*, vol. 3, pp. 1629–1632 vol.3, June 2003. 25
- [66] M. Placidi, P. Godignon, N. Mestres, G. Abadal, G. Ferro, A. Leycuras, and T. Chassagne, "Fabrication of monocrystalline 3C-SiC resonators for MHz frequency sensors applications," *Sensors and Actuators B: Chemical*, vol. 133, no. 1, pp. 276 – 280, 2008. 25
- [67] X. M. H. Huang, X. L. Feng, C. A. Zorman, M. Mehregany, and M. L. Roukes, "VHF, UHF and microwave frequency nanomechanical resonators," *New Journal of Physics*, vol. 7, no. 1, p. 247, 2005. 25
- [68] R. A. Johnson, ed., *Mechanical Filters in Electronics*. Wiley, 1983. 29, 30, 31, 32
- [69] H. A. Tilmans, M. Elwenspoek, and J. H. Fluitman, "Micro resonant force gauges," *Sensors and Actuators A: Physical*, vol. 30, no. 1-2, pp. 35 – 53, 1992. 34
- [70] C. Leondes, ed., *MEMS/NEMS Handbook - Sensors & Actuators*, vol. 4. Springer, 2006. 34
- [71] Timoshenko, "Analysis of bi-metal thermostats," *Journal of the Optical Society of America*, vol. 11, p. 233, 1925. 35, 36
- [72] M. Othman and A. Brunnschweiler, "Electrothermally excited silicon beam mechanical resonators," *Electronics Letters*, vol. 23, pp. 728 –730, july 1987. 35
- [73] O. Brand, H. Baltes, and U. Baldenweg, "Thermally excited silicon oxide beam and bridge resonators in CMOS technology," *Electron Devices, IEEE Transactions on*, vol. 40, pp. 1745 –1753, oct 1993. 35
- [74] Y. Zhang, Y. Zhang, and R. Marcus, "Thermally actuated microprobes for a new wafer probe card," *Microelectromechanical Systems, Journal of*, vol. 8, no. 1, pp. 43 –49, 1999. 36, 37

-
- [75] M. Zalalutdinov, K. L. Aubin, R. B. Reichenbach, A. T. Zehnder, B. Houston, J. M. Parpia, and H. G. Craighead, "Shell-type micromechanical actuator and resonator," *Applied Physics Letters*, vol. 83, no. 18, pp. 3815–3817, 2003. 36
- [76] R. Reichenbach, M. K. Zalalutdinov, K. L. Aubin, D. A. Czaplewski, B. Ilic, H. Houston, H. G. Craighead, and P. J. M., "Resistively actuated micromechanical dome resonators," *Proceedings of SPIE*, vol. 5344, pp. 51–58, 2004. 36
- [77] R. Reichenbach, M. Zalalutdinov, K. Aubin, R. Rand, B. Houston, J. Parpia, and H. Craighead, "Third-order intermodulation in a micromechanical thermal mixer," *Microelectromechanical Systems, Journal of*, vol. 14, pp. 1244 – 1252, dec. 2005. 36
- [78] W. C. Young and R. G. Budynas, *Roark's Formulas for Stress and Strain*. McGraw-Hill, 6th ed., 1989. 36, 37, 86
- [79] M. Elwenspoek, F. Blom, S. Bouwstra, T. Lammerink, F. van de Pol, H. Tilmans, T. Popma, and J. Fluitman, "Transduction mechanisms and their applications in micromechanical devices," in *Micro Electro Mechanical Systems, 1989, Proceedings, An Investigation of Micro Structures, Sensors, Actuators, Machines and Robots. IEEE*, pp. 126 –132, 20-22 1989. 39
- [80] D. DeVoe, "Piezoelectric thin film micromechanical beam resonators," *Sensors and Actuators A: Physical*, vol. 88, no. 3, pp. 263 – 272, 2001. 40, 42, 43
- [81] G. Piazza, R. Abdolvand, G. K. Ho, and F. Ayazi, "Voltage-tunable piezoelectrically-transduced single-crystal silicon micromechanical resonators," *Sensors and Actuators A: Physical*, vol. 111, no. 1, pp. 71 – 78, 2004. 40
- [82] B. Cunningham, Jenkins, "Experimental investigation of optimum thickness of a piezoelectric element for cantilever actuation," *IEE Proceedings Science, Measurement and Technology*, vol. 44, 1997. 40
- [83] E. Hong, S. Trolier-McKinstry, R. Smith, S. Krishnaswamy, and C. Freidhoff, "Design of MEMS PZT circular diaphragm actuators to generate large deflections," *Microelectromechanical Systems, Journal of*, vol. 15, pp. 832–839, Aug. 2006. 40
- [84] C. Zuo, N. Sinha, J. Van der Spiegel, and G. Piazza, "Multi-frequency pierce oscillators based on piezoelectric AlN contour-mode MEMS resonators," *Frequency Control Symposium, 2008 IEEE International*, pp. 402–407, May 2008. 41
- [85] G. Piazza, P. Stephanou, and A. Pisano, "Piezoelectric aluminum nitride vibrating contour-mode MEMS resonators," *Microelectromechanical Systems, Journal of*, vol. 15, pp. 1406–1418, Dec. 2006. 41, 48
- [86] G. Piazza, P. Stephanou, J. Porter, M. Wijesundara, and A. Pisano, "Low motional resistance ring-shaped contour-mode aluminum nitride piezoelectric micromechanical resonators for UHF applications," in *Micro Electro Mechanical Systems, 2005. MEMS 2005. 18th IEEE International Conference on*, pp. 20 – 23, 30 2005. 41

-
- [87] L. Yan, M. Wu, and W. Tang, "A 1.14 GHz piezoelectrically transduced disk resonator," in *Micro Electro Mechanical Systems, 2005. MEMS 2005. 18th IEEE International Conference on*, pp. 203 – 206, 30 2005. 41
- [88] Doppalapudi, "Sensors based on SiC-AlN MEMS," *Proceedings - Electrochemical Society*, 2004. 41
- [89] D. DeVoe and A. Pisano, "Modeling and optimal design of piezoelectric cantilever microactuators," *Microelectromechanical Systems, Journal of*, vol. 6, pp. 266–270, Sep 1997. 41
- [90] W. C. Tang, T.-C. H. Nguyen, and R. T. Howe, "Laterally driven polysilicon resonant microstructures," *Sensors and Actuators*, vol. 20, no. 1-2, pp. 25 – 32, 1989. A Special Issue Devoted to Micromechanics. 44
- [91] F. Bannon, J. Clark, and C.-C. Nguyen, "High-Q HF microelectromechanical filters," *Solid-State Circuits, IEEE Journal of*, vol. 35, pp. 512 –526, apr 2000. 44
- [92] A. Wong and C. T.-C. Nguyen, "Micromechanical mixer-filters ("Mixlers")," *Journal Of Microelectromechanical Systems*, vol. 13, pp. 100–112, 2004. 44, 46
- [93] J. Wang, J. Butler, T. Feygelson, and C.-C. Nguyen, "1.51-GHz nanocrystalline diamond micromechanical disk resonator with material-mismatched isolating support," *Micro Electro Mechanical Systems, 2004. 17th IEEE International Conference on. (MEMS)*, pp. 641 – 644, 2004. 44
- [94] Fedder, "CMOS-MEMS resonant mixer-filters," *Electron Devices Meeting, 2005. IEDM Technical Digest. IEEE International*, vol. na, pp. 274– 277, 2005. 47
- [95] J. Wang, Z. Ren, and C.-C. Nguyen, "1.156-GHz self-aligned vibrating micromechanical disk resonator," *Ultrasonics, Ferroelectrics and Frequency Control, IEEE Transactions on*, vol. 51, pp. 1607 – 1628, dec. 2004. 47
- [96] J. Clark, W.-T. Hsu, M. Abdelmoneum, and C.-C. Nguyen, "High-Q UHF micromechanical radial-contour mode disk resonators," *Microelectromechanical Systems, Journal of*, vol. 14, pp. 1298 – 1310, dec. 2005. 47
- [97] D. Yan, A. Khajepour, and R. Mansour, "Design and modeling of a mems bidirectional vertical thermal actuator," *Journal of Micromechanics and Microengineering*, vol. 14, no. 7, p. 841, 2004. 48
- [98] P. Yang, M. Stevenson, Y. Lai, C. Mechefske, M. Kujath, and T. Hubbard, "Design, modeling and testing of a unidirectional MEMS ring thermal actuator," *Sensors and Actuators A: Physical*, vol. 143, no. 2, pp. 352 – 359, 2008. 48
- [99] R. Hickey, D. Sameoto, T. Hubbard, and M. Kujath, "Time and frequency response of two-arm micromachined thermal actuators," *Journal of Micromechanics and Microengineering*, vol. 13, no. 1, p. 40, 2003. 48

-
- [100] R. Abdolvand, H. Mirilavasani, and F. Ayazi, "Single-resonator dual-frequency thin-film piezoelectric-on-substrate oscillator," *Electron Devices Meeting, 2007. IEDM 2007. IEEE International*, pp. 419–422, 10-12 2007. 48
- [101] J.-S. Park, S.-H. Kim, H.-D. Park, J. Ha, and S.-G. Kang, "Characterization of Sol-Gel multicoated thick $\text{Pb}(\text{Zr}_{0.52}, \text{Ti}_{0.48})\text{O}_3$ films on platinized silicon substrates for microdevices applications," *Japanese Journal of Applied Physics*, vol. 42, no. 12, pp. 7497–7501, 2003. 59, 154
- [102] K. Zheng, J. Lu, and J. Chu, "A novel wet etching process of $\text{Pb}(\text{Zr}, \text{Ti})\text{O}_3$ thin films for applications in microelectromechanical system," *Japanese Journal of Applied Physics*, vol. 43, no. 6B, pp. 3934–3937, 2004. 59
- [103] C. N. Banwell, *Fundamental of Molecular Spectroscopy*. Mc.Graw-Hill, fourth ed., 1994. 69
- [104] P. Y. Yu and M. Cardona, *Fundamentals of Semiconductors: Physics and Materials Properties*. Springer, 1996. 71
- [105] Z. C. Feng, C. C. Tin, R. Hu, and J. Williams, "Raman and rutherford backscattering analyses of cubic SiC thin films grown on Si by vertical chemical vapor deposition," *Thin Solid Films*, vol. 266, no. 1, pp. 1–7, 1995. 71, 72
- [106] S. Nakashima and H. Harima, "Raman investigation of SiC polytypes," *Physica Status Solidi a*, vol. 162, p. 39, 1997. 72
- [107] Z. C. Feng, "Optical properties of cubic SiC grown on Si substrate by chemical vapor deposition," *Microelectronic Engineering*, vol. 83, no. 1, pp. 165–169, 2006. The Symposium K Proceedings of the 3rd International Conference on Materials for Advanced Technologies (ICMAT 2005). 72
- [108] C. M. Su, M. Wuttig, A. Fekade, and M. Spencer, "Elastic and anelastic properties of chemical vapor deposited epitaxial 3C-SiC," *Journal of Applied Physics*, vol. 77, no. 11, pp. 5611–5615, 1995. 79
- [109] Y.-H. Min and Y.-K. Kim, "In situ measurement of residual stress in micromachined thin films using a specimen with composite-layered cantilevers," *Journal of Micromechanics and Microengineering*, vol. 10, no. 3, pp. 314–321, 2000. 79
- [110] W. Fang, "Comments on measuring thin-film stresses using bi-layer micromachined beams," *J. Micromech. Microeng.*, vol. 5, 1995. 79
- [111] J. Wylde and T. Hubbard, "Elastic properties and vibration of micro-machined structures subject to residual stresses," *IEEE Proceedings Canadian Conference Electrical and Computer Engineering*, vol. 3, pp. 1674–1679 vol.3, 1999. 79
- [112] Y. T. Yang, K. L. Ekinici, X. M. H. Huang, L. M. Schiavone, M. L. Roukes, C. A. Zorman, and M. Mehregany, "Monocrystalline silicon carbide nanoelectromechanical systems," *Applied Physics Letters*, vol. 78, no. 2, pp. 162–164, 2001. 126

- [113] M. Pozzi, M. Hassan, A. J. Harris, J. S. Burdess, L. Jiang, K. K. Lee, R. Cheung, G. J. Phelps, N. G. Wright, C. A. Zorman, and M. Mehregany, "Mechanical properties of a 3C-SiC film between room temperature and 600 °C," *Journal of Physics D: Applied Physics*, vol. 40, no. 11, pp. 3335–3342, 2007. 127, 138, 143
- [114] K. Tanaka, R. Kihara, A. Snchez-Amores, J. Montserrat, and J. Esteve, "Parasitic effect on silicon MEMS resonator model parameters," *Microelectronic Engineering*, vol. 84, no. 5-8, pp. 1363 – 1368, 2007. Proceedings of the 32nd International Conference on Micro- and Nano-Engineering. 149